Rochester Institute of Technology

RIT Digital Institutional Repository

12-12-1996

Aluminum nitride films by reactive sputtering

Alvin Randolph

Aluminum Nitride Thin Films by Reactive Sputtering

by

Alvin G. Randolph, III

Aluminum Nitride Thin Films by Reactive Sputtering

by

Alvin G. Randolph, III

December 12, 1996

Alvin G. Randolph, III   December 12, 1996

Aluminum Nitride Films by Reactive Sputtering

by

Alvin G. Randolph, III

A thesis submitted in partial fulfillment of the requirements for the degree of

Master of Science

in Materials Science and Engineering at the Rochester Institute of Technology.

Approved by

Dr. Santosh K. Kurinec, Advisor
Department of Microelectronics Engineering & Materials Science and Engineering

Dr. Marietta Scanlon
Department of Mechanical Engineering & Materials Science and Engineering

---

Dr. Tracy Davis
Department of Physics & Materials Science and Engineering

Dr. Vern Lindberg
Department of Physics & Materials Science and Engineering

Abstract

Aluminum nitride thin films (~1000 Å) have been deposited on silicon substrate by reactive sputtering using Al target in 1:1 $Ar:N_2$ environment. The atomic force microscopy examination revealed continuous microcrystalline film structure. The Auger electron spectroscopic analysis shows the presence of oxygen in the films. The annealing at 850° C in nitrogen is found to cause recrystallinization and, by FTIR analysis, further oxidation of the films. The films can be characterized as lossy dielectrics with relative permittivity ~ 10, higher than the bulk value of 8.9. Annealing the films is found to reduce anion vacancies and improve the dielectric strength within a range of a few MV/cm in these thin films.

Optical constants, n & κ, have been obtained from reflectance and transmittance spectra (190-900 nm) of films on fused silica. The results indicate the presence of a low energy absorption tail, and exponential absorption that is proportional to degree of disorder in the film. The average defect density of the film as deposited was 1.1×10^{20} cm^{-3}. Annealing the film at 760° C increased the degree of disorder resulting in an average defect density of 3.4×10^{20} cm^{-3}. Subsequent annealing at 800° C and 850° C systematically decreased the degree of disorder and the average defect density. The real part of permittivity (ε_1) of the annealed films over this frequency range varies approximately ±0.5 from the ε_∞ of 4.84.

Table of Contents

List of Figures

List of Tables

Acknowledgments

I wish to acknowledge my debt to my Committee, Dr. Kurinec, Dr. Scanlon, Dr. Lindberg, and Dr. Davis for their support and guidance. Special recognition goes to Dr. Kurinec for her unswerving zeal to publish whereby I acquired a keen appreciation for the art of scientific reason. I am also grateful to Dr. Bruce Smith for the use of his spectrometer and optics software, the Chemistry department for FTIR spectrometer, and the Mechanical Engineering department for the AFM and x-ray diffractometer.

This publication is dedicated to the memory of Roderick Dwain Randolph (1955 - 1995).

1 Introduction

1.1 Properties of Aluminum Nitride

Aluminum nitride is a member of a group of diatomic compounds called the III-V nitrides. Other members of this group consists of indium nitride, gallium nitride, and boron nitride. Aluminum nitride, indium nitride, and gallium nitride, are wide direct band-gap semiconductors. Boron nitride is an insulator usually and, while a III-V nitride, it is usually not included in topics with the first three. Boron nitride exists in two crystallographic forms, and is very hard and wear resistant as is aluminum nitride.

The appeal of aluminum nitride stems from the following:

- Its high thermal conductivity, theoretically 320 $Wm^{-1}K^{-1}$, which surpasses that of alumina by almost a factor of 10.[1,2,3,4,5]

- very high electrical resistivity,

- a high dielectric constant,

- low dielectric loss,[1,6]

- a thermal expansion coefficient closer to that of silicon than alumina.

The numerical values of these physical and electrical properties of aluminum nitride are given in Table 1-1.

Pure AlN crystallizes in a wurtzite structure which is similar to the zinc blende structure. Both structures, shown in Figure 1-1, consist of a cation surrounded by anions and anions surrounded by cations in a tetrahedral arrangement.[7] Also, the unit cell in both structures is hexagonal. The basis of the AlN unit cell, shown in Figure 1-2, consists of two Al atoms at (0,0,0) & (1/3,2/3,1/2) and two N atoms at (0,0,0.385) & (1/3,2/3,0.885) in a right-handed Cartesian coordinate system.[8] The lattice constants are a = 3.111 and c = 4.978 Å which are the magnitudes of the basis vectors, **a**, and **c** of the hexagon unit cell.[8,9]

1.1.1 Applications of Aluminum Nitride

Its high melting temperature (> 2800° C), chemical resistivity and transparency in the visible spectrum makes an ideal passivation layer for microelectronic devices and a protective coating for electro-optical devices.[10]

The development of high bit rate optical communication systems requires the use of very fast light modulators. In order to match the characteristics of light in optical fibers,

the modulator must be precisely integrated with the fibers. AlN is a promising thin-film piezoelectric material possessing high ultrasonic velocity and fairly large electro-mechanical coupling.[11]

Property	AlN	Al_2O_3	Comments
Density	3.25 gm/cm^3	3.75 gm/cm^3	Bulk state
Thermal conductivity	100-230 W/m-°K	20 W/m-°K	
Thermal expansion Coef	a:4.15 μm-m^{-1}-°K^{-1} c:5.27	a:8.11 μm-m^{-1}-°K^{-1} c:7.28	for Si, 2.5 μm-m^{-1}-°K^{-1}
Melting Point, T_m	3273 °K		
Index of refraction @ 632.8 nm	2.08	1.66	
Band Gap, E_g	~6.2 eV	~6.7 eV	E_g (AlN) is direct
IR absorption	680.0 cm^{-1}	460.0 cm^{-1}	
Dispersion edge, $λ_d$	0.24 μm	0.2 μm	no dispersion $λ > λ_d$
Hi freq. dielectric, $ε_∞$	4.84	2.77	
Dielectric const, 1 MHz	8.9	9.4	
Dielectric loss, 1 MHz	0.0003	0.0004	
Dielectric strength	15 kV/mm	15 kV/mm	
Resistivity	$> 10^{14}$	$> 10^{14}$	

Table 1-1 Some Physical Properties of AlN
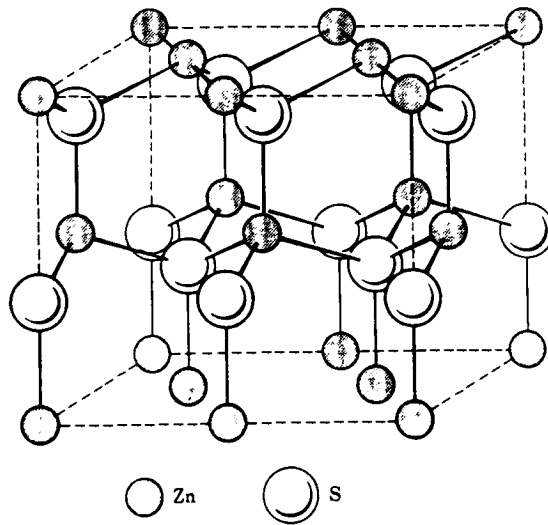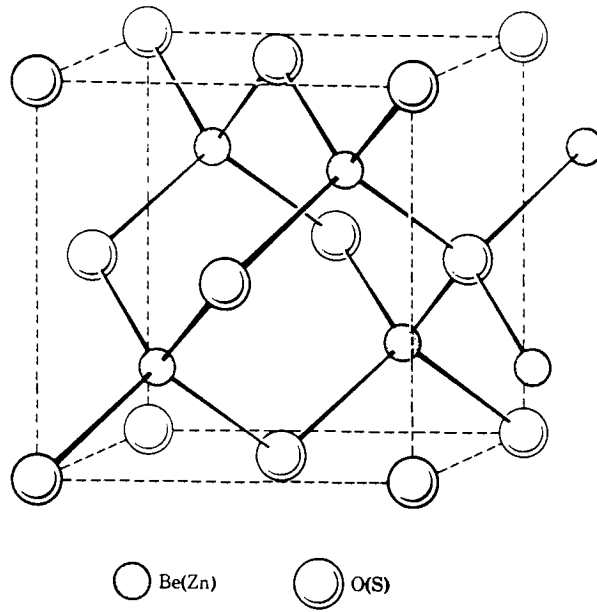
Figure 1-1   Zinc blende (top) and wurtzite (bottom) crystals.[7]

Most of the deposition techniques of AlN require substrate temperatures in the range of 1000°C to 1200°C for single crystal growth. But some devices, such as magneto-optical discs, cannot tolerate temperatures >500°C. So, AlN passivation layers cannot be applied to these devices in high temperature environments. As a result, considerable effort has been placed on lowering the deposition temperature and still get high resistivity and high purity AlN films.[11]
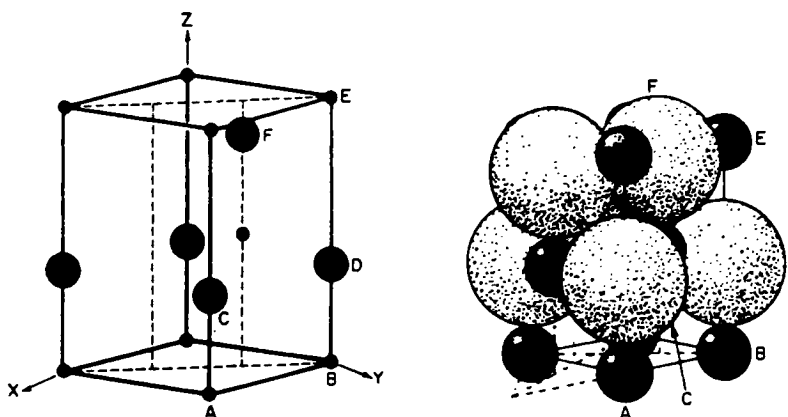
Figure 1-2 The AlN unit cell..[8]

1.2 Synthesis of Aluminum Nitride

Aluminum nitride can be synthesized in two forms; as a bulk ceramic powder and as a thin film. The bulk material is synthesized by the reduction-nitridation of alumina or direct nitridation of aluminum and then undergoes mechanical processing to achieve a certain grain size distribution. This form of aluminum nitride can be purchased from a refractory supplier and processed the same as any ceramic powder by isostatic pressing, tape casting, injection molding, etc. The thin films are usually synthesized during deposition via a CVD or PVD process.

1.2.1 Bulk Aluminum Nitride

Aluminum nitride powders are manufactured by the reduction-nitridation of alumina with carbon or by the direct nitridation of metallic aluminum. The nitridation of alumina involves the mixing of graphite with γ-alumina and heating the mixture to 1700° C in a

modest vacuum with N_2 gas flowing. After about 2 hr. the alumina will have been reduced to aluminum nitride.[12]

Aluminum metal can be nitrided directly with ammonia. Pure aluminum metal is brought in contact with ammonia at a very low temperature (~ 100° K) in a closed reaction chamber. The temperature is increased to at least room temperature where the reaction proceeds to completion.[13,14]

While high purity guarantees the highest possible thermal conductivity and translucency of an AlN substrate, additives are used to increase sinterability of the powder. Some sintering aids are calcium carbonate ($CaCO_3$), calcium nitrate ($Ca(NO_3)_2$) yttrium oxide (Y_2O_3), and calcium aluminate ($3CaO \cdot Al_2O_3$) which is sometimes designated by C_3A. Although most of the sintering additive evaporates during the sintering process, less than .01% Ca metal and 0.16% oxygen from C_3A is left behind. The thermal conductivity is reduced to ~175 $W\text{-}m^{-1}\text{-}K^{-1}$ [6]

1.2.2 Aluminum Nitride Films

Reactive sputtering of AlN films will results if N_2 gas occupies a significant partial pressure of the sputtering gas mixture. The Ar/N_2 ratio affects the deposition rate and the nitrogen composition of the film inversely, so care must be exercised in choosing a working ratio. To enhance the reactivity between aluminum and nitrogen, aluminum atoms can be sputtered under bombardment of N_2^+ ions from an ion gun as well as the Ar^+ ions from the plasma. This is called ion assisted deposition (IAD) and the nitrogen composition of the film can be increased or decreased by an appropriate choice of N_2^+ energy.[15]

In the CVD process, aluminum nitride thin films are deposited as a product of the reaction between a metal organic derivative of aluminum such as trichloroaluminum or trimethylaluminum (TMAl) and ammonia (NH_3). This type of reaction is carried out in an air-tight chamber that has been evacuated into the mT range. The reactants are admitted into the chamber until the pressure increases to the order of 1 atmosphere, N_2 being the carrier gas for TMAl. The temperature in the chamber can range from 300° to 1000+ °C. The higher temperatures are used to achieve epitaxial growth of the film as it is deposited. This version of the chemical vapor deposition process is called metal organic chemical va-

por deposition (MOCVD).[6] Hot filaments and lasers have also been employed to control reactivity and film characteristics.

2 Deposition of Aluminum Nitride Film by Sputtering

2.1 Fundamentals of Sputtering

Sputtering is a vacuum process where ions in a plasma bombard a target under the influence of an electric field. The electric field may be generated by a d.c. potential (typically 500 to 5000 V), or a high frequency a.c. voltage source. The plasma is an electrically neutral glow discharge of electrons and positive ions. Noble gases work best as a bombarding species because they are least likely to form reactants on the target surface. Argon is usually the gas of choice because these atoms are comparable in size to most target atoms and this results in optimum sputter yield. Krypton and Xenon have also been used, but they are more costly than Argon. When the argon ions collide with the target, target atoms are ejected by momentum exchange with energies in the range of 10 - 40 eV. These collisions also produce a small number of secondary electrons. The secondary electrons enter the plasma and ionize neutral Ar atoms thereby sustaining the plasma. The probability for ion production by energetic electrons (>100 eV) passing through low pressure argon (<2 mT) is low. The probability of secondary electrons ionizing enough argon atoms to produce more electrons from the target can only be increased by increasing the working (Ar) pressure. However, making the pressure too high, would decrease the deposition rate because significant numbers of sputtered atoms would not be able to penetrate the discharge atmosphere. Some would even be reflected back to the target.[16,17] Target atoms that are able to pass through the plasma deposit on a substrate and surfaces surrounding the substrate.[18,19] The substrate is any material intentionally positioned to collect the sputtered material.

2.2 D.C. Magnetron Sputtering

When the electric field is the result of a d.c. voltage source, the negative terminal is applied to the target (cathode) and the positive side of the power source is connected to the substrate holder (anode). The target and substrate are separated by 5 to 10 cm but most of the volume between the target and substrate is occupied by the electrically neutral plasma. Visually the plasma appears as a glow discharge with a dark space over the cathode. The applied potential is concentrated in the dark space giving rise to a large electric field. Current flow is the result of Ar^+ ions from the plasma to the target and electrons

from the plasma to the substrate. Electrons cause the substrate to heat up when they impact it. To prevent this, a magnetic field is applied in such a way as to confine the electrons to the vicinity of the target. This variation to the standard sputtering arrangement is called magnetron sputtering.[19,20,21]

If the plasma contains atoms other than argon, they may react with the target at its surface. This includes contaminates from out-gassing and leaks. Since oxygen is usually present in trace amounts and is highly reactive, the deposited film is usually oxygen contaminated to some degree unless a very high vacuum ($< 10^{-8}$ Torr) can be attained. A second gas may be intentionally mixed with the argon so that the deposited material is a compound of the target material and the second gas. This is called reactive sputtering.

2.3 RF Magnetron Sputtering

If one tries to sputter an electrically insulating material by making it the target in a standard d.c. arrangement, positive charge accumulates on its surface and the sputter yield decreases to zero. This can be overcome by applying an a.c. potential to the target instead of a d.c. potential. The magnetic field is also applied as in the case of d.c. sputtering. As the potential alternates, the electrodes reverse their cathode-anode roles every half cycle and there is a dark space over each electrode. The frequency of the oscillations must be high enough to prevent charge accumulation during that part of a cycle the electrode serves as the cathode. The Federal Communications Commission has allocated the r.f. frequency range of 10 to 20 MHz for industrial, scientific, and medical applications and most r.f. sputtering tools operate at 13.560 MHz. RF sputtering is the preferred process to d.c. sputtering because of its versatility at depositing conducting and semiconducting as well as insulating materials. Plasma electrons move back and forth past a sea of relatively stationary ions under the influence of the applied potential but mostly confined by the magnetic field. The dark space separating the charge on an electrode from that of the plasma can be modeled as a capacitor shunted by a diode and a resistor. The diode is included to account for electron current when the electrode is positive and the resistor is included to account for ion current when the electrode is negatively charged. The total ion and electron currents at a given electrode during an r.f. cycle must balance to zero. The r.f. power supply circuit is inductively coupled via a matching network to the plasma and electrodes as

though they were replaced by their electronic equivalents. Efficient power transfer requires that the r.f. power supply operate into a resistive load. The purpose of the matching network is to introduce inductance and/or capacitance into the circuit to match the power supply and the plasma impedances. This is called tuning the power supply, and a tuned power supply delivers maximum power (called forward power) to the plasma. Some r.f. sputtering systems feature automatic tuning as an operational convenience but quite often the user has to manually tune it.[22]

2.4 Sputter Parameters for the Aluminum Nitride Film

Two sputtering systems were used to deposit sample films for evaluation. A CVC 601 and a Perkin-Elmer 2400 both equipped with an rf power supply and a Brooks flow controller/monitor. Aluminum nitride film was deposited by reactively sputtering Al (99.999% pure) in an argon/nitrogen gas mixture. The substrates were, 1 x 2 in. silica plates, and silicon wafers.

2.4.1 Operational Particulars

The CVC 601 is a multi-target rf sputtering system. The target is arranged to sputter upward and the substrate holder, the rotor, can be stationary or rotating during sputtering. The flow rate was monitored by a dual channel Brooks flow meter and the Ar and N_2 flows were based on a total gas flow of approximately 206 sccm. The N_2 flow was the meter setting x2 and the Ar flow was the meter setting x2.8. The base and sputter pressures of the chamber were measured by an ion gauge and a pirani gauge respectively and displayed on the control panel. Pre-heat and sputter times were preset on a count-down timer. Sputtering was started after the designated pre-sputter time had lapsed by manually opening the shutter. The rf power was set to the desired level and the plasma was tuned during the pre-sputter period. Plasma tuning was done manually via shunt and series adjustments to achieve minimum reflected power of ~50W. The shunt/series readings were noted on each run to detect performance degradation in the tuning network.

The PE 2400 is also a rf-powered multiple-target sputtering system. The target, however, is arranged to sputter downward and the table could be rotating or stationary during sputtering. A Brooks dual channel flow rate controller was also used to maintain a total gas flow of 30 sccm. The Ar flow was the meter setting x1.44 and the N_2 flow was the

actual meter reading. The chamber base pressure was measured by an ion gauge that is switch activated. The plasma was automatically tuned and the level of reflected power was indicated on a microammeter. The sputtering period was controlled by a count-down timer.

The PE sputterer also has the capability of allowing the user to select one of four table positions for a stationary sputtering session. Between sputtering sessions the user can change sputtering gas or the mixture.

Trial sputter parameters were devised after those published by others studying reactively sputtered AlN and initial test runs were performed on the CVC 601. The films were deposited in an $Ar:N_2$ environment at ratios varying from 3:1 to 1:1. The objective was to determine the effect of the $Ar:N_2$ gas ratio on film thickness and index of refraction (NR) and to identify the best ratio that would consistently produce film with a thickness of ~1000 Å and NR of ~2.08. The other sputtering parameters are shown in Table 2-1.

Parameter	Value (or Range)
Base Pres.	~ 3.0×10^{-6} T
Sputter Pres.	4.6 mT
Pre-heat Time	40 min. @ 300 C
pre-/sputt Time	10/30 min.
Sputter Power	2.0 kW
Shunt/Series	5.0/8.9

Table 2-1 CVC 601 Sputtering Parameters.

2.5 Experimental Procedure

It was subsequently decided to sputter all film samples on the PE 2400. The sputtering parameters used were derived from the CVC trials and they are given in Table 2-2. Before depositing film samples for the investigation, trial samples were deposited to find out if the film would stand up to the wet and dry processing environments frequently encountered in microelectronics. One film sample on Si substrate was subjected to H_2O_2

wash, buffered HF solution, photo resist, exposure and development, and then ashing. Film samples on fused silica were also ashed, washed in H_2O_2. Adverse effects to samples on Si were detected by changes in the refractive index and thickness as measured by ellipsometry before and after treatment. Variations in samples on fused silica were detected by comparing the UV-Vis spectra before and after treatment.

Parameter	Value or Range
Base Pressure	$\sim 5.0 \times 10^{-7}$ T
Sputter Pressure	~ 10 mT
Forward Pwr	500 W
pre-/sputt Time	10/20 min.
$Ar:N_2$ (meter)	10.4:15.0

Table 2-2 Summary of P-E 2400 Sputtering Parameters.

Film samples were deposited on three n+ doped (100) 4" silicon wafers, 1" x 2" fused silica plates and 2" (111) Si wafers. The sputter runs are listed in Table 2-3.

To minimize the surface oxide layer on the Si wafers, they were cleaned in buffered HF (50:1) for 10 min. and blown dry. Within 20 min. of their removal from the HF solution, they were put into the sputter chamber which was immediately evacuated. In addition to being cleaned in buffered HF, FTIR background spectra of the 2" wafers (the substrates) were obtained from a Perkin-Elmer 1770 FTIR spectrometer prior to being put into the sputter chamber. Each fused silica plate was sputtered with a 2" control wafer so that the deposition thickness could be measured by the ellipsometer. Each sputter session was preceded by 10 minutes of pre-sputtering onto a dummy wafer on table position #1.

All film samples on 2" wafers samples were scanned by the FTIR spectrometer using their respective substrate spectra as the reference. This gave the as-deposited (pre-anneal) IR spectra.

The transmittance and reflectance of the as-deposited film samples were obtained by scanning the silica plates from 190 - 900 nm in a Perkin-Elmer UV-VIS spectrometer.

Run	Table Position	Substrate	Sample Name	Treatment
#1	#2	n+ 4" Si	AON54	760 C 30 min.
	#3	"	AON55	800 C
	#4	"	AON56	850 C
#2	#2	2" (111) Si	AON61	760 C 30 min.
	#3	2" (111) Si	AON62	800 C
	#4	"	AON63	850 C
		"	AON64	Left as-dep
#3	#2	Silica	AON65	850 C
		2" Si	AON69	850 C
	#3	Silica	AON66	800 C
		2" Si	AON70	800 C
	#4	Silica,	AON67	760 C
		Silica	AON68	Left as-dep
		2" Si	AON71	broken
#4	#2	n+ 4" Si	AON57	850 C
	#3	2" Si	AON72	760 C
		Silica	AON75	760 C
		Silica	AON76	not used
	#4	2" Si	AON73	not used
		2" Si	AON74	not used

Table 2-3 Summary of Evaluation Samples.

The 4" wafers were annealed at 760° C ,800° C and 850° C respectively for 30 minutes in a diffusion furnace. Nitrogen was flowing at 5 lpm. After this, aluminum was evaporated over the film, patterned via photolithography process to form Al-AlN-n^+Si capacitors. The capacitors were square and circular patterns ranging in size from 0.1 to 2.0 mm^2.

The substrate was grounded and the plate of a capacitor was dc biased to place the n^+-doped silicon substrate in accumulation, ~ +3.0 v. Capacitances were read from an analog meter as a 1 MHz on a 25 mV dc signal was applied. These measured capacitances were plotted against plate area to extract the out-of-plane dielectric constant. The dielectric constant of each film sample was calculated from the slope of the respective line.

The breakdown voltage of each film was measured by applying a d.c. potential across a capacitor and in series with a current limiting resistor. The voltage was increased until the dielectric broke down. That final potential less the potential dropped across the resistor is the breakdown potential of the device.

Three 2" wafers and three silica plates were also annealed at the three temperatures; 760°, 800°, and 850 °C on different runs than the 4" wafers.

The infrared spectra of the annealed film on the 2" wafers were obtained by scanning them relative to their respective substrate spectra in the FTIR Spectrometer. This gave the post-anneal IR spectra.

Then post reflectance and transmittance of the annealed films were obtained by scanning the silica plates in the UV-VIS spectrometer once more. These spectra were numerically evaluated by a software utility to determine the refractive index and extinction coefficient of the film.

Annealed and as-deposited samples on silicon wafers were topographically analyzed by Atomic Force Microscopy (AFM) and chemically analyzed by Auger Electron Spectroscopy (AES).

An annealed or as-deposited film sample was prepared for x-ray diffraction analysis by mounting a appropriately sized section of the 2" wafer on a glass plate, so that the assembly fitted comfortably in the sample compartment of the x-ray diffractometer. The x-ray diffraction spectra of the film samples were taken in steps of 0.05° over an angular range of $2\theta = 30°-70°$ at a slew rate of 2.4 deg/min. A background spectrum was also obtained from a blank piece of the 2" substrate ((111) silicon wafer) mounted on the same glass plate as the film samples.

2.6 The Atomistic Theory of Optical Properties

The Hagen-Reubens equation of reflectivity predicted experimental results of metals in the far infrared quite effectively. It was based on the continuum theory which considers only macroscopic properties. However, at frequencies $> 10^{13}$ s^{-1} the experimental reflectivity of metals falls faster than predicted by the equation. Drude sought an explanation by considering the motions of electrons under the influence of an electric field and their interaction with atoms in a non-ideal lattice. This approach is called the atomistic model and treated the electrons in a crystal lattice as either free, damped, or bound to their nuclei. Different proportions of each effect are combined to give a very good explanation of a material's optical spectra.

2.6.1 Free Electrons

Drude's first approach to determining the reflectivity of metals was to treat the electrons as free to vibrate without hindrance under the influence of an electric field. The next step will be to apply a damping factor to this motion.

Assuming the electrons are affected by plane polarized radiation whose strength at anytime, t, is given by

$$\mathcal{E} = \mathcal{E}_{\circ} e^{i\omega t} \qquad (2\text{-}1)$$

where $\omega = 2\pi\nu$ is the angular frequency and $\mathcal{E}_{\circ}$ is the maximum amplitude of the field. The force exerted on an electron by this field, $e\mathcal{E}$ where e is the electronic charge, displaces it in one dimension according to the equation of motion,

$$m \frac{d^2 x}{dt^2} = e\mathcal{E} = e\mathcal{E}_{\circ} e^{i\omega t} \qquad (2\text{-}2)$$

where m is the mass of the electron. The electron displacement as a function of the incident electric field is the solution of this 2nd order differential equation,

$$x = - \frac{e\mathcal{E}}{4\pi^2 m\nu^2} . \qquad (2\text{-}3)$$

The dipole moment of the electron is equal to the product of its displacement, x, and the electronic charge, e. The total dipole moment per unit volume of material is the polarization, $P = exN_f$, where N_f is the free electron density. The dielectric constant (which is also

the square of the index of refraction) can be determined directly from the polarization and the electric field strength using

$$\hat{\varepsilon} = 1 + \frac{4\pi P}{\mathcal{E}} \qquad (2\text{-}4)$$

so,

$$\hat{\varepsilon} = 1 - \frac{e^2 N_f}{\pi m \nu^2}. \qquad (2\text{-}5)$$

But,

$$\hat{\varepsilon} = \hat{n}^2 = n^2 - \kappa^2 - i2n\kappa \qquad (2\text{-}6)$$

where, $\hat{n}$, is the complex index of refraction which consists of the real index of refraction, n, and a complex part, κ, called the extinction coefficient (or attenuation index). Since the right-hand side of eq. (2-5) is real, $\hat{n}^2$ is also real. At high frequencies, $\hat{n}$ is essentially real (≈ 1.0), and essentially imaginary at low frequencies.

From this index of refraction, the reflection at normal incidence is,

$$R = \frac{(n-1)^2 + \kappa^2}{(n+1)^2 + \kappa^2}. \qquad (2\text{-}7)$$

So, for small frequencies, n = 0, and

$$R \cong \frac{1 + \kappa^2}{1 + \kappa^2} = 1. \qquad (2\text{-}8)$$

For large frequencies, $\kappa = 0$, therefore,

$$R \cong \frac{(n-1)^2}{(n+1)^2} \qquad (2\text{-}9)$$

This is consistent with experimental observation for some materials. but does not hold for most.[23]

2.6.2 Bound Electrons with Damping

If the electron motion is damped by a force that is proportional to their velocity, the equation of motion becomes

$$m \frac{d^2 x}{dt^2} + \gamma \frac{dx}{dt} = e\mathcal{E}_o e^{i\omega t} \qquad (2\text{-}10)$$

where γ is a proportionality constant called the damping coefficient. Under the influence of

a constant electric field, $dx/dt = v_d$ the drift velocity, a constant which is proportional to the conductivity, σ_0 , of the material. Since $d^2x/dt^2 = 0$,

$$v_d = \frac{dx}{dt} = \frac{e\mathcal{E}}{\gamma} \qquad (2\text{-}11)$$

and the drift velocity is given as

$$v_d = \frac{\sigma_0 \mathcal{E}}{eN_f} \qquad (2\text{-}12)$$

$$\gamma = \frac{N_f e^2}{\sigma_0} \qquad (2\text{-}13)$$

More will be said about the damping coefficient later.

If the electrons are bound in the vicinity of the nucleus, as would be the case for a dielectric, the electric field of the incident radiation merely displaces the electron cloud around the nucleus of the atom. This implies a spring force in addition to the inertial and damping forces. According to Hooke's Law, the spring force is proportional to the displacement from equilibrium, x, That is, $F_s = -Kx$, where K is the proportionality constant between the displacement and the spring force. Accounting for the spring force, the equation of motion becomes

$$m\frac{d^2x}{dt^2} + \gamma\frac{dx}{dt} + Kx = e\mathcal{E}_\circ e^{i\omega t}. \qquad (2\text{-}14)$$

The particular solution to this differential equation can be found by assuming a solution of the form, $x = ae^{i\omega t}$ from which it is determined that

$$x = \frac{e\mathcal{E}_\circ e^{i(\omega t - \varphi)}}{\sqrt{m^2(k/m - \omega^2)^2 - \gamma^2 \omega}} \qquad (2\text{-}15)$$

where

$$\varphi = \tan^{-1}\left(\frac{\gamma\omega}{m(k/m - \omega^2)}\right) \qquad (2\text{-}16)$$

is the phase angle.

Therefore, the dielectric constant becomes,

$$\hat{\varepsilon} = 1 + 4\pi \frac{P}{\varepsilon} = \frac{4\pi e^2 N_a}{\sqrt{m^2(k/m - \omega^2)^2 - \gamma^2\omega}} e^{i(\omega t - \varphi)} \qquad (2\text{-}17)$$

where N_a is the dipole density which for a dielectric is the atomic density, and $k/m = \omega_o^2$ is the resonant frequency of the oscillator. Since $\hat{\varepsilon} = \hat{n}^2 = n^2 - \kappa^2 - i2n\kappa$, the real and imaginary parts of the dielectric constant are

$$\varepsilon_1 = n^2 - \kappa^2 =$$
$$1 + \frac{4\pi e^2 m N_a(\omega_o^2 - \omega^2)}{m^2(\omega_o^2 - \omega^2)^2 + \gamma^2\omega^2} = 1 + \frac{4\pi e^2 m N_a(v_o^2 - v^2)}{4\pi^2 m^2(v_o^2 - v^2)^2 + \gamma^2 v^2} \qquad (2\text{-}18)$$

and

$$\varepsilon_2 = 2n\kappa = \frac{4\pi e^2 m N_a \gamma\omega}{m^2(\omega_o^2 - \omega^2)^2 + \gamma^2\omega^2} = \frac{2\pi e^2 m N_a \gamma v}{4\pi^2 m^2(v_o^2 - v^2)^2 + \gamma^2 v^2} \qquad (2\text{-}19)$$

where the substitutions $e^{i\varphi} = \cos\varphi - i\sin\varphi$, $\cos\varphi = 1/\sqrt{1 + \tan^2\varphi}$ and $\sin\varphi = \tan\varphi / \sqrt{1 + \tan^2\varphi}$ were made.

Plots of eqs. (2-18) and (2-19) are shown in Figure 2-1. It is seen that at the resonant frequency, v_o, absorption is maximum but drops to zero at frequencies far from the resonant frequency. The polarization approaches, $\varepsilon_1 = 1$, far from the resonant frequency so that in this limit, $\kappa \sim 0$ and $n \sim 1.0$. Both these phenomena have been observed experimentally.[23]
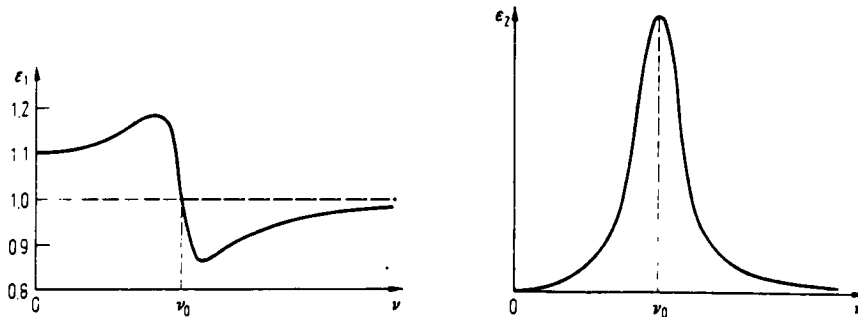
Figure 2-1   Frequency dependence of polarization and absorption.[23]

2.7 Macroscopic Characteristics and the Clausius-Mossotti Relation

If a material is non-crystalline, the effects of an external field must be averaged over a volume large enough to be representative of the material. When an electric field, $\mathcal{E}_o$, is applied to an initially unpolarized non-crystalline dielectric material, surface charges on the dielectric gives rise to a depolarization field, $\mathcal{E}_1$, which opposes the applied field. This new field is proportional to the induced surface charge, $\sigma = \mathbf{n} \cdot \mathbf{P}$, where $\mathbf{n}$ is the unit normal to the surface, so

$$\mathcal{E}_1 = -c|\sigma| = -cP \text{ (CGS)}$$
$$\mathcal{E}_1 = -\frac{c\sigma}{\varepsilon_o} = -\frac{cP}{\varepsilon_o} \text{ (SI)} \tag{2-20}$$

The factor c is related to the shape of the dielectric medium. For elliptical, spherical, or disc shaped symmetry a factor of 1/3 (SI) or $4\pi/3$ (CGS) is applicable.

The field at the site of an atom within the medium, the local field, is not the applied field, but an adjustment to the sum of the applied field and the depolarization field, $\mathcal{E}_m$. Therefore,

$$\mathcal{E}_{loc} = \mathcal{E}_m + \mathcal{E}_c \tag{2-21}$$

where

$$\mathcal{E}_m = \mathcal{E}_o + \mathcal{E}_1. \tag{2-22}$$

The adjustment field, $\mathcal{E}_c$, is the net field due to dipole charges on the surface of an imaginary sphere surrounding the atom plus the field due to dipoles inside the sphere. The field due to charges on the surface of the imaginary sphere is $(4\pi/3)\mathbf{P}$, by integration over that spherical surface. As it turns out, for a material of cubic crystal structure, the contribution to the local field from dipoles inside the sphere is zero due to symmetry. Therefore, the resultant local field is,

$$\mathcal{E}_{loc} = \mathcal{E}_m + \frac{\mathbf{P}}{3\varepsilon_o} \text{ (CGS)}$$
$$\mathcal{E}_{loc} = \mathcal{E}_m + \frac{\mathbf{P}}{3\varepsilon_o} \text{ (SI)} \tag{2-23}$$

is the field at the center of the imaginary cavity due to dipole surface charges.

Polarization is a reflection of a material's microscopic properties. From Maxwell's displacement,

$$\mathbf{D} = \xi\boldsymbol{\mathcal{E}} = \boldsymbol{\mathcal{E}} + 4\pi\mathbf{P} \text{ (CGS)}$$
$$\mathbf{D} = \xi\varepsilon_0\boldsymbol{\mathcal{E}} = \varepsilon_0\boldsymbol{\mathcal{E}} + \mathbf{P} \text{ (SI)}$$

(2-24)

where ξ is the dielectric constant. If we let,

$$\mathbf{P} = \chi\boldsymbol{\mathcal{E}} \text{ (CGS)}$$
$$\mathbf{P} = \varepsilon_0\chi\boldsymbol{\mathcal{E}} \text{ (SI)}$$

(2-25)

then

$$\mathbf{D} = (1 + 4\pi\chi)\boldsymbol{\mathcal{E}} \text{ (CGS)}$$
$$\mathbf{D} = (1 + \chi)\varepsilon_0\boldsymbol{\mathcal{E}} \text{ (SI)}$$

(2-26)

so

$$\xi = 1 + 4\pi\chi \text{ (CGS)}$$
$$\xi = 1 + \chi \text{ (SI)}$$

(2-27)

where χ is the susceptibility of the medium, a unitless scalar in CGS and SI. Since polarization and dipole moment are related by,

$$\mathbf{P} = \sum_j N_j \mathbf{p}_j$$

(2-28)

and

$$\mathbf{p} = \alpha\boldsymbol{\mathcal{E}}_{\text{loc}}$$

(2-29)

then

$$\mathbf{P} = \sum_j N_j\alpha_j\boldsymbol{\mathcal{E}}_{\text{loc}}(j) = \left(\sum_j N_j\alpha_j\right)\left(1 + \frac{4\pi}{3}\chi\right)\boldsymbol{\mathcal{E}}_{\text{loc}} \text{ (CGS)}$$
$$\mathbf{P} = \left(\sum_j N\alpha_j\right)(1 + \chi)\varepsilon_0\boldsymbol{\mathcal{E}}_{\text{loc}} \text{ (SI)}$$

(2-30)

so,

$$\frac{\xi - 1}{\xi + 2} = \frac{4\pi}{3}\sum N_j\alpha_j \text{ (CGS)}$$
$$\frac{\xi - 1}{\xi + 2} = \frac{1}{3\varepsilon_0}\sum N_j\alpha_j \text{ (SI)}$$

(2-31)

which is the Clausius-Mossotti (C-M) equation. It relates the dielectric constant of a well-

behaved non-crystalline solid to the volume concentration, N_j, and the polarizability, α_j, of each type atom constituent of the material. is the and $\mathcal{E}_{loc}$ is the local electric field at the jth atom. Polarizability has the units of [length^3] in CGS and [farad-m^2] in SI but, the CGS version of the Clausius-Mossotti relation will be used throughout the remainder of this report because it is the most commonly encountered.[24,25]

If the medium is subjected to an oscillatory field, we may write

$$\mathbf{p} = e\mathbf{x}(t) = \frac{e^2 \mathcal{E}_{loc}}{m(\omega_0^2 - \omega^2) + i\gamma\omega} \tag{2-32}$$

and

$$\mathbf{P} = \sum_j N_j f_j \mathbf{p} = \mathcal{E}_{loc} \sum_j \frac{N_j f_j e^2}{m(\omega_{oj}^2 - \omega^2) + i\gamma_j \omega} \tag{2-33}$$

in accordance with the theory established in section 2.6.2. The f_j factor is the volume fraction, N_j, of the jth atom vibrating with resonance frequency, ω_{oj}, and damping coefficient, γ_j. From eqs. (2-32) and (2-33) above,

$$\mathbf{P} = \left(\mathcal{E} + \frac{4\pi}{3}\mathbf{P}\right) \sum_j \frac{N_j f_j e^2}{m(\omega_{oj}^2 - \omega^2) + i\gamma_j \omega} \quad \text{(CGS)} \tag{2-34}$$

implying that ε, χ and α are now complex quantities, so eq. (2-27) should be rewritten as,

$$\hat{\xi} = 1 + 4\pi\hat{\chi} \text{ (CGS)}$$
$$\hat{\xi} = 1 + \hat{\chi} \text{ (SI)} \tag{2-35}$$

The C-M relation becomes,

$$\frac{\hat{\xi} - 1}{\hat{\xi} + 2} = \left(\frac{4\pi}{3}\right) \sum_j \frac{N_j f_j e^2}{m(\omega_{oj}^2 - \omega^2) + i\gamma_j \omega} \quad \text{(CGS)}$$

$$\frac{\hat{\xi} - 1}{\hat{\xi} + 1} = \left(\frac{1}{3\varepsilon_o}\right) \sum_j \frac{N_j f_j e^2}{m(\omega_{oj}^2 - \omega^2) + i\gamma_j \omega} \quad \text{(SI)} \tag{2-36}$$

respectively.

The polarizability, α, may consist of up to three components cumulatively affecting polarization. In the visible-UV part of the spectrum the electron shell is displaced by the electric field of the radiation. This is the electronic component and is the only polarization experienced by elemental medium. In the infrared region, charged ions and the electron shell are displaced by the electric field and this called ionic polarization. Finally, molecules with a permanent dipole moment experience a torque forcing them into alignment with the electric field. This called dipolar or orientational polarization and arises under the influence of microwave radiation. Ionic and dipolar contributions are negligible at optical frequencies because of the greater inertia of ions and molecules. Orientational polarization is also highly temperature dependent but, will be disregarded since this study does not involve molecules with permanent dipole moments. A diagram of the frequency dependency of each component is shown in Figure 2-2.[24,26]

The total polarizability in the frequency range 1-10 MHz is a combination of the electronic and ionic polarizabilities, α_e and α_i, respectively and will be referred to as the dielectric polarizability, α_D. The C-M relation says that the dielectric polarizability of any material is an additive combination of the dielectric polarizabilities of each constituent
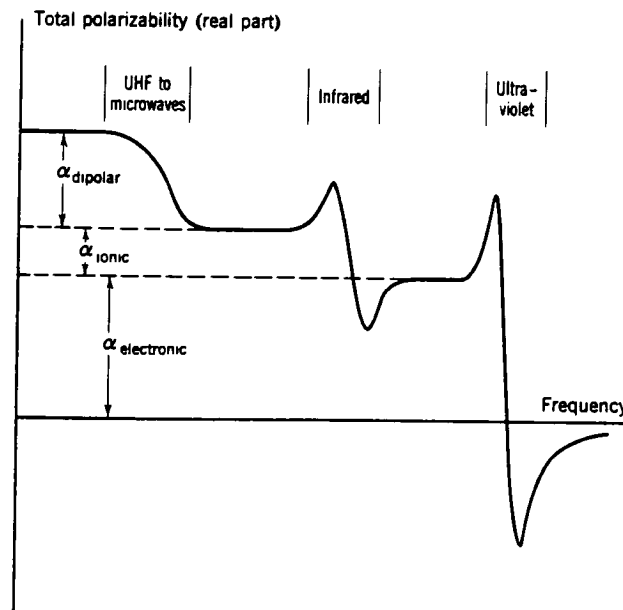
Figure 2-2   The Frequency dependence of the three Components of Polarization.[24]

weighted by its volume density, N_j. The volume density of each constituent is determined

from the bulk density of the material and its molecular weight. So, the C-M relation can be written as

$$\frac{\xi - 1}{\xi + 2} = \frac{4\pi}{3V} \sum n_j \alpha_{Dj}$$ (2-37)

where n_j is the number of atoms of type j in the molecular formula of the material (i.e. 2 M atoms and 1 X atom in M_2X), and V is the volume (same units as polarizability which is typically $Å^3$) occupied by one molecule.[26]

In the optical spectrum (visible, UV and higher frequencies), the electronic polarizability alone effects the dielectric constant. The C-M relation becomes,

$$\frac{n^2 - 1}{n^2 + 2} = \frac{4\pi}{3} \sum N_j \alpha_{ej}$$ (2-38)

where $\xi = n^2$ was applied.

2.8 Frequency Spectra

Eqs. (2-18) and (2-19) can be viewed as the complex fourier transform of an oscillation with a resonant frequency of ω_0 and a damping coefficient of γ_0. Eqs. (2-18) and (2-19) can be rewritten as:

$$\varepsilon_1 - 1 = \frac{4\pi e^2 m N_a (\omega_0^2 - \omega^2)}{m^2 (\omega_0^2 - \omega^2)^2 + \gamma^2 \omega^2} = \frac{4\pi e^2 N_a}{m} \left(\frac{(\omega_0^2 - \omega^2)}{(\omega_0^2 - \omega^2)^2 + \Gamma^2 \omega^2} \right)$$ (2-39)

and

$$\varepsilon_2 = \frac{4\pi e^2 m N_a \gamma \omega}{m^2 (\omega_0^2 - \omega^2)^2 + \gamma^2 \omega^2} = \frac{4\pi e^2 N_a}{m} \left(\frac{\Gamma \omega}{(\omega_0^2 - \omega^2)^2 + \Gamma^2 \omega^2} \right)$$ (2-40)

respectively, where $\Gamma = \gamma / m$, and $1/\Gamma$ is the relaxation time which is a measure of the environment between the vibrating atoms. The quantities in parentheses are known as the Lorentzian dispersion,

$$D(\omega) = \left(\frac{(\omega_0^2 - \omega^2)}{(\omega_0^2 - \omega^2)^2 + \Gamma^2 \omega^2} \right)$$ (2-41)

and absorption,

$$A(\omega) = \left(\frac{\Gamma\omega}{(\omega_0^2 - \omega^2)^2 + \Gamma^2\omega^2} \right) \qquad (2\text{-}42)$$

respectively and occur universally in spectra. The full-width at half maximum of the absorption and the spacing between the dispersion peaks are both given by Γ so the resonant frequency and the relaxation time can be extracted from either spectra. A sample plot of each is shown in Figure 2-3.
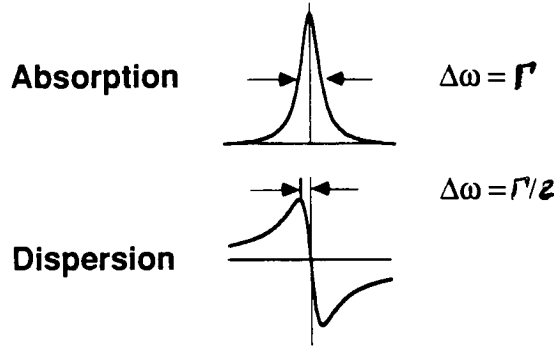
Figure 2-3 Dispersion and Absorption Lorentzian.[27]

A remarkable property about the Lorentzian spectrum is that a plot of D(w) vs. A(w) for an isolated line yields a circle that is tangent to the origin with a diameter equal to the absorption peak height. It is shown in Figure 2-4. This plot is useful because it can discriminate against various line broadening mechanisms. Two or more over-lapping Lorentzians of the same width but different peak position will produce a plot displaced outside its reference circle, whereas two overlapping Lorentzians of the same position but different width will displace the plot inside its reference circle. This illustrated in Figure 2-5.
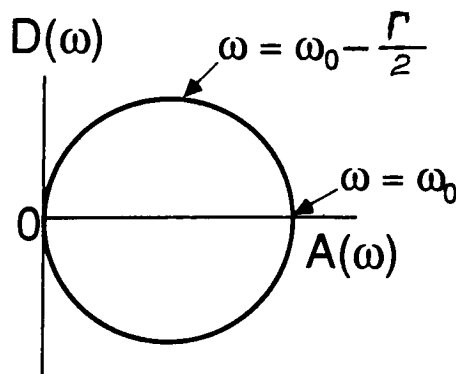
Figure 2-4 Dispersion vs. Absorption.[27]
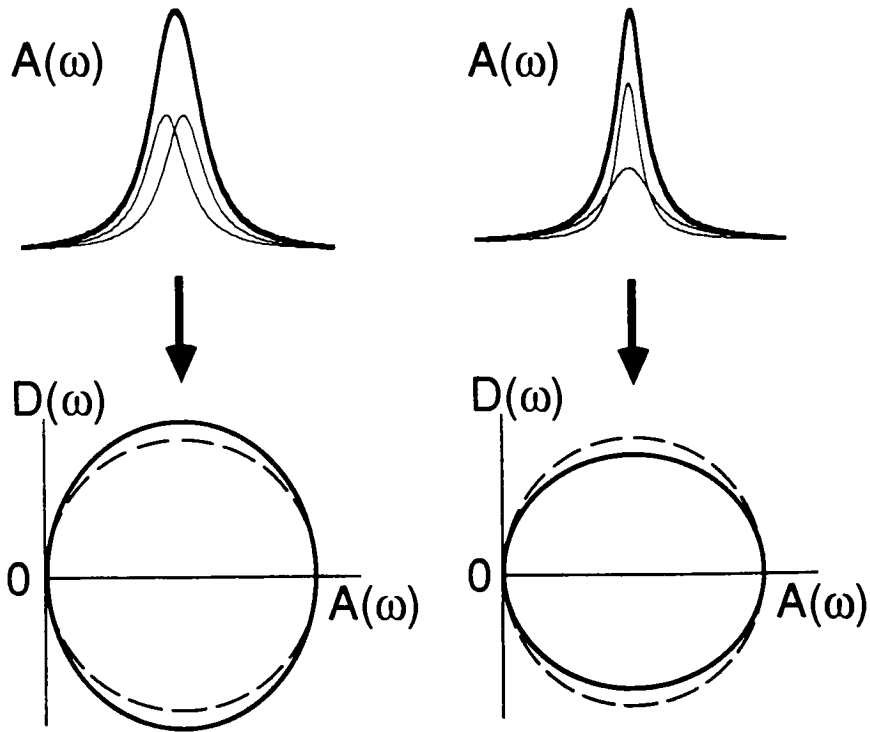
Figure 2-5 Detecting Lorentzian Shift and broadening.[27]

The natural frequencies of atomic vibrations ω_o (or ν_o) have been shown to be the fundamental property responsible for the characteristic transmission, absorption, and reflection spectra of a material. For most materials, there are a number of vibrational modes, each having a resonant frequency of ω_{oi}, a damping constant of γ_i and an oscillator strength of f_i. Each oscillator contributes to the dielectric constant so that the real and imaginary parts can be written as,

$$\varepsilon_1 = 1 + \frac{4\pi e^2 N_a}{m} \sum_i \left(\frac{f_i (\omega_{oi}^2 - \omega^2)}{(\omega_{oi}^2 - \omega^2)^2 + \Gamma_i^2 \omega^2} \right) \tag{2-43}$$

and

$$\varepsilon_2 = \frac{4\pi e^2 N_a}{m} \sum_i \left(\frac{f_i \Gamma_i \omega}{(\omega_o^2 - \omega^2)^2 + \Gamma_i^2 \omega^2} \right) \tag{2-44}$$

respectively. All of the resonant vibrational frequencies of a material within a specific frequency bandwidth form a spectrum that uniquely "fingerprints" that material.

In reality, every material exhibits some degree of free electron behavior and a certain degree of oscillator behavior. So a material's true polarization and absorption is a proportional or statistical combination of these two conditions.[23,27]

2.9 Quantum Mechanical Treatment

It is not clear from a classical point of view why electrons in a material behave as free electrons at one frequency and as if they are bound to the atoms at a higher frequency. An unconstrained interpretation of the behavior of electrons can be obtained by applying quantum mechanics to the periodic potential of a crystal lattice. The alternating electric field of radiation which impinges on the material and perturbs the potential field of the lattice. So, a correction, V', must be added to the lattice potential, V_o, giving a total potential of $V = V_0 + V'$ Once again, the incident radiation is assumed to be plane polarized with field strength $\mathcal{E} = A\cos(\omega t)$. The perturbation potential energy is,

$$V' = e\mathcal{E}x = exA\cos(\omega t) \tag{2-45}$$

since energy = force x displacement.

The time dependent Schrodinger wave equation is applicable here because the potential varies with time,

$$\nabla^2\Psi - \frac{2m}{\hbar^2}V\Psi - i\frac{2m}{\hbar}\frac{\partial\Psi}{\partial t} = 0 \tag{2-46}$$

which with $V = V_0 + V'$ becomes,

$$\nabla^2\Psi - \frac{2m}{\hbar^2}V_0\Psi - i\frac{2m}{\hbar}\frac{\partial\Psi}{\partial t} = \frac{2m}{\hbar^2}exA\frac{1}{2}(e^{i\omega t} + e^{-i\omega t})\Psi \tag{2-47}$$

after substituting for $\cos\omega t = (e^{i\omega t} + e^{-i\omega t})/2$.

The general solution of eq. (2-47) is,

$$\Psi = \psi_i^0(x,y,z)e^{i\omega_i t} + \psi_\pm(x,y,z)e^{i(\omega_i \pm \omega)t} \tag{2-48}$$

Using,

$$x\psi_i^0 = a_{1i}\psi_1^0 + a_{2i}\psi_2^0 + \cdots + a_{ni}\psi_n^0 + \cdots = \sum_n a_{ni}\psi_i^0 \tag{2-49}$$

and expressing the perturbed wave function, $\psi_\pm$, as a series of the unperturbed wave functions,

$$\Psi_{\pm} = \sum b_{\pm n} \psi_n^0 , \tag{2-50}$$

the wave function is determined to be

$$\Psi = \psi_i^0 e^{i\omega_i t} + \frac{1}{h} \sum_n eA a_{ni} \psi_n^0 \left[\frac{e^{i(\omega_i - \omega)t}}{\nu_{ni} + \nu} + \frac{e^{i(\omega_i - \omega)t}}{\nu_{ni} - \nu} \right] \tag{2-51}$$

where $\nu_{ni} = \nu_n - \nu_i$

The polarization, P, in quantum mechanics is,

$$P = Ne\overline{x} = Ne\int x\Psi\Psi^* dv \tag{2-52}$$

and considering only the time-dependent terms

$$\Psi\Psi^* = \frac{eA}{2h} \left[\sum_n a_{ni}^* \psi_n^{0*} \psi_i^0 \underbrace{\left(\frac{e^{-i\omega t}}{\nu_{ni} + \nu} + \frac{e^{i\omega t}}{\nu_{ni} - \nu} \right)}_{S} + \right.$$

$$\left. \sum_n a_{ni} \psi_n^0 \psi_i^{0*} \underbrace{\left(\frac{e^{i\omega t}}{\nu_{ni} + \nu} + \frac{e^{-i\omega t}}{\nu_{ni} - \nu} \right)}_{T} \right]. \tag{2-53}$$

After some calculus and using the previous methodology we find,

$$\varepsilon_1 = n^2 - \kappa^2 = 1 + \frac{4Ne^2}{\hbar} \sum_n a_{ni}^2 \frac{\nu_{ni}}{\nu_{ni}^2 - \nu^2} . \tag{2-54}$$

This is equivalent in form to the dispersion relation eq. (2-18) with the oscillator strength given by

$$f_i = \frac{4\pi m}{\hbar} a_{ni}^2 \nu_{ni} . \tag{2-55}$$

In the quantum mechanical approach, the resonance frequency, n_{oi}, has be replaced with n_{ni}, which is proportional to the energy of an allowed electron transition from the nth to the ith energy band. The parameter, a_{ni}, is proportional to the probability of an electron transition from the nth to the ith band. Therefore, the oscillator strength is essentially the probability of that interband transition.[23]

2.10 Band Structure and Optical Characteristics

Although electrons have been treated thus far as particles, in solids they form bands due to the periodic potential. The electrical properties of a solid can be explained by its band structure and the band structure influences the optical properties. A material's transmittance and/or reflectance over UV/visible wavelengths are exploited to obtain its refractive index and extinction coefficient, n and κ respectively. The absorption coefficient, which is derived from the extinction coefficient, is a function of it's excitation states.

2.10.1 Interpretation of the Spectral Characteristics

A film's transmittance is a function of n and κ of both the film and the substrate on which it is supported. By application of Fresnel's equations, the transmittance of radiation through a film and its substrate is given by,

$$T(\omega) = \frac{T_{23} \cdot \hat{t}_{012}(\omega) \cdot \hat{t}_{012}^*(\omega) \cdot \exp(-\alpha_2 d_2)}{\left[1 - R_{210}(\omega) \cdot R_{23}(\omega) \cdot \exp(-2\alpha_2 d_2)\right]}. \qquad (2\text{-}56)$$

assuming that the coherence length of the source is less than the substrate thickness, d_2. If the source radiation is coherent throughout the substrate, interference effects would introduce a phase shift along with the absorption. The subscripts refer to the model of a thin film on a thick substrate in Figure 2-6. The refractive indices, n_0 and n_3 represent air which is set at 1.0. The refractive indices of the film and substrate, $\hat{n}_1(\omega)$ and $\hat{n}_2(\omega)$ respectively, are functions of the spectral frequency, ω, and are designated as complex for
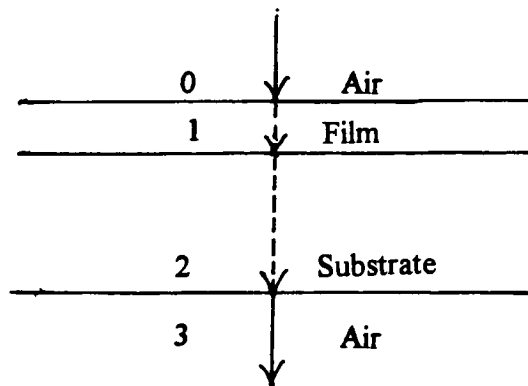
Figure 2-6 Film/Substrate Model

27

this study. If the substrate is silicon in infrared radiation, the extinction coefficient is essentially zero so the refractive index may be treated as real. If the substrate is fused silica in visible or UV radiation, the refractive index is treated as complex but the extinction coefficient, κ_2, is most significant at UV frequencies. The amplitude transmission from medium 0 through the film to medium 2 is,

$$\hat{t}_{012}(\omega) = \frac{\hat{t}_{01} \cdot \hat{t}_{12} \cdot \exp(-i\hat{\gamma}_1 d_1)}{\left[1 + \hat{r}_{01}(\omega) \cdot \hat{r}_{12}(\omega)\exp(-i2\hat{\gamma}_1 d_1)\right]} \qquad (2\text{-}57)$$

where

$$\hat{r}_{01} = \frac{1.0 - \hat{n}_1}{1.0 + \hat{n}_1}, \hat{r}_{12} = \frac{\hat{n}_1 - \hat{n}_2}{\hat{n}_1 + \hat{n}_2}, \hat{r}_{23} = \frac{\hat{n}_2 - n_3}{\hat{n}_2 + n_3} \qquad (2\text{-}58),(2\text{-}59)$$

$$\hat{t}_{01}(\omega) = \frac{2}{1.0 + \hat{n}_1}, \hat{t}_{12}(\omega) = \frac{2 \cdot \hat{n}_1}{\hat{n}_1 + \hat{n}_2}, \qquad (2\text{-}60),(2\text{-}61)$$

$$\hat{\gamma}_1 = 2\pi\omega\hat{n}_1 \qquad \text{and} \qquad \hat{n}_1 = n_1 - i\kappa_1 \qquad (2\text{-}62),(2\text{-}63)$$

The exponent terms in eq. (2-57) are complex and with eqs. (2-63) and (2-63),

$$\exp(-i2\hat{\gamma}_1 d_1) = \exp(-\alpha_1 d_1)\exp(-i4\pi\omega n_1 d_1). \qquad (2\text{-}64)$$

The absorption coefficient of the film, $\alpha_1 = 4\pi\omega\kappa_1$ comes from the real part and the imaginary part is the phase shift. The film's thickness is given by d_1. The absorption coefficient of the substrate is $\alpha_2 = 4\pi\omega\kappa_2$. It is applied to carry the transmittance from the film side of the substrate, through its thickness, d_2, to the air side of the substrate.

The transmittance at the substrate-air interface is,

$$T_{23} = \frac{4(n_2^2 + \kappa_2^2)}{(n_2 + n_3)^2 + \kappa_2^2} \qquad (2\text{-}65)$$

where the extinction coefficient of the substrate, κ_2, is negligible at visible frequencies as stated above.

The reflectance amplitude and magnitude are:

$$\hat{r}_{210} = \frac{\hat{r}_{21} + \hat{r}_{10}\exp(-i2\gamma_1 d_1)}{1.0 + \hat{r}_{21}\hat{r}_{10}\exp(-i2\gamma_1 d_1)} \qquad (2\text{-}66)$$

and

$$R_{210} = \hat{r}_{210}\hat{r}_{210}^{*} \qquad (2\text{-}67)$$

respectively.

The spectral refractive index and extinction coefficient, $n(\omega)$ and $k(\omega)$ respectively, can be extracted from the transmittance and reflectance spectra via a number of different numerical procedures. The details of the specific process used for this report is beyond its scope. Once obtained, the data can be shown to reproduce the original transmittance and reflectance spectra by applying the equations above.[28]

2.10.2 Application to the Band Structure

The absorption spectrum of a non-crystalline solid has been treated by Abe and Toyazawa as a disordered system patterned after a virtual crystal into which positional disorder has been introduced. The conduction and valence band wave functions of the amorphous material can be expanded in terms of Bloch waves of the conduction and valence bands of the virtual crystal. However, there is no mixing of valence and conduction band waves due to positional disorder.

The band structure of the virtual crystal consists of parabolic density of states in the conduction and valence bands that are separated by an energy gap of width E_g. Due to the disorder within an amorphous material, states from the conduction and valence bands extend exponentially into the gap. These "tails" at the edges of the gap have the effect of narrowing its width. A typical absorption spectrum of an amorphous or strongly disordered system consists of the three regions shown in Figure 2-7. In region I, absorption is weak due to impurities in the amorphous semiconductor, i.e. atoms of a different chemical nature, vacancies, etc.

Region II is the exponential tail of the band and absorption increases as such with photon energy. Absorption from the valence band to the tail has the form,

$$\alpha^{BT} = \alpha_{E_g} \exp\left((E - E_g)/E_o\right) \qquad (2\text{-}68)$$

where α_{E_g} is the value of α at $E = E_g$ and 5.6 eV < E < 6.06 eV. By fitting a $\ln(\alpha)$ vs. E line to region II, E_o, can be determined.

Region III comprises transitions into extended states near the optical edge, i.e. from valence to conduction band. It has an E^2 dependence given by

$$\alpha^{BB} \propto (E - E_x)^2 \qquad (2\text{-}69)$$

over the range $6.06 < E \le E_g$. The disordered band gap, E_x, can be determined from a $\alpha^{1/2}$ vs. E linear fit to region III.

The energy gap of the disordered material is modeled as,

$$E_x(W,T) = E_g - AE_o(W,T) \qquad (2\text{-}70)$$

where E_o is the inverse slope of the exponential region and dependent on the absolute temperature, T, and a measure of the disorder, W. A is the material constant and is independent of disorder and temperature.
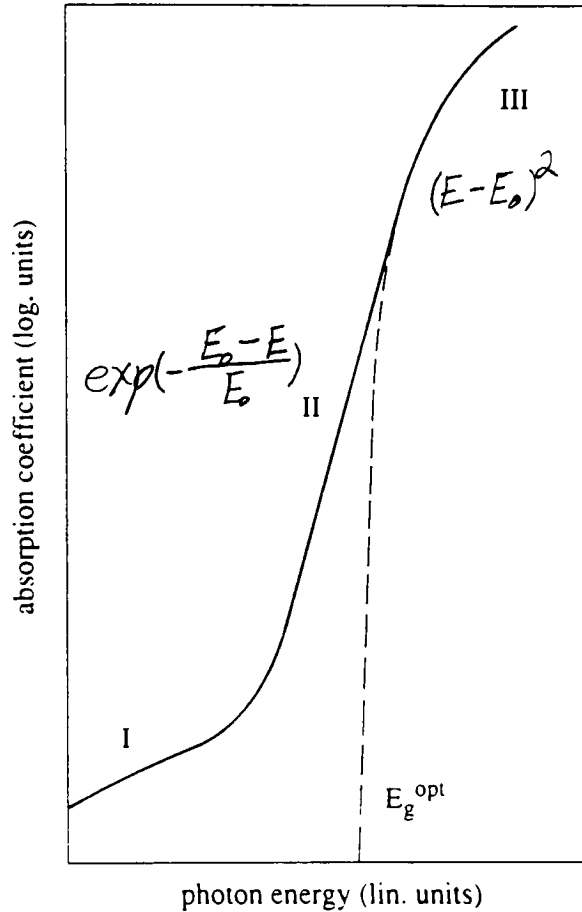
Figure 2-7 The Three Regimes of Absorption Coefficient in a Disordered Semiconductor.[29]

The degree of disorder is a function of lattice misalignment, impurities or vacancies which are manifested in E_o, the inverse slope of region II. Localized defect states within the energy gap from which an electron is excited into the conduction band, state-to-band (SB) absorption, are exhibited in the low-energy ($E \le 5.6$ eV) absorption characteristics,

region I. This is given by $\alpha^{BT} + \alpha^{SB} = \alpha$, and α^{SB} can therefore be determined by applying the appropriate values of E_o and E_g to eq. (2-68) and subtracting from α.[29,30] The defect density, N [cm^{-3}], can be estimated using the relation, $N \approx 10^{16} \cdot \alpha_{max} \cdot W_{1/2}$ where $W_{1/2}$ is the width of the peak at half maximum, and α_{max} is the peak absorption (in cm^{-1}).[31]

A measure of the relative level of disorder between two material samples is the ratio of the E_o's, since E_o is a function of the disorder. Another measure of the degree of disorder is the change in E_g between two temperature extremes,

$$\Delta E_g(T) = E_g(0) - E_g(T) \qquad (2\text{-}71)$$

the reference temperature being 0° K. This is the only measure of disorder when there is no exponential or low-energy absorption. and can be expressed in terms of Einstein's harmonic oscillator model and weighing in the effects of thermal expansion.[32]

2.11 Theoretical Approach to Infrared Optical Properties of AlN Films

As stated previously, the predominant contaminate in the deposited film is oxygen giving a 2-phase composite of alumina (Al$_2$O$_3$) and aluminum nitride (AlN). The composition of this AlON film is specified by formulas such as (AlN)$_x$(Al$_2$O$_3$)$_{1-x}$, or AlO$_x$N$_y$ but for this analysis, (AlO$_{3/2}$)$_{1-z}$(AlN)$_z$ will be used. The optical properties of this film depends on the response of both phases. As stated in a previous chapter, pure AlN crystallizes in a wurtzite structure and pure AlON crystallizes in a spinel structure and both are built on
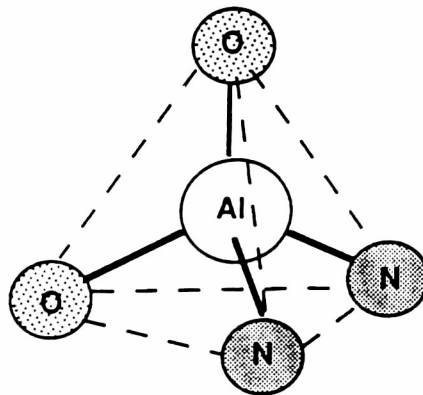
Figure 2-8 Tetrahedral unit of Aluminum nitride.[33]

Al-centered tetrahedral structures shown in Figure 2-8. The Al atom in this structure has a

coordination number of four. At 850° C, pure AlN begins to oxidize as oxygen atoms randomly occupy some of the tetrahedral apices forming phases of δ- or θ-alumina (Al_2O_3). Beyond 850° C the oxygen composition increases with time and temperature until the AlN is completely oxidized or the supply of oxygen atoms are depleted. At 1200° C and above, alumina transforms to the α phase which exhibits a coordination of 6 rather than 4.[33]

The dielectric constant of the mixture may be calculated from,

$$\varepsilon_m = \sum_j f_j \varepsilon^j \qquad (2\text{-}72)$$

where j represents one of the five different tetrahedral configurations listed in Table 2-4, f_j is the volume fraction of the jth configuration given by,

Tetrahedral Configuration	j =	ω_o cm^{-1}	Γ cm^{-1}	Ω cm^{-2}	ε_∞
AlO_4	0	660.0	400	4×10^6	5.0
AlO_3N	1	667.5	350	"	4.96
AlO_2N_2	2	675.0	300	"	4.92
$AlON_3$	3	682.5	250	"	4.88
AlN_4	4	690.0	200	4×10^6	4.84

Table 2-4 Parameters for determining ε_m.

$$f_j = \frac{V_{Al\text{-}O}^{(j)} + V_{Al\text{-}N}^{(j)}}{V_{tot}} \qquad (2\text{-}73)$$

where

$$V_{tot} = (1 - z)V_{AlO_{3/2}} + zV_{AlN} \cdot \qquad (2\text{-}74)$$

is the total volume.

Considering the case of an AlON film given as $(AlO)_{0.2}N_{0.78}$ which is equivalent to $(AlO_{3/2})_{0.146}(AlN)_{0.854}$. This gives, $V_{tot} = [(1-z)1.2 + z]V_{AlN} = 1.029V_{AlN}$ where use was made of

32

$$V_{AlO_{3/2}}/V_{AlN} = 1.2. \qquad (2\text{-}75)$$

The fraction of the total volume occupied by tetrahedral structures with two oxygen and two nitrogen atoms (j = 2), f_2, is determined with $V_{Al\text{-}o}^{(2)} = 3z^{(2)}(1\text{-}z)^{(2)}1.2V_{AlN} = 0.0556V_{AlN}$ cm^3 and $V_{Al\text{-}N}^{(2)} = 3z^{(2)}(1\text{-}z)^{(2)}V_{AlN} = 0.0466V_{AlN}$ cm^3 resulting in $f_2 = 0.1$. When this procedure is correctly applied to all tetrahedral configurations, the sum of the volume fractions is 1.0, i.e.

$$\sum_j f_j = 1 \qquad (2\text{-}76)$$

as expected.

The dielectric constant of the five different basic tetrahedral units can be represented in the spectral region by the Lorentzian oscillator,

$$\varepsilon^j = \varepsilon_\infty^j + \frac{\Omega^j}{\left(\omega_o^j\right)^2 - \omega^2 - i\omega\Gamma^j}. \qquad (2\text{-}77)$$

This is essentially the same Lorentzian oscillator introduced in eqs. (2-39) through (2-44) rewritten in a slightly different format. Here ω_o is the resonance frequency, Γ the full width at half maximum, and Ω is the oscillator strength. The dielectric constant at infinite frequency, ε_∞, appears instead of 1 because other factors in addition to electron cloud displacement affecting polarization. The values of these parameters are given in Table 2-4 along with the units.[33]

The refractive index, $n_1(\omega)$ and extinction coefficient, $k_1(\omega)$ are determined from ε_m by,

$$n_1(\omega) = \sqrt{\frac{\varepsilon_r(\omega) + \sqrt{\varepsilon_r(\omega)^2 + \varepsilon_i(\omega)^2}}{2}} \qquad (2\text{-}78)$$

and

$$k_1(\omega) = \frac{\varepsilon_i(\omega)}{2 \cdot n_1(\omega)} \qquad (2\text{-}79)$$

respectively.

Figure 2-9 shows plots of the theoretical and experimental FTIR spectra of four AlON films in different states of oxidation. The theoretical predictions closely match the experimental results in the first three cases. The last graph (d) is that of a film sample that was heated to 1200° C causing the formation of α-alumina which is made up of octahedral structures (coordination # = 6) rather than tetrahedral structures. This film does not fit the model hence the poor correlation.[33]
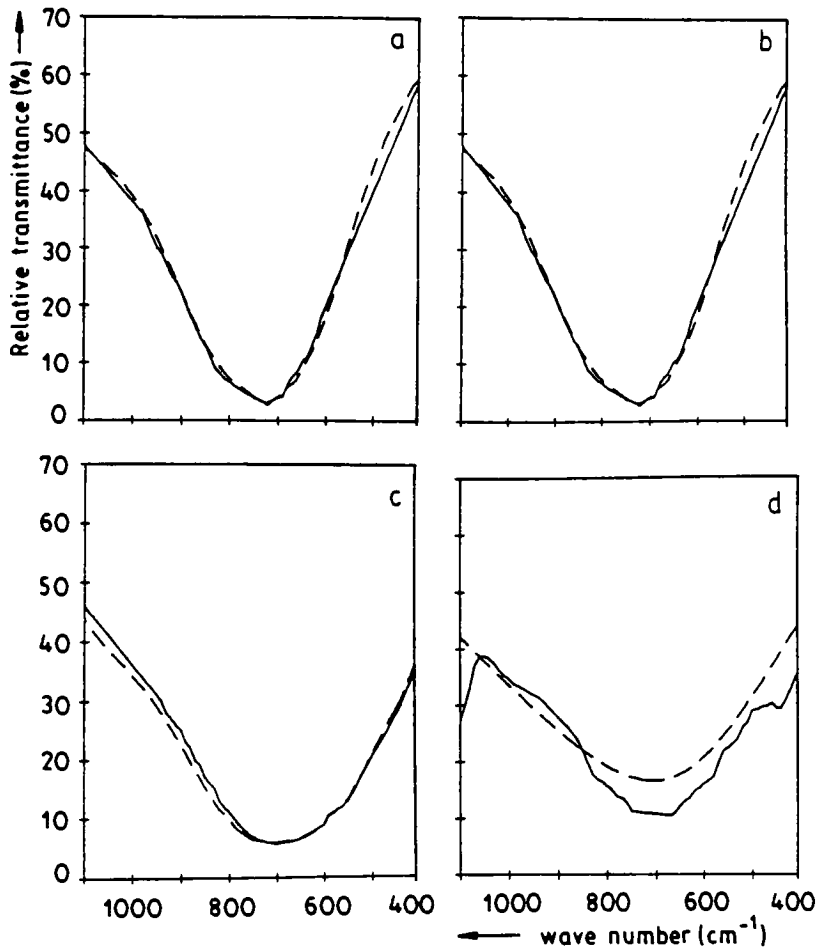
Figure 2-9 Theoretical and experimental FTIR spectra of AlON films.[33]

2.12 Morphology

The morphological structure and topography of the film samples were studied to help detect any effects of surface area change with the measured capacitance due to annealing. This analysis was done on a Digital Instruments Dimension 3000 Scanning Probe Micro-

scope using the Nanospec II controller and image analysis software. The Dimension 3000 consist of the microscope head containing laser position and adjustment controls and the piezo-tube, the image, control, and scan monitors. The Dimension 3000 has the capability of non-contact surface profiling, atomic force microscopy (AFM), using tapping mode, scanning tunneling microscopy (STM) for conductive materials. Other scan modes are the friction force mode for imaging frictional forces, force modulation mode for elasticity analysis, magnetic field and electric field analysis using magnetic force modulation (MFM) and electric force modulation (EFM) respectively.

The Nanospec II software provides analytical tools for performing roughness, auto-covariance, spectral density analysis, etc. of captured images.

2.12.1 Concepts of Atomic Force Microscopy

AFM, a derivative of scanning probe microscopy, permits microscopic surface details to be imaged by either tapping or scanning with a probe/cantilever assembly. The probe tip is chemically etched from a Si or Si_3N_4 crystal and mounted on a silicon cantilever. Silicon tips have a higher aspect ratio, the most consistent tip sharpness, and provide the best edge-imaging capability of all probe tips supplied at present. An illustration of a silicon probe is shown in Figure 2-10 and a silicon nitride probe is shown Figure 2-11. It is very important that tip morphology be understood so its effect on the image can be taken into account.[34]

The objective of SPM imaging is to keep the probe tip a constant height above the sample. Any changes in the surface in the scan direction, revealed by a signal from the height-sensing mechanism, causes a feedback control circuit to raise or lower the probe and record the new height.[34]

Many height-sensing mechanisms have been developed. A common one used with conducting samples is tunneling current sensing which is capable of angstrom-level resolution. This is possible because the tunneling current in a vacuum changes an order of magnitude for each angstrom of separation.[34]

The scheme used in this investigation was the Dimension 3000's tapping mode which is a form of mechanical resonance. The tip and cantilever are silicon. The cantilever is vibrated at its natural or resonant frequency and a change in the tip's height above the sam-

ple is detected by a change in the vibrational frequency. In order to follow the contour of the surface the resonant frequency must be >10 kHz. The natural frequency of a cantilever can be determined from its physical structure and properties.[34] The spring constant, K, of a cantilever is related to its resonance frequency by, $f = (K/9.57\rho LA)^{1/2}$ where L and A are the length and cross-sectional area of the cantilever, and ρ is the density of the cantilever material. The spring constant of the cantilever can be determined from its Young's modulus, E, and its moment of inertia, I, by $K = 3EI/L^3$.[35] The substrate of a cantilever is vibrated by a piezo stack causing the cantilever and tip to oscillate. The vertical deflection of the cantilever is altered as it passes over the surface of the sample. The cantilever's vertical position is monitored by a laser beam that is reflected off its surface. So, prior to scanning a sample, several preliminary adjustments need to be made.[34]
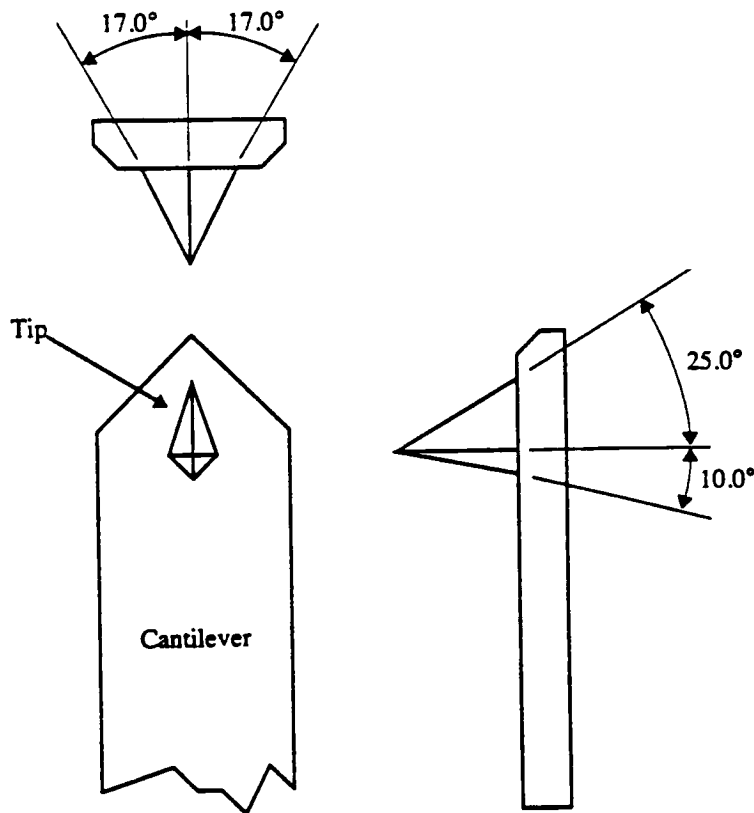
Figure 2-10 Silicon Cantilever; Theoretical Tip Shape.[34]

The laser must be positioned on the top of the freely vibrating cantilever via the laser adjustment knobs on top of the microscope head. The laser and the cantilever were displayed in the control monitor. When the laser is properly positioned on the cantilever, the sum signal (SUM), which is also shown graphically on the image monitor, will be at least 1.0. Then, the vertical deflection signal (Vert Defl) of the beam wass set to zero by adjusting the mirror adjustment knobs on the side of the microscope head so as to center the red dot on the detector graphic of the image monitor. When this is done, the laser image will also be centered on the head's filter screen.[34]

Lever Type	A	B	C	D	Spring constant (N/m)	Measured Fr (kHz)
100 μm Wide	115	122	21	60	0.58**	40
200 μm Wide	193	205	36	113	0.12**	12.3-22.1 †
100 μm Narrow	115	122	15	69	0.38**	-
200 μm Narrow	193	205	20	150	0.06**	-
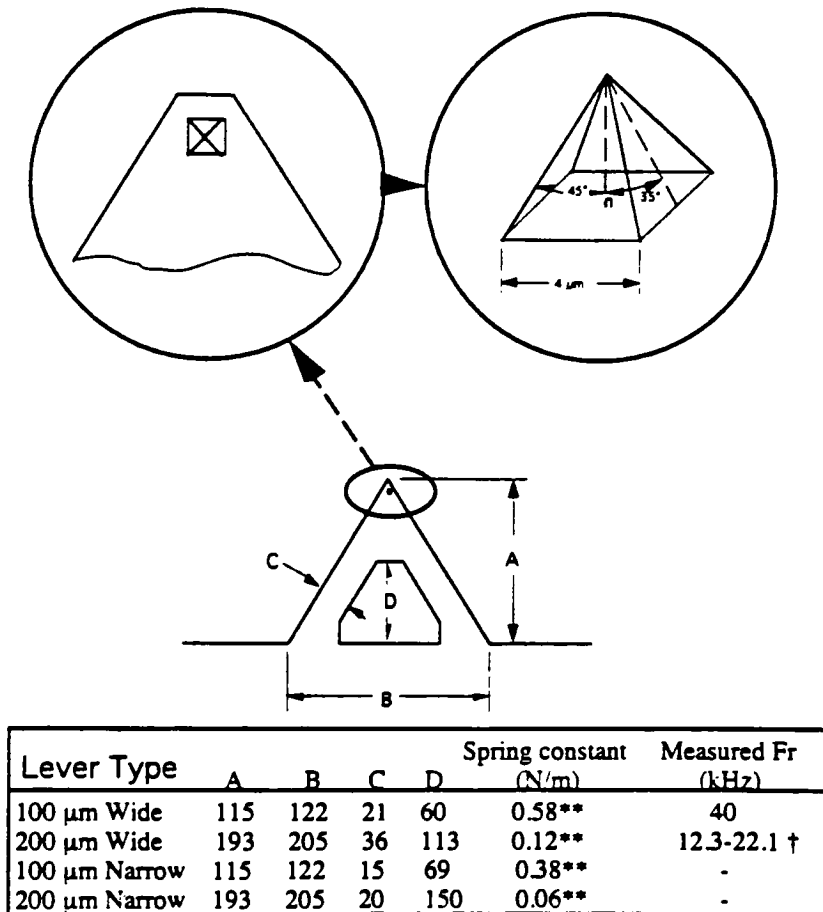
Figure 2-11 Silicon Nitride Cantilevers; Specification and Tip Shape.[34]

Next, the cantilever's resonant frequency was determined and it's drive frequency was set to 90% of the resonant frequency. The drive signal was set to give a RMS amplitude (RMS Amp) of 2-3 VRMS. The set-point was set to a value in accordance with the de-

sired response time. This parameter influences response time of the cantilever and the force applied to the sample. With a set-point slightly less than the RMS amplitude, the system takes longer to respond to a height change and also very little energy is transferred to the sample. When the set-point is significantly below the free vibration amplitude, the system recovers quickly from a change in sample height but more energy is transferred to the sample. So, where the scan area involved a step, the set-point was set lower than when the scan area was visually smooth in order to minimize distortion.[34]

2.12.2 Preparing to Scan

Several other parameters were entered into the Main Controls, menu to Figure 2-12, properly setup the AFM for imaging. Two are the proportional and integral gain which determine how well the feedback circuit tracks the sample surface. The recommended settings are just short of where the piezo begins to oscillate. These were chosen to be 0.5 for integral gain and 1.7 for proportional gain.

Main Controls Settings

```
Motor  View  Frame  Capture  Microscope  Lithography  Off-line  Quit
========================== Main Controls ==========================

Main Scan Controls              Main Feedback Controls
Scan size [μm]       :   90.0   Integral gain         :    0.500
X offset [nm]        :   0.00   Proportional gain     :     1.20
Y offset [nm]        :   0.00   Setpoint [V]          :     2.00
Scan angle [deg]     :   0.00   Drive frequency [KHz]     337.88
Scan rate [Hz]       :    1.5   Drive amplitude [mV] :      225
Number of samples    :    256   Analog 2 [mV]        :     0.00
Slow scan axis       : Enabled
Z limit [V]          :    440

Main Controls    Other Controls    Interleave Controls

First Image                     Second Image
Data type            : Height   Data type         :   Height
Z range [nm]         : 300.00   Z range [nm]      :      300
Line direction       : Trace◄   Line direction    :   Trace◄
Scan line                Main   Scan line
First and Second...            Third Image

                        Opt: -2714.6 μm   SPM: -12380.1 μm
Equip: D 3000 AFM  Tip: Secured  Capture: Off   File: Date/Time
```

Figure 2-12 The Main Control Panel showing Tapping Mode settings.[34]

The Scan Size refers to the size of the square area (X and Y directions) that will be scanned by the probe. The Number of Samples, the number of pixels that make up the im-

age (128, 256, or 512), was set to 256. The X direction runs along the cantilever and the Y direction is perpendicular to the cantilever.

The scan rate is the left-right rate (in hertz) at which the probe sweeps the sample. The scan rate, typically 1.0 - 2.0 Hz, should be decreased as the scan size increases. A slow scan rate also allows quicker system response to steps than a faster scan rate.

In the lower part of the Main Controls menu, the First Image field was cleared, and Second Image was turned off. The Data Type parameter was set to "Height" which means that the Z piezo will change position only to keep the rms amplitude constant (the "Set-point"). The set-point represents a predefined height above the sample, so the probe was raised or lowered as necessary to maintain that height.

The Z range, the maximum surface feature height (in nm) that is to be displayed, was set to 100 nm. Also, the user specifies the left scan as the trace or retrace direction.[34]

2.12.3 Scanning the Sample

The sample was moved under the microscope by selecting the Load New Sample option under the Stage menu. This option allowed the user to bring the surface of the sample into focus and find the area to be scanned. Then, the Engage command was selected from the Motor menu and the Nanospec moved the tip to the surface and started the scan.

After the image scan started, the Scope Mode was activated to view the probe trace and retrace signals. This is a graph of the probe height versus X position that shows the surface contour in the trace and retrace direction. If they are not nearly identical, the scan rate, set-point, integral or proportional gain was adjusted to give the optimal image.

When the probe response is acceptable, image capture was activated by selecting that option from the Capture menu.

After the capture was complete, the system was taken off-line for image processing. In most instances, a view of the surface plot showed ripples in the image which were caused by drifting of the Z piezo. The image was flattened by the Auto Flatten option from the Modify menu to remove these irregularities. This action resulted in the average Z level being zero.

Next, The image was cross-sectioned in the Section program from the Analyze menu to display a height profile of the sample along a user drawn line. This utility also provided FFT information along the line.

The Roughness utility was used to perform a surface analysis, peak count, surface area, and summit count, etc. from a user selected area. Each parameter was measured relative to a user selectable threshold value. The threshold is in turn based on the zero or the tallest peak in the selected area. The reported surface area was the 3-dimensional area of that part of the image above the threshold. It is computed by summing the area of all triangles formed by three adjacent data points. The number of summits is the number of peaks that are greater than its eight nearest neighbors by at least the threshold value.

In addition to the zero plane, the routine also calculates a Mean Plane which is the image plane about which the variance of the Z values is a minimum. The Center Plane is the plane which is parallel to the Mean Plane for which the volume enclosed by the surface area is the same above and below the plane.

The routine also reported the Z range which is the difference between the highest and lowest points within the selected area. The Max. Height is the difference in the highest and lowest points within the selected area relative to the Mean Plane. The Mean Z value is the average of all Z values within the chosen area and is very close to zero if the image has been flattened. The Rms Z value is the standard deviation of all Z values relative to the average Z value.

The Mean Roughness, R_a, is the mean value of the surface, $f(x,y)$, relative to the Center Plane and is calculated by,

$$\frac{1}{L_x L_y} \int_0^{L_x} |f(x,y)|\, dx \int_0^{L_y} dy \tag{2-80}$$

where L_x and L_y and the dimensions of the selected area and $f(x,y)$ is the surface.

The surface area difference is the ratio of the 3-dimensional area to the projected area produced by projecting the surface onto the threshold plane. It is calculated from, [34]

$$\text{Surface area difference} = \left[\frac{\text{surface area}}{\text{projected area}} - 1.0 \right] * 100 \,. \tag{2-81}$$

40

2.13 Analytical Instruments

The thickness and refractive index of the film samples were measured using an ellipsometer. Optical spectra of film samples on fused silica over the UV/Visible band were obtained from the Perkin-Elmer Lambda 11. Infrared spectra of film samples on silicon wafers were obtained from the Perkin-Elmer 1770 Fourier Transform Infrared (FTIR) spectrometer.

The film composition was determined qualitatively by Auger Electron Spectroscopy (AES) and Secondary Ion Mass Spectroscopy (SIMS).

2.13.1 The Ellipsometer

A manual ellipsometer was used to measure the thickness and index of refraction. The difference in the angle that a polarized light source (632.8 nm) makes with the plane of incidence between incidence and reflection were manually read from the ellipsometer. This information was typed into a file along with the refractive index and extinction coefficient of the substrate, silicon. The file was then read by a FORTRAN algorithm which calculated the thickness and refractive index of the film.

2.13.2 UV - Vis Spectroscopy

The Lambda 11 is a single beam spectrometer intended for routine UV/Vis measurements. There are two lamps that provide the radiation. A deuterium lamp spans the 326 to 190 nm wave length range and a halogen lamp spans the 900 to 326 nm range. The instrument has a fixed spectral bandwidth of 2 nm. Operating parameters may be entered via the keyboard or IBM PC controller. A PC controller was used for collecting these spectra. It allowed the user to enter the spectral range, the scan rate, the function (Transmittance or Reflectance), and the file name.

Prior to starting a scan, the instrument was calibrated (Autozero). For transmittance, the sample holder was emptied, and the Autozero function was selected at the terminal. This sets the 100% transmittance and 0% absorption reference levels for each wave length mark.

For reflectance, a pre-calibrated aluminum-plated mirror was used as the calibration standard. During reflectance calibration, the standard was mounted in a special sample holder made for reflectance measurements. This established the 100% reflectance level,

but each point of the resultant spectrum had to be corrected by the calibration factor provided with the standard.

A schematic of the system's optical elements is shown in Figure 2-13. Mirror M1 reflects radiation from the halogen lamp toward mirror M2. When the deuterium lamp is in use, mirror M1 is rotated out of the optical path. After leaving the mirror M2, radiation passes through a filter and a slit before being reflected off a monochromator grating. The monochromator is a holographic concave grating with 1053 lines/mm at the center. The filter is driven in synchronization with the monochromator so that the radiation is prefiltered before it reaches the monochromator. Upon leaving the monochromator, the radiation passes through a slit, gets reflected off mirrors M3 and M4 and is then incident on the sample. The radiation passing through the sample is then collected by a lens and measured at the detector.[36]
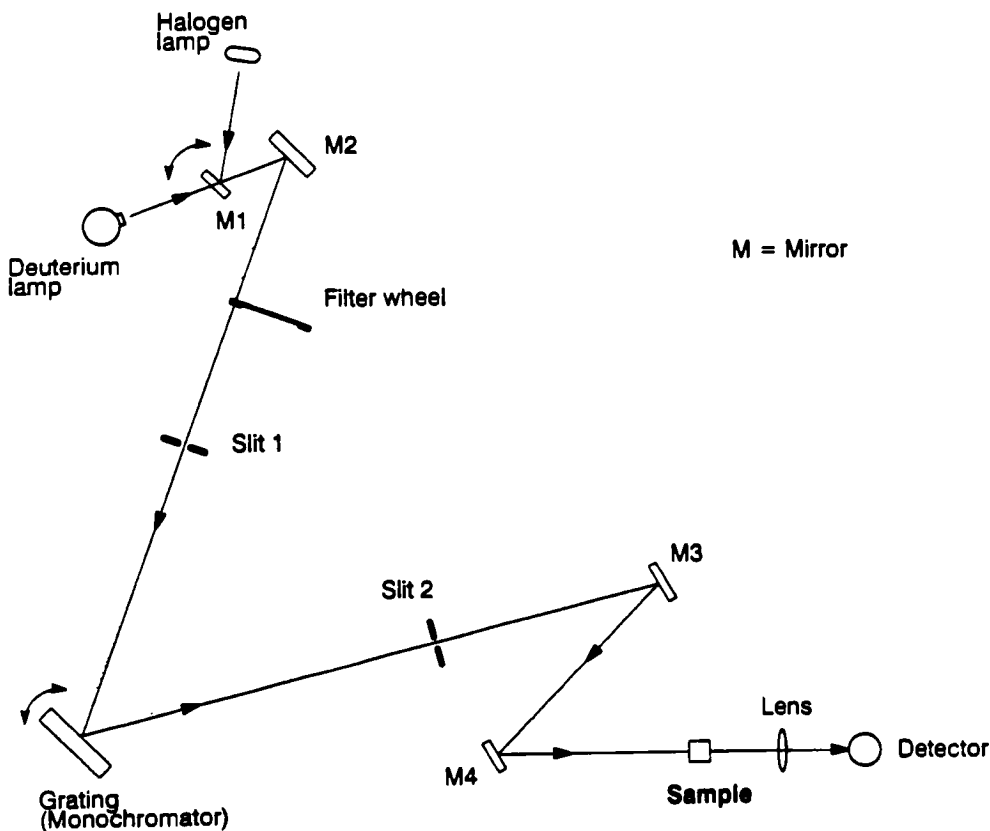
Figure 2-13 Optical Path of the Lambda 11.[36]

2.13.3 Infrared spectroscopy

The P-E 1770 infrared spectrometer is a single beam Michelson interferometer with frictionless electromagnetic drive and bi-directional data collection.

2.13.3.1 Features of Interference Spectroscopy

The interferometer approach has several advantages over traditional dispersive instrumentation. First of all, there are no filters or gratings in an interferometer to cause discontinuities in the spectrum. Also, all frequencies are measured simultaneously whereas with a dispersive instrument, they are measured successively. A complete spectrum can be obtained very rapidly and many scans can be averaged in the time required for a single scan of a dispersive spectrometer.

An interferometer will give at least the same energy throughput as a dispersive spectrometer at the same resolution. The resolution of an interferometer is constant throughout its frequency range. In a dispersive instrument, slits are used for resolution control and to restrict stray light, but also restrict energy throughput. The effects of stray light in interferometers is so low that a direct equivalent in dispersive instruments is non-existent. Because of this and the advantage in the last paragraph, interference spectrometers can achieve the same signal-to-noise ratio in less time.

The frequency scale of an interferometer is more accurate and stable than that of a dispersive instrument because it is derived from a helium-neon laser. The frequency of this laser has been determined very accurately and is known to be very stable and in part accounts for the constant resolution of an interferometer over its frequency range.[37]

2.13.3.2 Theory of Interference Spectroscopy

The interference spectrum (interferogram) is the result of infrared frequencies being modulated through a Michelson interferometer diagrammed in Figure 2-14. An interference pattern is produced by a pair of interacting beams of radiation; one ray is displaced by a fraction of wave length. The amount of displacement is called the optical path difference, and the interferometer alters the difference by precisely moving one of the mirrors in Figure 2-14. The position of the other mirror and the beam splitter is highly critical because the path length must be determined exactly. Half the source beam is transmitted through the beam-splitter and the other half is reflected at a right angle toward the other

mirror. There are two optical paths. One is from the source through the beam-splitter to the movable mirror and back to the reflecting surface of the beam-splitter, L_1. The other is
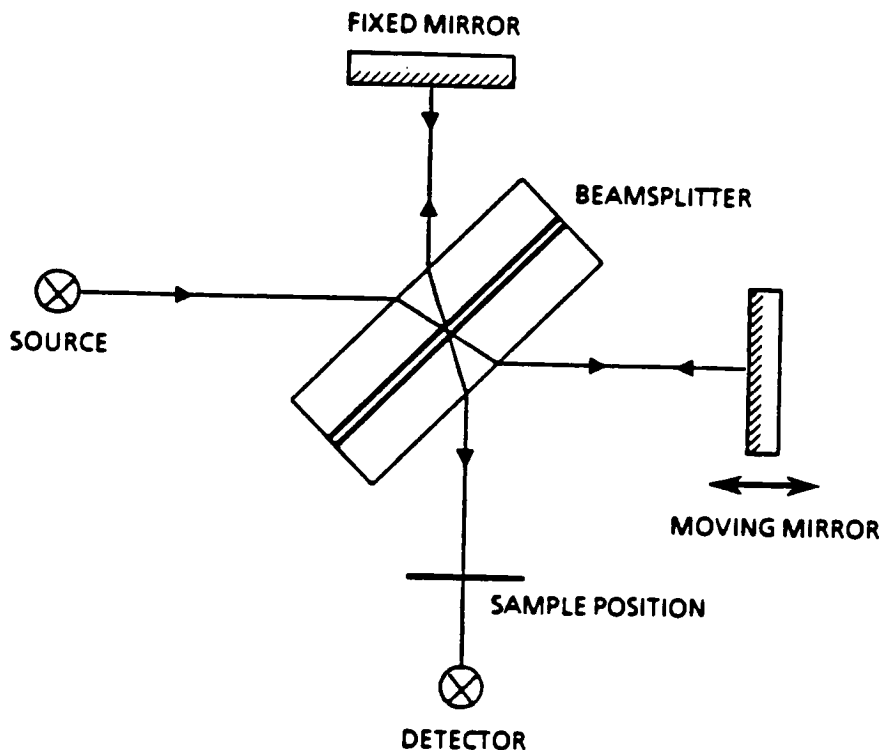
Figure 2-14 Diagram of a Michelson Interferometer.[37]

from the source to the other mirror via reflection off the beam-splitter and back to the reflecting surface of the beam-splitter. The two rays form an interference pattern at the reflecting surface of the beam splitter. For a single wavelength, the interference pattern as a function of path length is a sinusoid of the same wavelength. For a broad band source, the interference pattern is the sum of the magnitudes of each constituent frequency of the source. The resultant interferogram consists of a strong signal near zero path difference and then falls off rapidly. A typical interferogram is shown in Figure 2-15. An energy vs. frequency spectrum is obtained by Fourier transforming the interferogram.[37]

The transmittance of a film sample was obtained by first getting a background spectrum of the substrate, the silicon wafer. Next, the spectrum of the film on that same substrate was obtained and the two spectra are ratioed.

O OPTICAL PATH DIFFERENCE
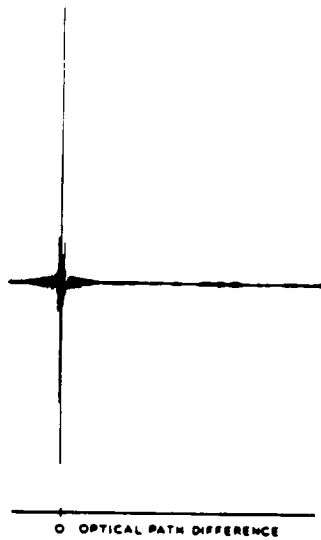
Figure 2-15 A typical FTIR Interference Pattern.[37]

2.13.4 Secondary Ion Mass Spectroscopy (SIMS)

This is a very sensitive semi-quantitative surface analysis method. It has depth profile capability with a depth resolution of ~20 Å and can be used to study interfaces and implant layers.

A mono-energetic ion beam, usually Ar^+, about 2 mm in diameter is incident on the specimen causing positive, negative, and neutral ion fragments to be ejected from the surface at low kinetic energy. These secondary ion fragments are emitted with an approximately cosine distribution and are collected by any number of proprietary schemes and directed into the aperture of the electrostatic energy analyzer. The electrostatic energy analyzer admits only ions of a narrow energy range which then pass through a mass spectrometer. From there, on ions of a given mass/charge ratio pass through to the detector where they are counted. The magnitude of the detector signal for a particular mass/charge ratio is proportional to the number of those ions counted. Because most atoms take on multiple oxidation states and form complex ionic radicals with other atoms, the mass/charge ratio may bear a complex relationship to the original material composition.[38]

The specimen is brought under vacuum, ideally 10^{-8} to 10^{-9} Torr, at the time the sample surface is being bombarded. Data collection requires about 5 minutes and the probe beam can be stationary or rastered across the specimen.[38]

2.13.5 Auger Electron Spectroscopy

With this form of analysis the sample is under much lower vacuum which may require an overnight pump-down period. The probe source is a mono-energetic beam of electrons ~100 mm in diameter and reaches the top 10 atomic layers with Å depth resolution. It is useful for contamination, implant, and interface analysis.

The probe beam ejects a core (K) level electron from a surface atom. This vacancy is filled by the de-excitation of an electron from the L level. The de-excitation is accompanied by a photon which ejects another L level electron with an amount of energy characteristic of the parent atom. If the atom is within the first 10 atom layers, the electron will very likely escape the surface without energy loss (e.g. scattering). This is the Auger electron, and is detected by a cylindrical mirror analyzer. The Auger electrons are less numerous than the ejected core electrons, so the signal must be differentiated to enhance there presence. Any atom can be identified by its specific set of energy peaks. The magnitude of a peak is proportional to the relative amount of that atom present in the material.[39]

2.13.6 X-ray Diffractometry (XRD)

An x-ray diffraction spectra of the film samples was taken to detect any long range crystallinity. The instrument used was the Rigaku Geigerflex which used a Cu kα radiation (λ = 1.54056Å) and has a maximum scan range of 2θ = 20° - 160° The user selects the starting and ending scan angle, the slew rate, (0.06 - 6.0 deg/min), and step size (0.01°-0.1°). Another software package, JADE, automatically locates peaks by their angular position and planar spacing, and allows multiple spectra to be over-layed for comparison.

The peak positions of the spectra of a material are a function of the crystal structure and planar spacing. The spacing of planes in the direct lattice are proportional to the position vector in reciprocal space. The position vector in reciprocal space is defined so it is normal to planes (h k l) in the direct lattice. Planes in reciprocal space, (h' k' l'), are proportional to those of the direct lattice, e.g. h'/h = k'/k = l'/l = N. The position, θ_b, of a peak corresponding to (h k l) planes of spacing, d_{hkl}, satisfies the Bragg relation,

$$N\lambda = 2d_{hkl} \sin \theta_b \qquad (2\text{-}82)$$

where N is an integer representing the order.[40]

The intensity of a peak is a function of the crystal structure and atoms forming the respective plane. For a given plane in the reciprocal lattice, (h' k' l'), the intensity of the respective peak is proportional to

$$F(h', k', l') = \sum_j f_j e^{i2\pi(h'x_j + k'y_j + l'z_j)}$$
(2-83)

where the sum taken is over the j atoms in the unit cell located at (x_j, y_j, z_j) and f_j is the scattering factor of the jth atom in the cell. Scattering factors are tabulated for every known atom in physics data books.[41] The five most intensive planes of pure AlN[42] are listed in Table 2-5 along with the spacing.

Plane	Spacing, Å	2θ	rel. intens.
(002)	2.489	36.12°	21.15
(110)	1.556	59.47°	20.280
(103)	1.413	66.19°	14.89
(112)	1.319	71.46°	14.57
(100)	2.694	33.24°	13.94

Table 2-5 The five most intense AlN planes.

3 Results

3.1 Selection of sputter Parameters

The thickness and index of refraction of the film samples deposited in the trial runs are summarized in Table 3-1 and plotted in Figure 3-1 and Figure 3-2. Each point represents the mean of six ellipsometer measurements on a film sample deposited under the indicated $Ar:N_2$ gas ratio. The other sputter parameters are given in Table 2-2.

$Ar:N_2$ ratio	Mean Thickness (nm)	Mean NR
1:1	107.0 ± 5.5	2.05 ± 0.05
1:2	119.4 ± 4.3	2.05 ± 0.02
1:3	115.7 ± 8.0	2.06 ± 0.07

Table 3-1 Summary of Film Deposited in Different Ar/N_2 Environments.

The rate of film growth and hence its ultimate thickness is dependent on factors such as the sputtering rate, sputtering pressure, power, substrate temperature, and in the case of reactive sputtering, the fraction of argon gas in the mixture. It was expected that the sputter rate will be proportional to the Ar gas composition. With a higher Ar content, more Ar+ ions are generated to bombard the target. The deposition rate will depend on the amount of sputter material that can reach the substrate through the plasma. As the N_2 composition of the gas increases (Ar composition decreases), the film thickness in general may decrease due to the reduced sputter rate.

Mean Film Thickness vs. N$_2$ Composition
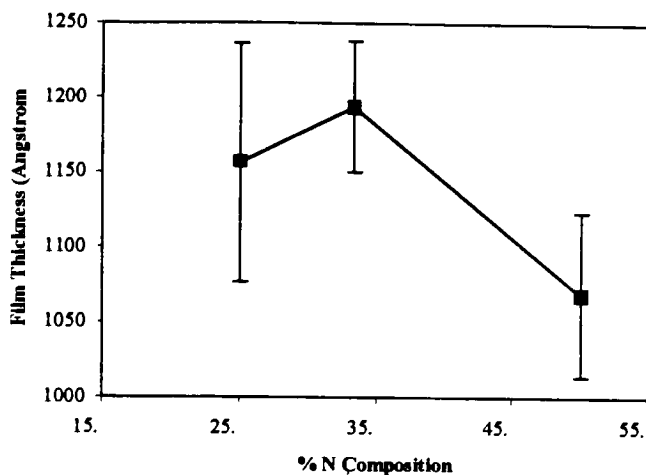
Figure 3-1 Plot of Film Thickness vs. N$_2$ Composition.

Film Index of Refraction vs. N$_2$ Composition
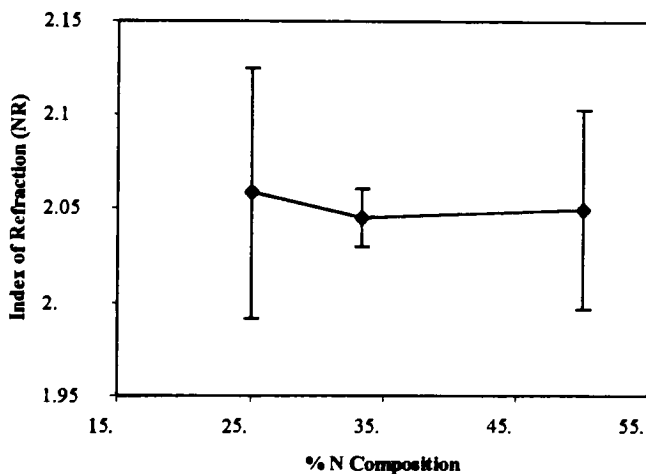
Figure 3-2 Plot of Refractive Index vs. N$_2$ Composition.

The reactivity between Al and N atoms is higher at a high N$_2$ gas composition than at a lower N$_2$ composition because of a higher probability of interaction between sputtered Al and N$_2$ molecules. So, as the amount of N$_2$ in the gas mixture increases, the N$_2$ content of the film is expected to increase also. It was also expected that within the gas composition range, a point of maximum reactivity between Al and N would be reached where the

film thickness changes significantly owing to a change in some physical property such as density. If such a point does exist within the gas composition range, a parabolic trend between film thickness and N_2 composition of the gas will result.

Plots of the Mean Film Thickness vs. N_2 composition and mean NR vs. N_2 composition show error bars that are proportional to the 1st standard deviation of the dependent parameter. Although the mean film thickness appears to be a parabolic function of N_2 composition suggesting more reactive product at an Ar:N_2 gas ratio of 2:1, the error bars are too wide to conclude such a trend. Similarly, the magnitude of error in the index of refraction prevents satisfactory determination of a trend which appears to be constant over the range of Ar/N_2 mixtures plotted. It is safe to conclude that sputtering with the parameters in Table 2-2 and Ar:N_2 of 1:1 will produce an AlN film of thickness 1000 - 1200 Å and NR of 2.0 - 2.1 on the CVC 601 sputterer. This was the intended target.

3.2 Film Thickness Measurement

Film thickness was estimated using an ellipsometer (@ λ = 632.8 nm). To verify the film thickness observed by ellipsometry, a method using Secondary Ion Mass Spectroscopy (SIMS) was employed. The films were etched using the SIMS argon ion gun while monitoring the atomic concentration of Si ions. When Si^{+4} ion concentration started to increase suddenly, the film-substrate interface was reached and etching was stopped. The samples were then taken out and the depth of the crater formed by Ar+ etching was measured by a Dektak 3ST surface profiler. This film thickness was compared with that measured by ellipsometry. The film thicknesses of two samples by both methods agreed within ± 50Å. Therefore, it was concluded that ellipsometry was an acceptable method to measure the thickness of all the films. The depth profile plots of both films are shown in Figs. 2 & 3 of the appendix.

For compositional analysis, Auger Electron Spectroscopy (AES) was used. Spectrograms of the 760, 800, 850 °C films as received and after 1 min. of sputtering are shown in Figs. 4 - 6 of the appendix. The AES Survey Scan shows the presence of Al, N, O, C and Si on the surface. Carbon is a common surface impurity in thin films whereas oxygen is present throughout all the films. The AES system would have automatically calculated the relative composition from the counts but time did not permit the sensitivities to be cali-

brated for this analysis. So, the compositional data shown with the spectra do not indicate actual film composition, but it can be concluded that the Al, O, and N composition of the three film are essentially constant.

3.3 Results of Annealing on Thickness and Refractive Index

Six sets of ellipsometer measurements were taken from each film before and after annealing. The mean and standard deviation of thickness of all films were calculated before and after annealing. The pre- and post-anneal thickness of all films are plotted simultaneously in Figure 3-3 for comparison. The refractive index was treated similarly, the pre- and post-anneal refractive index of the films are plotted simultaneously in Figure 3-4 for comparison.

Pre- & Post-Anneal Thickness
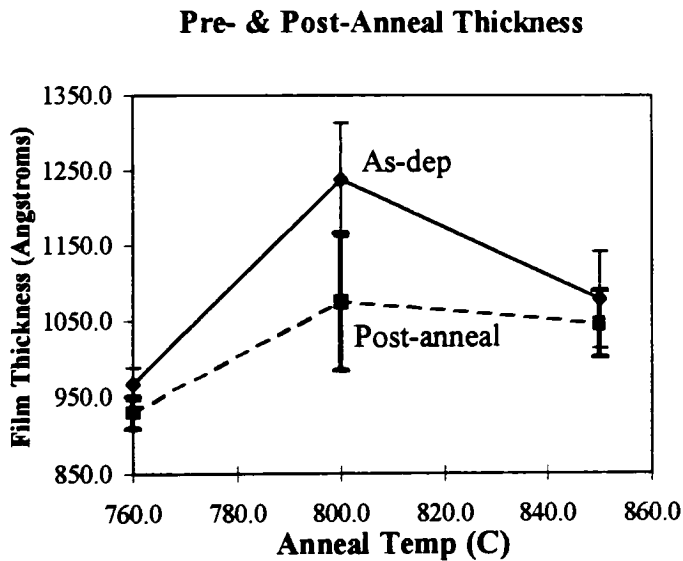
Figure 3-3 Affect of annealing on thickness.

Pre- & Post- Anneal Refractive Index (NR)
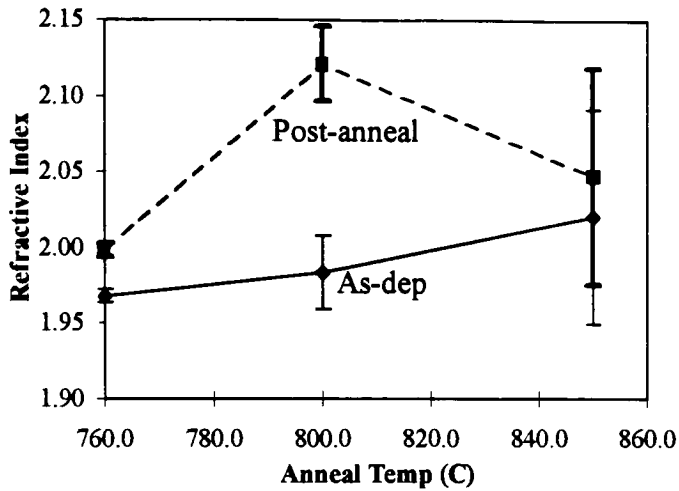
Figure 3-4 Affect of annealing on refractive index.

3.4 Capacitance and Dielectric Constant

Plots of the capacitance vs. plate area are shown in Figure 3-5 for each film type. The slope of each line, determined from a least squares fit, is proportional to the dielectric constant of the film. The dielectric constants calculated from these slopes are given in Table 3-2.
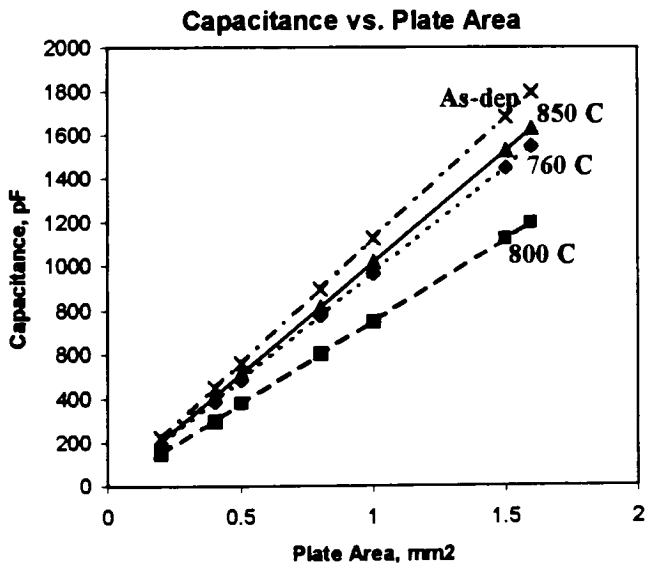
Figure 3-5 Capacitance as a function of plate area.

Film	Mean Dielectric Constant
As-deposited	11.8
760° C	10.2
800° C	9.1
850 °C	10.7

Table 3-2 Mean dielectric constant of annealed films.

A summary of the range of breakdown potential for each film type is given in Table 3-3. All capacitors on the as-deposited dielectric were shorted while approximately half the capacitors on other wafers were shorted. Those that were not broken down exhibited breakdown over a wide potential range and showed no leakage characteristics.

	Dielectric Breakdown, MV/cm			
	1.5 mm^2		0.4 mm^2	
	Low	High	Low	High
As-deposited	----	----	----	----
760 C	0.17	0.48	0.16	1.08
800 C	0.15	2.49	0.11	3.24
850 C	0.22	0.95	0.3	1.08

Table 3-3   Dielectric Breakdown potentials of the films.

3.5 Optical Effects

Plots of the extinction coefficient and the refractive index of the annealed film are shown in Figure 3-6 - Figure 3-8. Those of the as-deposited film are shown in Figure 3-9.

An analysis of the transmittance and reflectance of the film samples on fused silica began by determining extracting n and κ of each film sample on fused silica. A third party software utility was used for this task. It accepted the transmittance, reflectance and thickness of the film as input. The substrate thickness, reflectance and absorption coefficient were also provided for the utility to compute n and κ. Acceptance of the resultant spectra was based on the calculated refractive index corroborating with that measured by the ellipsometer at 632.8 nm (1.96 eV). Film thickness was the only parameter that could be adjusted to achieve a suitable refractive index and the final thickness that produced it was not far from that measured by the ellipsometer. For the annealed film samples, it was fairly straightforward to obtain n and κ spectra which yielded transmittance spectra nearly coincident with those of the experimental transmittances.

The as-deposited films presented additional difficulty and their calculated transmittances were poorer fits to the respective experimental spectra. The extinction coefficient spectra nevertheless was quite useful for the forthcoming analysis. Plots of theoretical transmittance of each annealed film is compared to its experimental counterpart in Figure 6-3 - Figure 6-5 of the appendix.

Three as-deposited extinction coefficient spectra were averaged and the absorption coefficient generated from this mean κ became the as-deposited standard. The absorption coefficient of the annealed samples and the as-deposited standard are shown simultaneously in Figure 3-10.

n and k of Film Annealed at 760 C
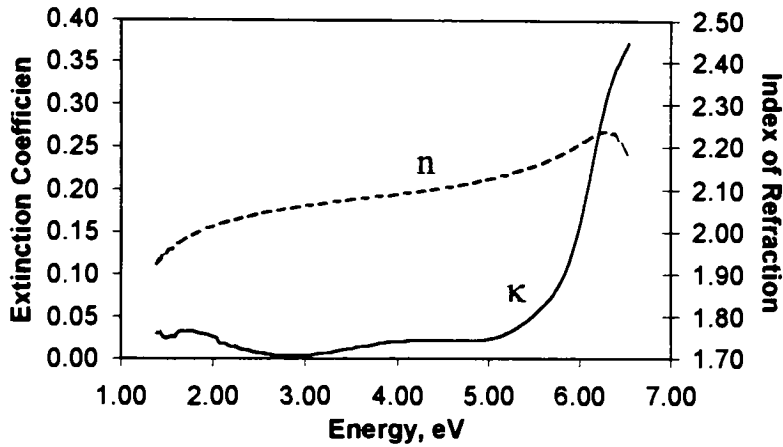
Figure 3-6 Optical Properties at 760° C.

n & k of Film Annealed at 800 C
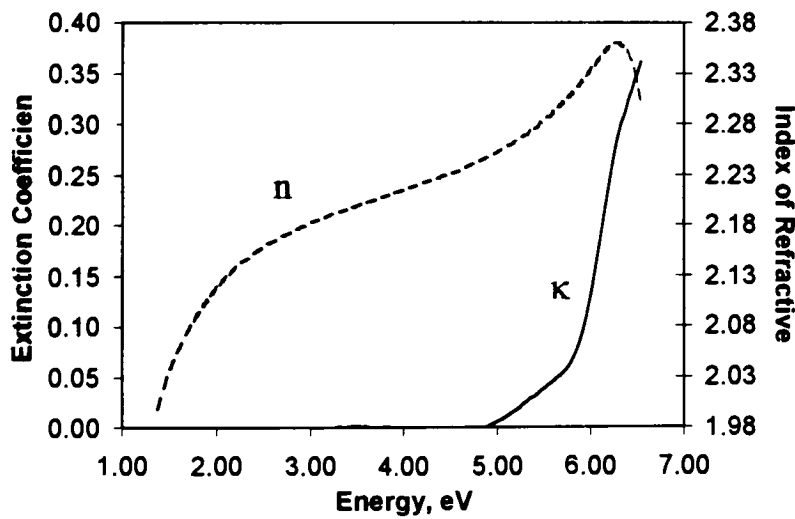
Figure 3-7 Optical Properties at 800° C.

n and k of Film Annealed at 850 C
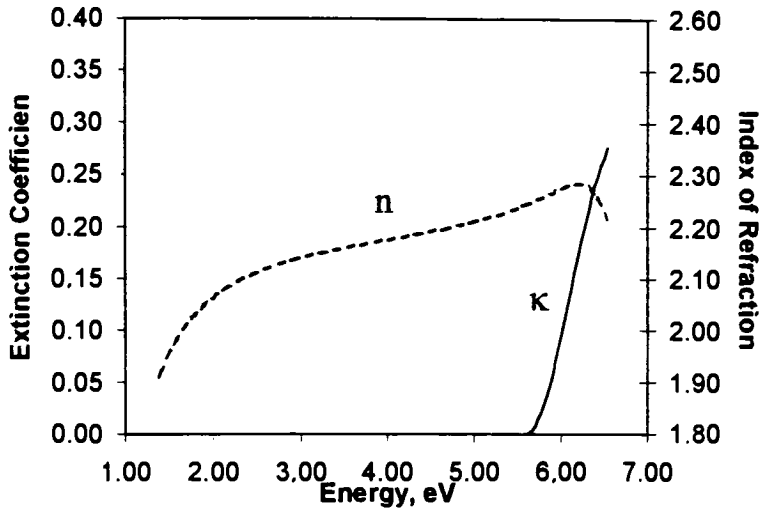
Figure 3-8 Optical Properties at 850° C.

As-Deposited Extinction Coefficient
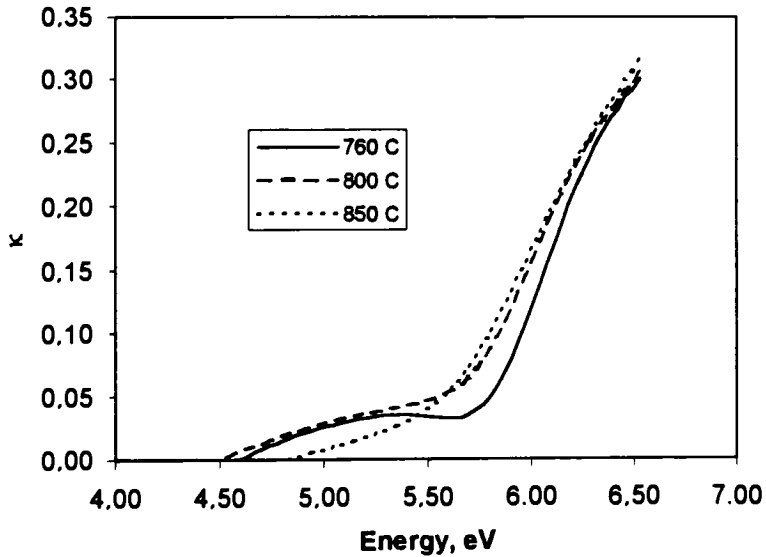
Figure 3-9 As-deposited Optical Parameter.

Ln Absorption Coefficient
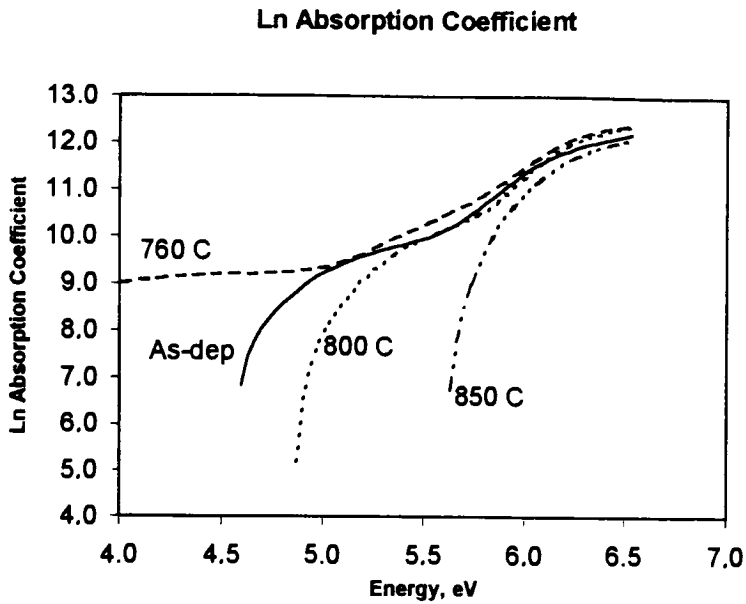
Figure 3-10 Absorption Coefficient of Annealed Films.

3.5.1 Analysis of the Curves

The absorption coefficient spectra of the annealed film were modeled after the disordered system described in section 2.10.2. After fitting points on the linear part of a curve, region II, to an exponential and the parabolic part, region III, to a quadratic function, the energy-band gap parameters were calculated. The results are shown in Table 3-4.

Film Sample	E_o (eV)	E_x (eV)	A	α_{Eg} (cm^{-1})
As-Dep (avg.)	0.294	5.13	3.57	1.61×10^5
760° C	0.34	5.20	2.88	1.61×10^5
800° C	0.261	5.39	3.03	1.61×10^5
850° C	N/A	5.35	N/A	N/A

Table 3-4 Summary of Band-gap Energy Parameters.

3.6 Absorption and Polarization

Plots of the polarization (ε_1) and absorption (ε_2) of the annealed films are shown in Figure 3-11 - Figure 3-12.

ε₁ of Annealed Films
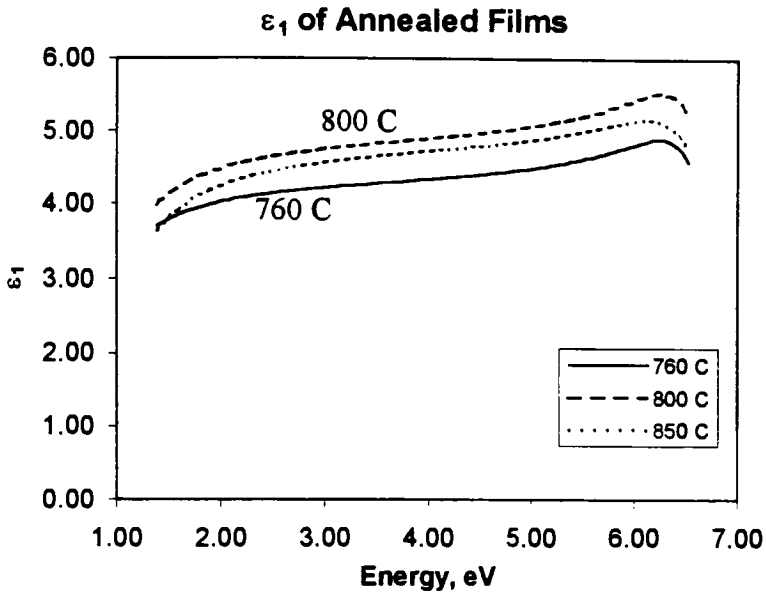
Figure 3-11 Real Part of the Dielectric Constant.

ε₂ for Annealed Films
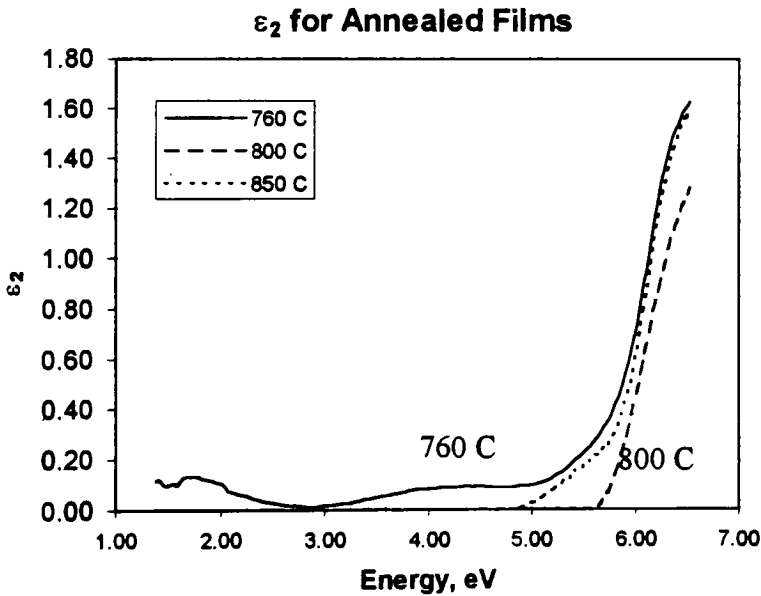
Figure 3-12 Imaginary Part of Dielectric Constant.

The state-to-band absorption, α^{SB}, can be determine by applying the appropriate values of E_o and E_g to (2-68) and subtracting from α. This does not apply to the 850° C film

which has lost much of its disorder as indicated by the absence of an linear and low energy region. Plots of the low energy absorption coefficient of the other films are shown in Figure 3-13. It is obvious the distribution is a parabolic function of energy as stated in section 2.10.2, i.e. $\alpha^{SB} \propto E^2$

State-to-Band (SB) Absorption
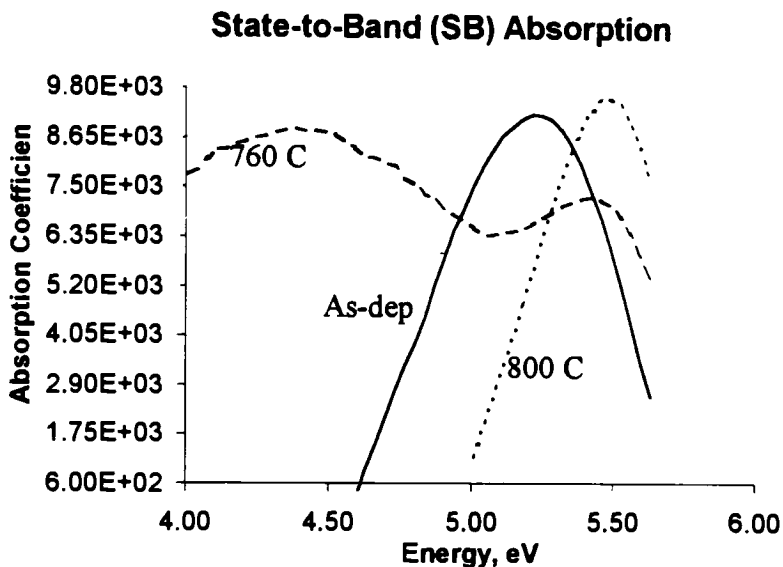
Figure 3-13 Low energy absorption characteristics.

The defect concentration (per unit volume) of each film is a function of the maximum absorption, α_{max}, and the width at half maximum, $W_{1/2}$, of its absorption curve. A summary of the defect densities calculated as described in section 2.10.2 is given in the following table. The defect concentration will be analyzed more thoroughly in the conclusions.

Film	E_{max} (eV)	α_{max} (cm^{-1})	$W_{1/2}$ (eV)	N (cm^{-3})
As-dep	5.2	9,205.0	1.2	$1.1 \cdot 10^{20}$
760° C	4.5	7,274.0	4.7	$3.4 \cdot 10^{20}$
800° C	5.5	9,570.0	1.0	$9.1 \cdot 10^{19}$

Table 3-5 Defect density summary.

3.7 Morphological Analysis

A summary of the roughness analysis of film samples on silicon wafers and fused silica are provided in Table 3-6 for comparison. The data in the table represents typical values of at least two different scans of 1 μm^2 areas. Parameter definitions can be found in section 2.12.3. The reference point for these measurements was a threshold of 2 nm. Illustrations of AFM scans of each film's surface are shown in Figs. 7 - 10 of the appendix.

The films that were annealed at 760° C on silicon wafers and quartz exhibited a significantly lower Rms Z, mean roughness, and peak count than the as-deposited film. The average peak height will not always parallel the other parameters. It is not significant that the mean

Film	RMS z (nm)		Mean Rough (nm)		Peak Ct		Avg. Pk Ht (nm)	
	Si	Silica	Si	Silica	Si	Silica	Si	Silica
As-deposited	0.59	0.71	0.47	0.56	31.0	28.0	2.24	2.31
760 C	0.44	0.49	0.33	0.39	13.0	2.0	2.23	2.06
800 C	0.7	0.71	0.49	0.57	33.0	31.0	2.37	2.35
850 C	1.54	0.88	1.1	0.69	214.0	96.0	3.77	2.49

Table 3-6 Summary of morphological data.

roughness is less than the Rms Z since they are calculated relative to different planes. But, in this study, they always deviate in the same direction.

At 800° C, Rms Z, mean roughness, peak count, and average peak height of film on silicon wafers and silica are at least the same as those of the as-deposited film. This may be due to a morphological change, since there was no compositional change.

At 850° C, all films showed greater measurements than those of the 800° C films. The film on the silicon wafer showed much greater increase in Rms Z, mean roughness, and peak count than those of silica. In addition, there appears to be crystal formation in the

850 C wafer film which can only be discerned from the top-view of the AFM scan, Figure 10b.

3.8 Infrared Analysis

The infrared spectra of the annealed films are shown in Figure 3-14 - Figure 3-16 along with their as-deposited spectra. Also, all the annealed IR spectra are shown for comparison in Figure 3-17. We see that the as-deposited films are highly transparent with much sharper absorption peaks than was predicted theoretically in section 2.11. The position of the absorption, near 690 cm^{-1}, indicates film composition of mostly AlN. After annealing, the film becomes less transparent to infrared and the single absorption peak appears to have split showing additional absorption near 620 cm^{-1} possibly indicating the formation of Al_2O_3. It is also apparent from the sequence of spectra in Figure 3-17 that higher annealing temperatures has subsequently enhanced the size of the secondary peak. This possibly indicates an increase in the relative composition of Al_2O_3 formed in the film as a result of annealing.

Pre- & Post-anneal Spectra - 760 C
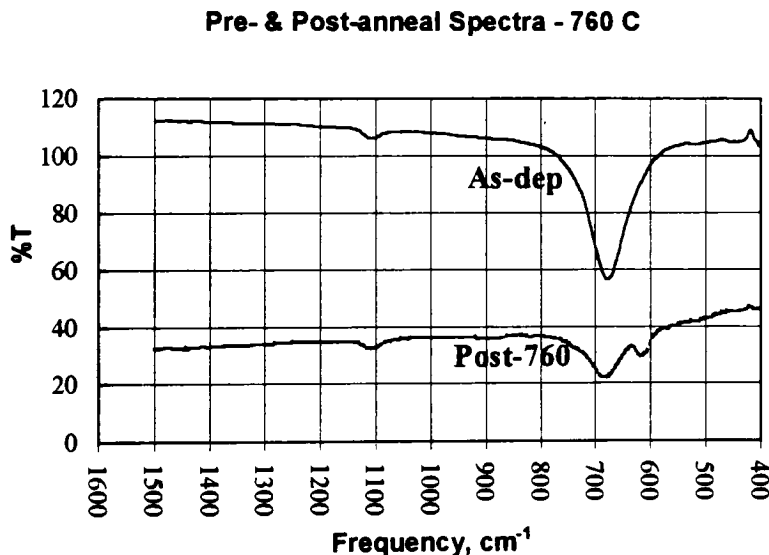
Figure 3-14 Infrared Spectra for 760 C.

Pre- & Post-anneal Spectrum - 800 C
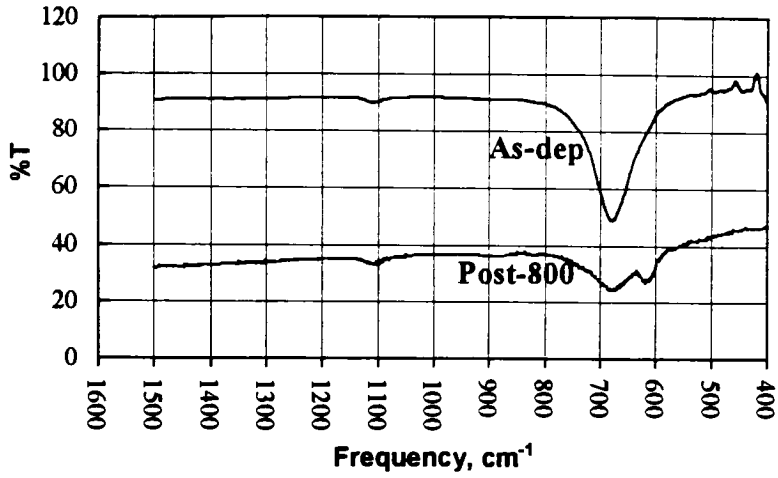
Figure 3-15 Infrared Spectra for 800 C.

Pre- & Post-anneal Spectrum - 850 C
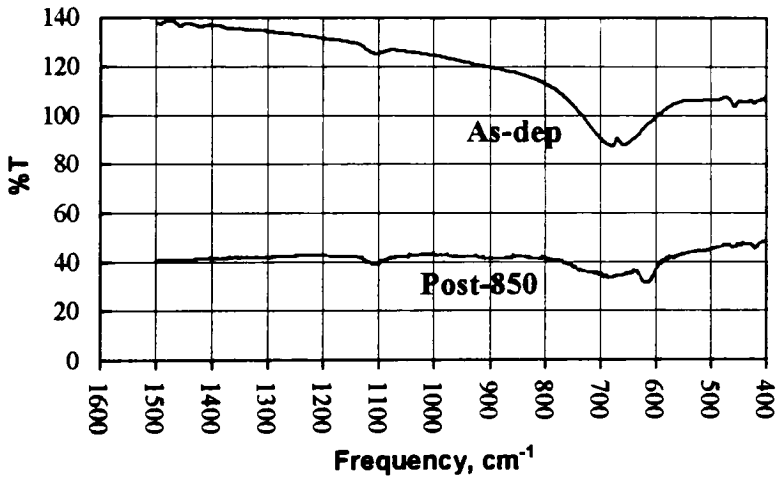
Figure 3-16 Infrared Spectra for 850 C.
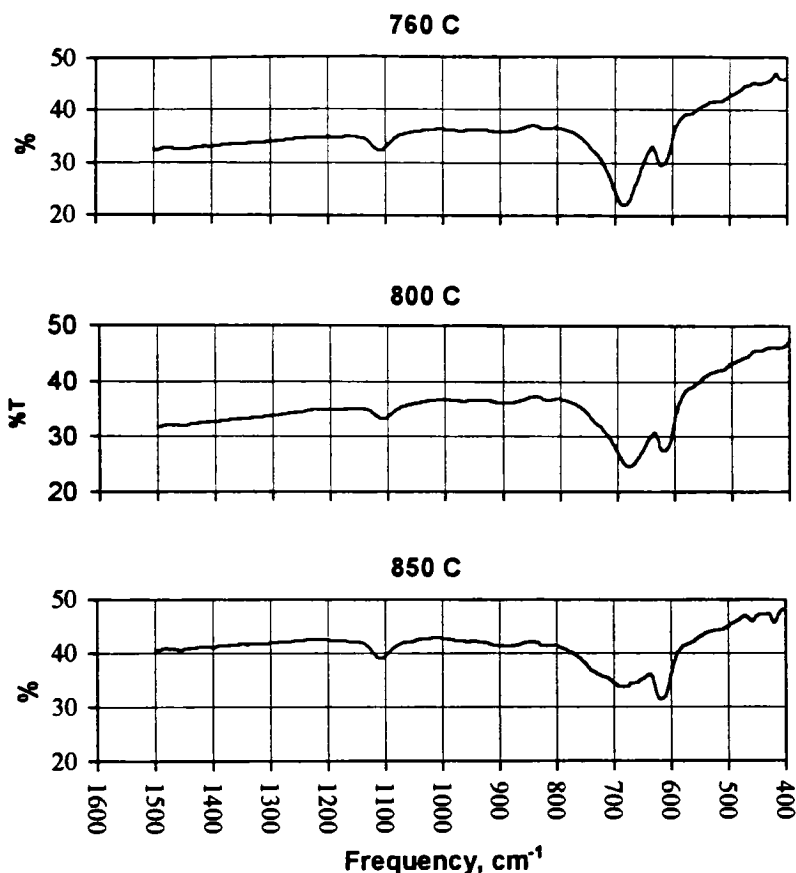
Figure 3-17 Post-anneal IR Spectra.

3.9 X-ray Diffraction Analysis

The x-ray diffraction spectra of the background and the film samples are shown in Figure 3-18. The spectrum of the 760° C annealed film is shown adjacent to the background spectrum to emphasize their similarity. This is further confirmation of the absence of structural order in that film as was concluded from the UV/Vis optical analysis.

The peaks in the remaining spectra correspond to the (002) planes (hexagonal (0002) planes in (h k i l) format) of bulk AlN indicated in Table 2-5. The 2θ position of each peak as determined by the analytical software JADE, is given in Table 3-7 along with the planar spacing represented by that peak. It is clear from the sequence of spectra that the film has some structure as deposited. Annealing at 760° C destroys that order and the film becomes amorphous. Films annealed at 800° and 850° C retained some degree of order.
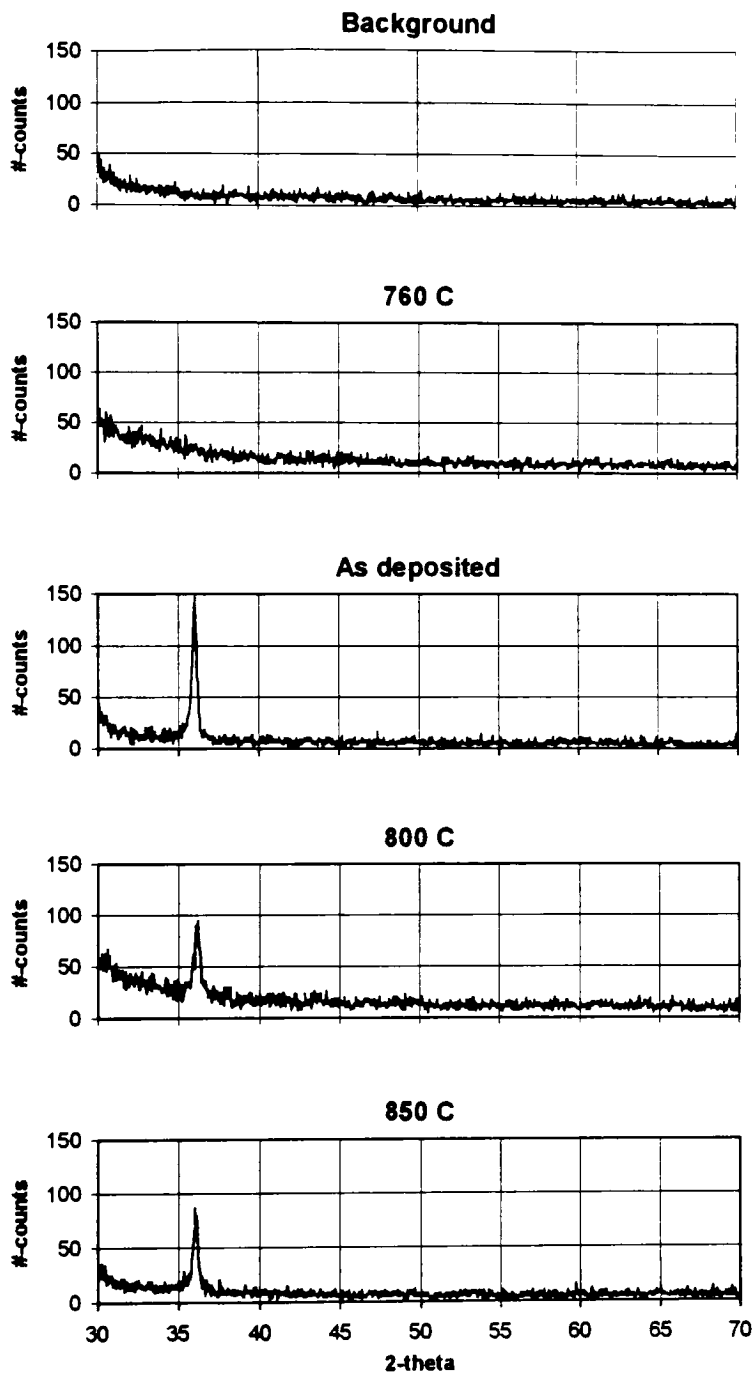
Figure 3-18 X-ray diffraction spectra of annealed and as-deposited film.

Film	Position (2θ)	d_{hkl} (Å)
As-dep	35.98°	2.49
800°C	36.15°	2.48
850°C	36.01°	2.49

Table 3-7 Summary of peak positions in AlN film.

4 Discussion

4.1 Clausius-Mossotti Calculations

The C-M relation can be tested using published ionic polarizabilities. For SiO_2 (fused silica), with a density of 2.65 gm/cm^3, $\alpha_D(Si^{+4}) = 0.88$ Å^3 and $\alpha_D(O^{-2}) = 2.0$ Å^3 as published by Shannon. The total $\alpha_D = 4.88$ Å^3 and $V = 37.67$ Å^3, so $(\varepsilon - 1)/(\varepsilon + 2) = 0.5433$ and $\varepsilon = 4.57$.

Similarly, the dielectric constant of AlN with a density of 3.28 gm/cm^3 can be determined from $\alpha_D(Al^{+3}) = 0.78$ Å^3 (from Shannon) and $\alpha_D(N^{-3}) = 2.24$ Å^3 The $\alpha_D(N^{-3})$ was determined from the dielectric constant and density of Si_3N_4, $\varepsilon = 6.5$, density = 3.1 gm/cm^3 and $\alpha_D(Si^{+4})$ from Shannon. The total $\alpha_D = 3.02$ Å^3 and $V = 20.76$ Å^3, so $(\varepsilon - 1)/(\varepsilon + 2) = 0.609$ and $\varepsilon = 5.68$. This is a perfectly legitimate dielectric constant since it is larger than $\varepsilon_\infty = 4.84$. The published dielectric constant at 1 MHz is $\varepsilon = 8.6$, so $\varepsilon = 5.68$ apparently applies to a much higher frequency possibly in the optical region. The frequency ranges to which Shannon's ionic polarizabilities apply can only be inferred from those of the 129 oxide-compound polarizabilities from which he derived them. The compound polarizabilities he used were measured by different observers, methods, and at frequencies. On the assumption that the polarizability of a compound can be predicted accurately as a linear combination of the ionic polarizabilities as described in section 2.7, Shannon applied a least squares fit to the linear system to obtain the ionic polarizabilities. So, it is difficult to specify a valid frequency range of some ionic polarizabilities, $\alpha_D(ion)$.[43]

4.2 Effects on Thickness and Refractive Index

The effects of annealing of the film samples were greatest at 800° C as illustrated in Figure 3-3. This indicates densification since the thickness decreased, the surface area of the film did not change, and there was no reason to believe that film material evaporated during annealing. Proportional increases in the index of refraction can also be observed in Figure 3-4.

4.3 Effects on Dielectric Constant

The capacitors formed on n+ doped wafers were measured at 1 MHz with the substrate biased in accumulation (+5v). The as-deposited film exhibits the largest dielectric

constant but the largest deviation from this occurred after annealing at 800° C where the dielectric constant came closest to the published value of $\varepsilon = 8.6$ (at 1 MHz). On either side of this annealing temperature, 760° and 850° C, the dielectric constants were significantly larger but not as large as that of the as-deposited film. This general trend is similar to that for the film's thickness under annealing.

4.4 Effects on Dielectric Breakdown

The application of a large dc potential to a capacitor plate until the film broke down resulted in a wide range of breakdown potentials at all annealing temperatures regardless of pad size. This can be seen in Table 3-3. The largest range of breakdown potentials occurred on film annealed at 800° C. The film annealed on either side of this, 760° and 850° C, experienced about the same range of breakdown potential while the as-deposited capacitors were all shorted.

The largest breakdown potentials occurred on capacitors with the smaller pad size. This indicates existence of physical leakage paths through the film and that annealing obliterated some of them.

4.5 Effects on the Band Structure

Extraction of the extinction coefficient of the annealed films from their transmittance and reflectance allowed the evaluation of their respective absorption characteristics. From the absorption spectrum of annealed and as-deposited film, Figure 3-10, we see that annealing at 760° C created a greater degree of disorder than the as-deposited state by the increase in low energy absorption. Annealing at higher temperatures (800° & 850° C), the same time period, leaves the film in increasingly higher degrees of order than the as-deposited state. This is confirmed by the shrinking low energy shoulder (at 800° C), and the absence of both a low energy shoulder and the linear region (at 850° C) of the absorption spectrum.

By fitting regions II & III of the absorption spectrum curves, parameters of the energy gap equation (2-68) were determined for the respective film sample and shown in Table 3-4. While the band gap of the as-deposited film (5.13 eV) is approximately the same as that of the 760° C film (5.20 eV), the slopes of their exponential sections differ

significantly. The smaller slope of the 760° C absorption is indicative if the higher state of disorder in that film compared to all the others. The band gap of the films annealed at 800 °C and 850° C are approximately equal but greater than those of as-deposited and 760° C state.

The material constant is independent of disorder and should be the same at each annealing temperature since the composition did not change due to annealing. The material constants for the 800° C and as-deposited films are within experimental accuracy but it is not clear why that of the 760° C film is more remote. The absorption coefficient can only be as accurate as the extinction coefficient which is a function of the spectrometer accuracy. The theoretical transmittances calculated from n and κ matched the experimental transmittances within instrument accuracy and calibration fluctuations.

Extensions of the linear portions of the absorption spectrum of all films (except the 850° C film) to the band gap energy converged at the same value, $\alpha_{Eg} \approx 1.6 \times 10^5$ cm^{-1}. This indicates the conservation of conduction and valence states as the material is annealed.

Analysis of state-to-band (SB) absorption in the low-energy shoulder summarized in Table 3-5 indicates that the greatest defect density occurs in the film that was annealed at 760° C which had thrice as many as the average as-deposited film. The film annealed at 800° C had the fewest defects, only 3/4 as many as the average as-deposited film. So, disorder in this material implies not only structural misalignment but vacancies as well.

Since there was no linear or low-energy absorption shoulder on the 850° C curve, the disorder of that film cannot be determined from E_o. Unfortunately the information needed to make the calculation from $\Delta E_g(T)$, eq. (2-71), is not available.

It may seem, at first thought, that the dielectric constant of the 800° C film (9.07) was lower than that of the others because its defect density is lowest. This would not be quite consistent since the estimated defect density of the 760° C film was twice that of the as-deposited material but, the dielectric constant of the former (10.15) was considerably less than the latter (11.75). Also, the dielectric constant of the 850° C film (10.65) was only slightly larger than that of the 760° C film. But, as stated previously, the shape of its absorption characteristics indicate it is in a much more ordered state than any of the other

films; as-deposited or annealed. So, the estimated defect densities alone do not explain the dielectric constant paradox.

The defect density and state of disorder does not explain the morphological changes either. It appears that maximum disorder of the film at 760° C correlates with smoothest topography and fewer structures (lowest peak count) regardless of the substrate. Also, maximum order of the film occurs at 850° C correlates with the maximum roughness, peak count, and, in the case of the wafer film, crystallization. The electronic dielectric constants of the annealed films differ by no more than ±0.5.

4.6 Nature of the defects

In the study of the affects of oxygen contaminates in AlN ceramics, it was generally understood that O atoms substitutionally occupy N sites and are well situated near an Al vacancy. This is best explained by the following reaction where $(O_N)^{\cdot}$ represents an O atom substituting on a N site and $(V_{Al})^{'''}$ is an Al vacancy. It tells us that for every three

$$AlN + xAl2O3 \rightarrow Al_{1-1/3x}N(O_N)^{\cdot}_x(V_{Al})^{'''}_{1/3x} \qquad (4\text{-}1)$$
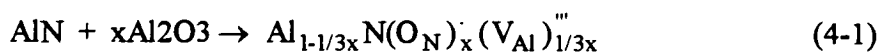
oxygen atoms incorporated on N sites, there exists one Al vacancy. These two conditions, O substitutions and Al vacancies, along with sintering temperatures, facilitate the conversion of tetrahedrally coordinated Al to octahedrally coordinated Al.[44]

The leakage current of GaN capacitors was interpreted by Zolper et. al. as an indication of vacancies due to N loss.[45] Nitrogen vacancies are believed to contribute to the n-type conductivity in GaN film. Aluminum nitride film (~120 nm) was used as a protective coating on selected GaN films (1.5 - 2.0 μm thick) while others were left unprotected. On annealing at 1100° C for 15 s under flowing N_2, Schottky and ohmic contacts were deposited. Unprotected GaN film experienced greater N loss than protected film. The loss was detected as a 3 - 4 order-of-magnitude increase in the leakage current of reverse-biased GaN/contact diodes. The N loss was further verified by AES depth profiling after removal the surface carbon.

This same phenomena may explain the poor breakdown performance of the film samples in this study. Nitrogen vacancies are suggested by the low reactivity of N_2 and further by the low N content from the AES estimates. The AlN capacitors made from as-

deposited film always leaked under d.c. bias. But, half the capacitors made from annealed films showed no leakage current until broken down. Once again it appears that annealing has eliminated some leakage paths.

4.7 Analysis of the Infrared Spectra

When the theoretical approach described in section 2.11 was applied using trial compositions and thicknesses, the transmittances in Figure 4-1 were generated for different film thicknesses. They closely resemble those generated by the authors, Figure 2-9. Also, the transmittances of AlN film of various compositions designated by the given format do not deviate significantly as can be seen in Figure 4-2.

The model used by the authors is based on the molecular structure $(AlO_{3/2})_{1-z}(AlN)_z$ which is derived from $(AlO)_xN_y$. The variables x, y, and z are molar fractions that are related by $z = 3/[2(x/y) + 3]$. Also, x and y do not have to sum to 1. Immediately, it is clear that these formulae are stoichiometrically incompatible with this AlN material which is heavily Aluminized. All of the N and O can be accounted for in these expressions, but there is Al left over and it is not clear what morphology it takes before and after annealing. Oxygen atoms may substitute at N sites as indicated in eq. (4-1), but there are very few, if any, Al vacancies. The abundance of Al may account for the crystal formation in the film that was annealed at 850° C (Figure 10 of the appendix). Aluminum crystallizes in a cubic structure so it is not likely that the surplus aluminum is metallizing since the crystals on the 850° C film have formed triangular outlines, indicating the presence of hexagonal or tetragonal structures.
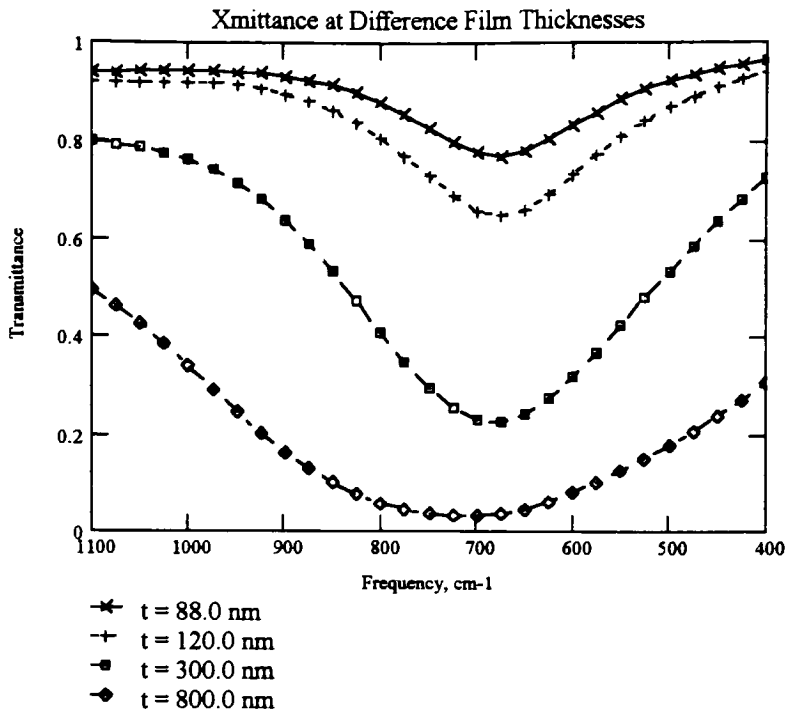
Figure 4-1 Transmittance of different film thicknesses based on the Ansart model.
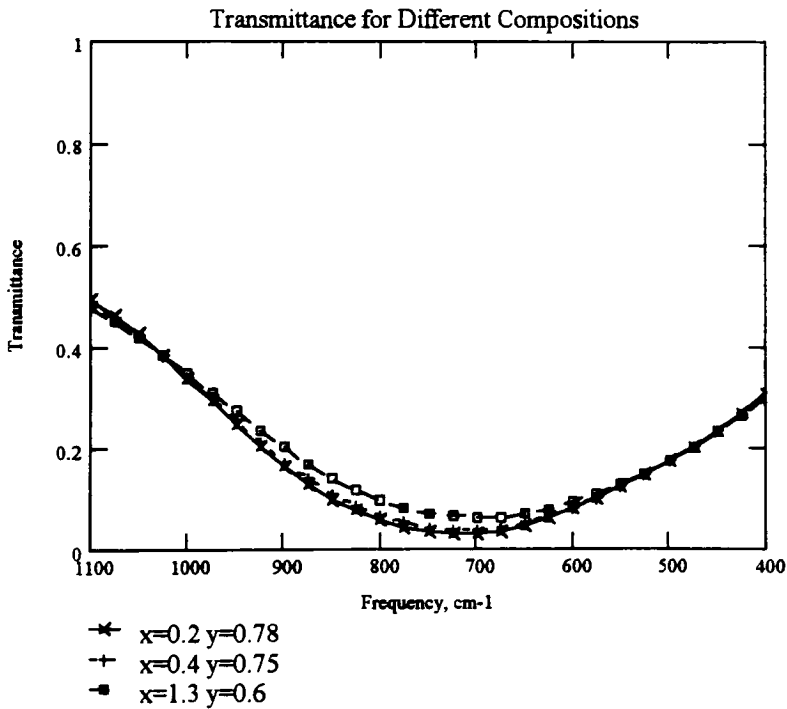
Figure 4-2 Transmittance of different compositions based on Ansart model.

71

4.8 Analysis of the X-ray Diffraction Spectra

The x-ray diffraction spectra indicate a small decrease in (0002) planar spacing in the 800° C film in addition to a relative decrease in its thickness noted in section 4.2. The decrease in planar spacing cannot be taken as an explanation of the thickness change since the presence of anion vacancies may also play a role.

As stated in section 2.11, AlN oxidizes into δ- and θ-alumina when annealed at 850° - 1200° C in the presence of oxygen. These films already contain oxygen which may explain any reactions with prior to 850° C. The three most intensive diffraction peaks of δ-alumina occur at $2\theta = 67.31°$, $32.78°$ in decreasing order & $45.55°$ and those of θ-alumina at $2\theta = 67.31°$, $31.36°$ & $32.90°$ also in decreasing order. The presence of α-alumina is ruled out since the annealing temperature did not reach 1200° C. The absence of the most intense peak at 67.31° from the above spectra may be due more to background noise than the absence of alumina phases. [46]

5 Conclusions

In their as-deposited state, the films are nitrogen deficient, and exhibit poor breakdown strength according to the results in Table 3-2.

Annealing at 760° C did not significantly affect the surface topography of the film in comparison to the as-deposited surface on either Si or silica plates. This is can be seen from the AFM images in the appendix and the roughness summary in Table 3-6. Annealing at higher temperatures caused oxidation of the AlN and improved the films breakdown characteristics as seen in Table 3-2 and Table 3-3.

The film has some order when deposited. The structure is predominantly hexagonal (0002) AlN planes, which exhibit maximum scattering intensity. Annealing at 760° C introduces more disorder. This characteristic is seen in the absorption and x-ray spectra (Figure 3-10 and Figure 3-18 respectively). Subsequent annealing at 800° C and 850° C systematically increases the degree of order in the film also observed in the same diagrams.

The films exhibited a dielectric constant of approximately 10 and was not significantly affected by annealing. This is born out by dielectric constant measurements in Table 3-2. Also, optical analysis in Figure 3-11 show the real permittivity, ε_1, of the annealed films varied less than ± 0.5 from ε_∞ of 4.84.

Further characterization studies of this material include optical analysis of film deposited under different Ar:N_2 environments. A thorough chemical analysis of each film via XPS (X-ray Photoelectron Analysis) and AES is also needed to determine the exact Al, N, and O composition and the bonding that results from each anneal.

An in-plane measurement of the dielectric constant may confirm the presence of orientational polarization. This could explain the why the out-of-plane dielectric constants reported in section 3.4 are greater than the bulk dielectric constant (8.9).

Whereas this work was in partial satisfaction of an academic endeavor, the topic has industrial interest and value. Academia cannot provide all the tools needed to compete with industry. The skills acquired in obtaining and interpreting this data however are enduring and pertinent to the materials industry.

6 Appendix

The illustrations that follow are the reflectance and transmittance of film samples on silica plates. Each graph shows the spectrum before and after annealing.

Pre- & Post-anneal (850 C) Reflectance

Pre- & Post-anneal (850 C) Transmittance
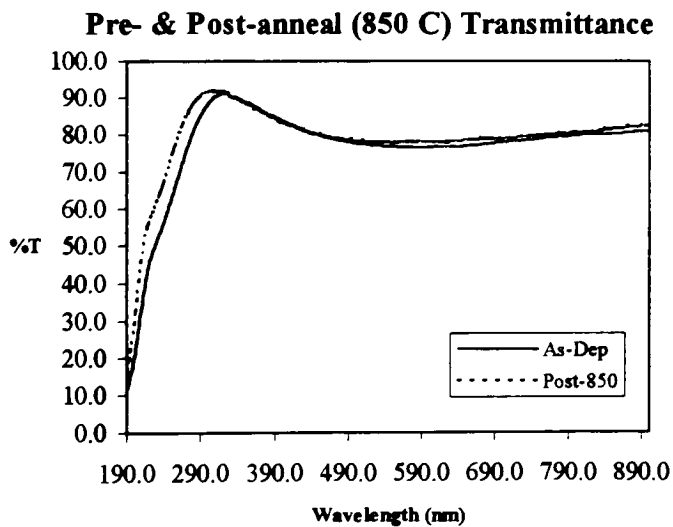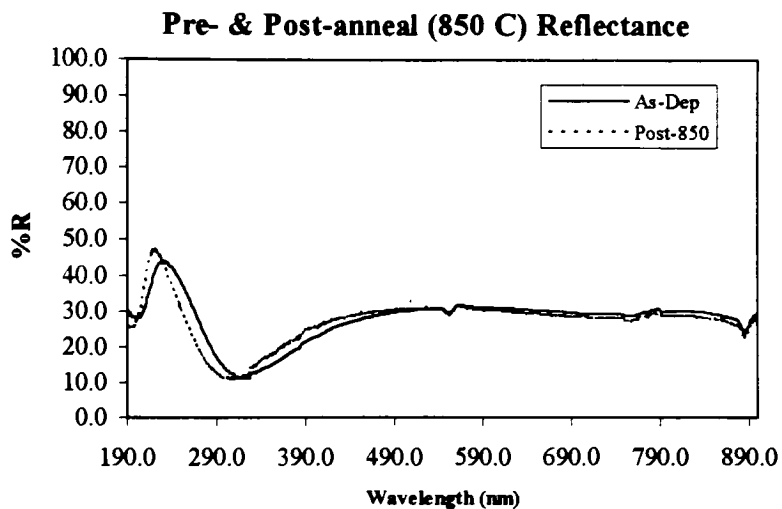
Figure 6-3 Reflectance (above) and Transmittance (below) at 850 C.

Pre- & Post Anneal (800 C) Reflectance

%R vs **Wavelength (nm)**

Legend: As-Dep, Post-800

Pre- & Post Anneal (800 C) Transmittance

%T vs **Wavelength (nm)**

Legend: As-Dep, Post-800
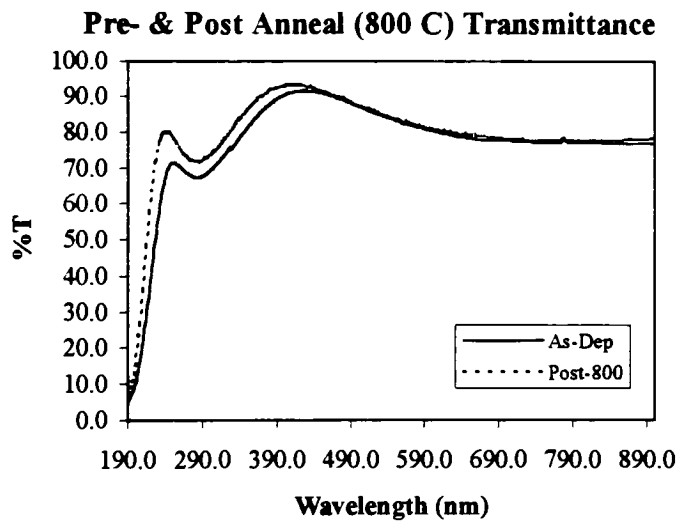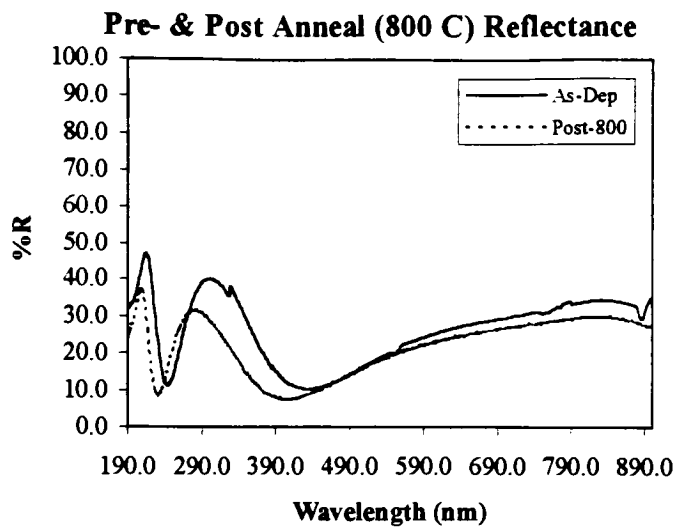
Figure 6-4 Reflectance (above) and Transmittance (below) at 800 C.

Pre- & Post-anneal (760 C) Reflectance

Pre- & Post-anneal (760 C) Transmittance
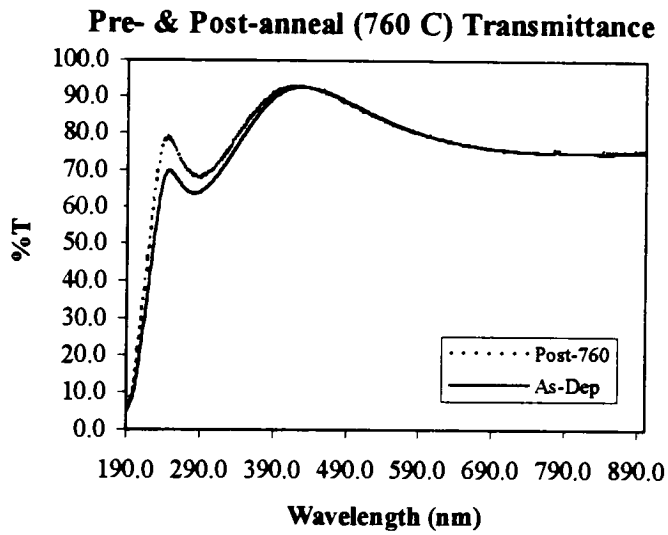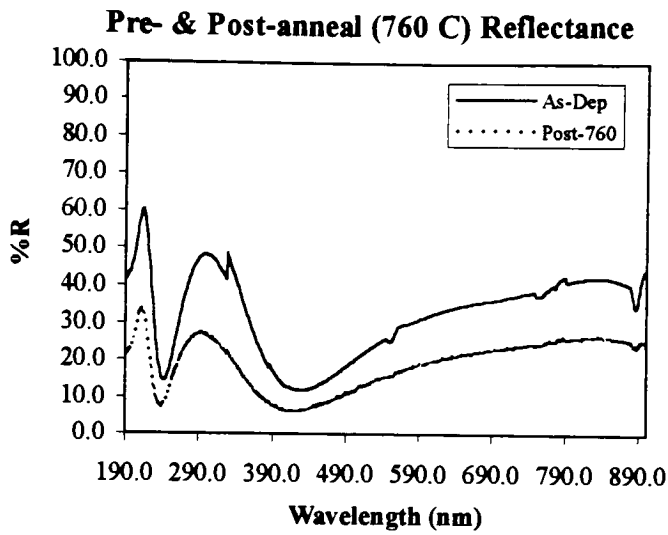
Figure 6-5 Reflectance (above) and Transmittance (below) at 760 C.

6.1 The Predicted Transmittance

The following diagrams are comparisons of the theoretical and experimental transmittances of the annealed film. The theoretical transmittances were calculated from n and κ extracted from the experimental transmittances and reflectances by the "Fresnel" utility. The Fresnel utility generated n and κ spectra of 150 points over the given spectrum on an energy (E) scale. They were converted back to a wavelength (nm) scale using the relation,

wavelength [nm] = 1239.85/E [eV]. A subset of the experimental transmission spectrum (711 points) was taken using the wavelength closest to that calculated as above. Although the two scales are slightly different, there is no visible difference between spectra plotted on either scale.
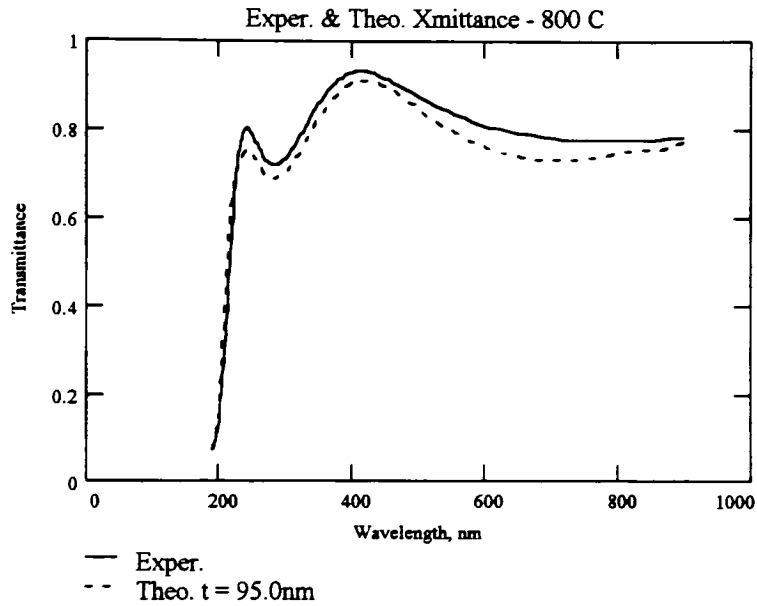
Figure 6-6 Theoretical Transmittance (800 C) from n & κ.

Exper. & Theo. Xmittance - 850 C

— Exper.
- - Theo. t = 71.9 nm
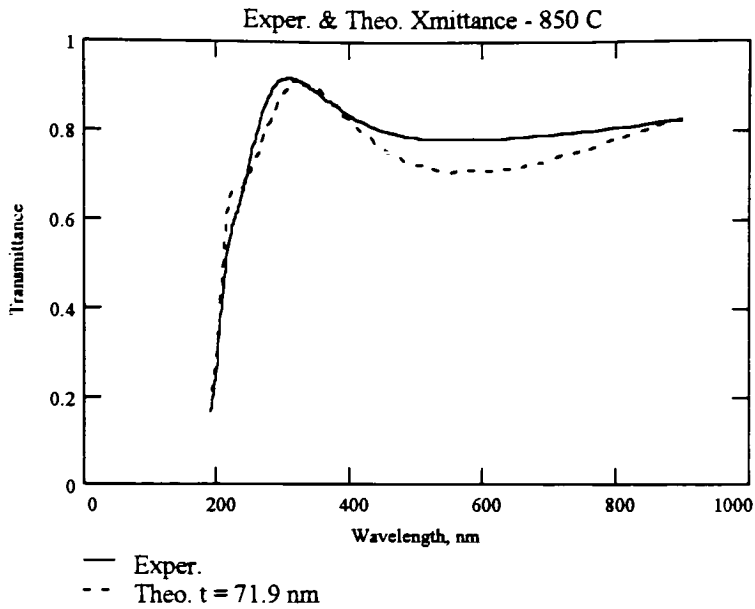
Figure 6-7 Theoretical transmittance (850 C) from n and κ.

Exper. & Theo. Xmittance - 760 C

— Exper.
- - Theo. t = 103.0 nm
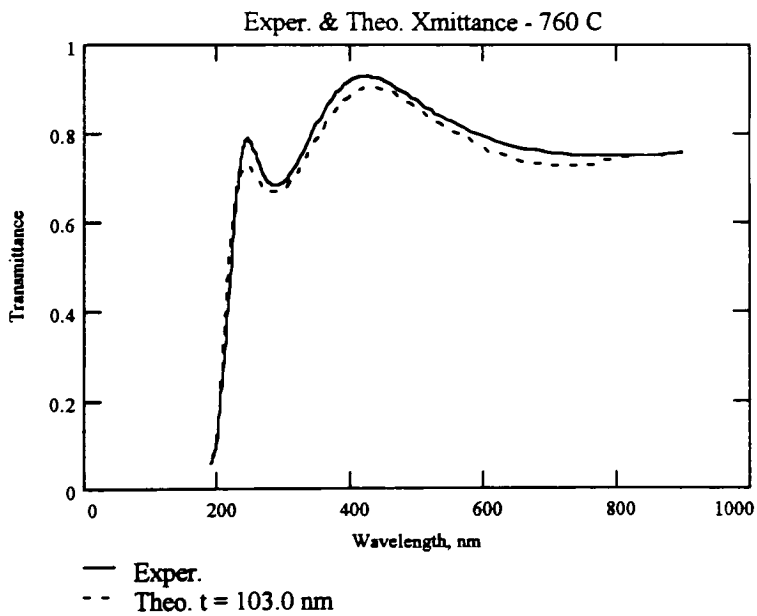
Figure 6-8 Theoretical transmittance (760 C) from n and κ.

Figure 1. SIMS survey scan of 760 C film.

Negative SIMS Depth Profile 26 Jul 96 Al2N63 Region: 5 Time: 30.00 min Sputter Angle: 60.8

File: SKALN_2 AlN/Si annealed 760C

Ep: 5.00 kV Ip: 51.00 nA Cs+

350x350um2

Log (Counts / Second)

Sputter Time (min)
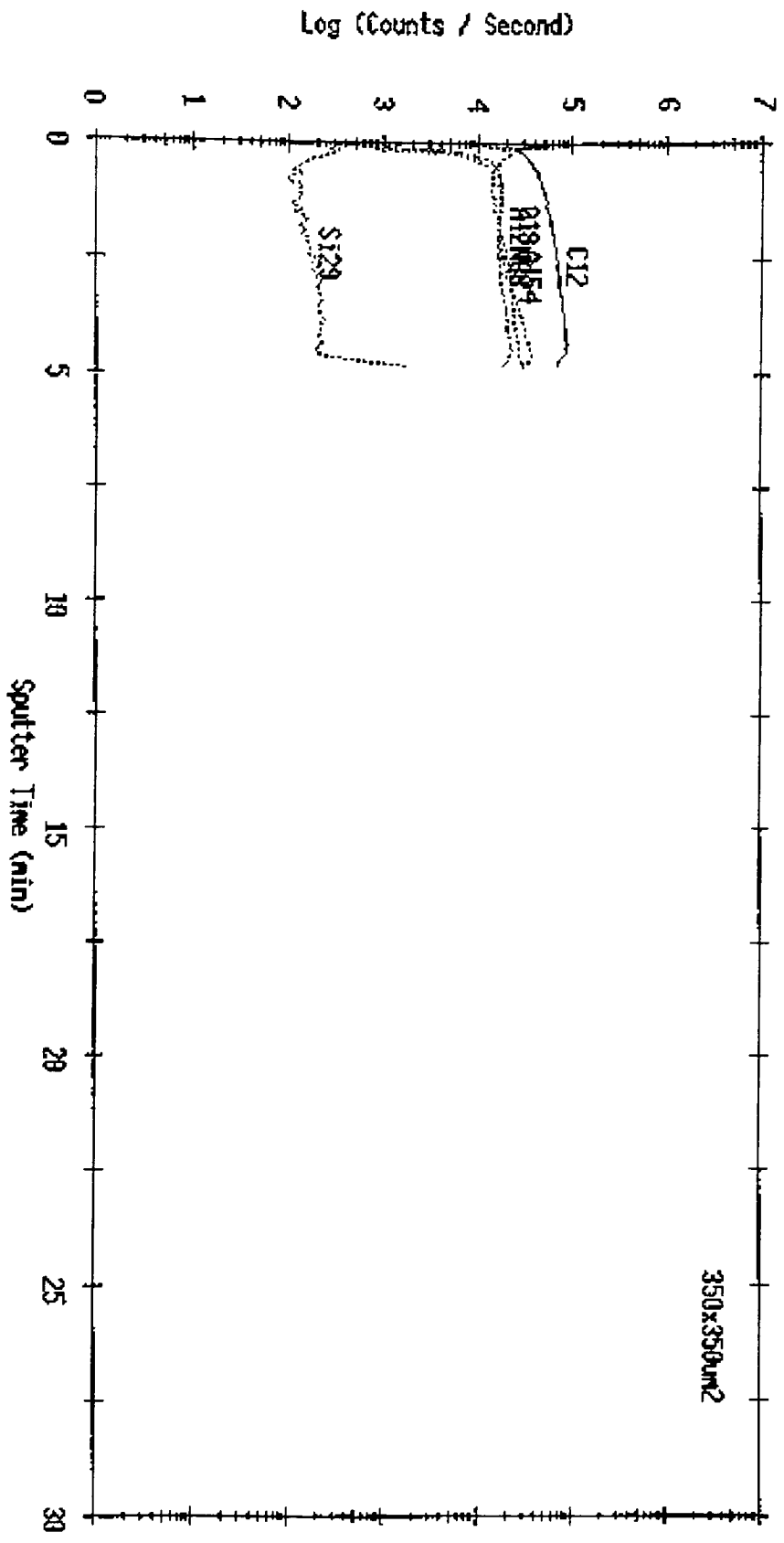
Figure 2. SIMS depth profile of 760 C film.

Negative SIMS Depth Profile 26 Jul 96 Al2N63 Region: 5 Time: 30.00 min Sputter Angle: 60.8

File: SiReN_3 AlN/Si annealed 800C

Ep: 5.00 kV Ip: 51.00 nA Cs+

Log (Counts / Second)

Si29

Cl2

350x350um2

Sputter Time (min)
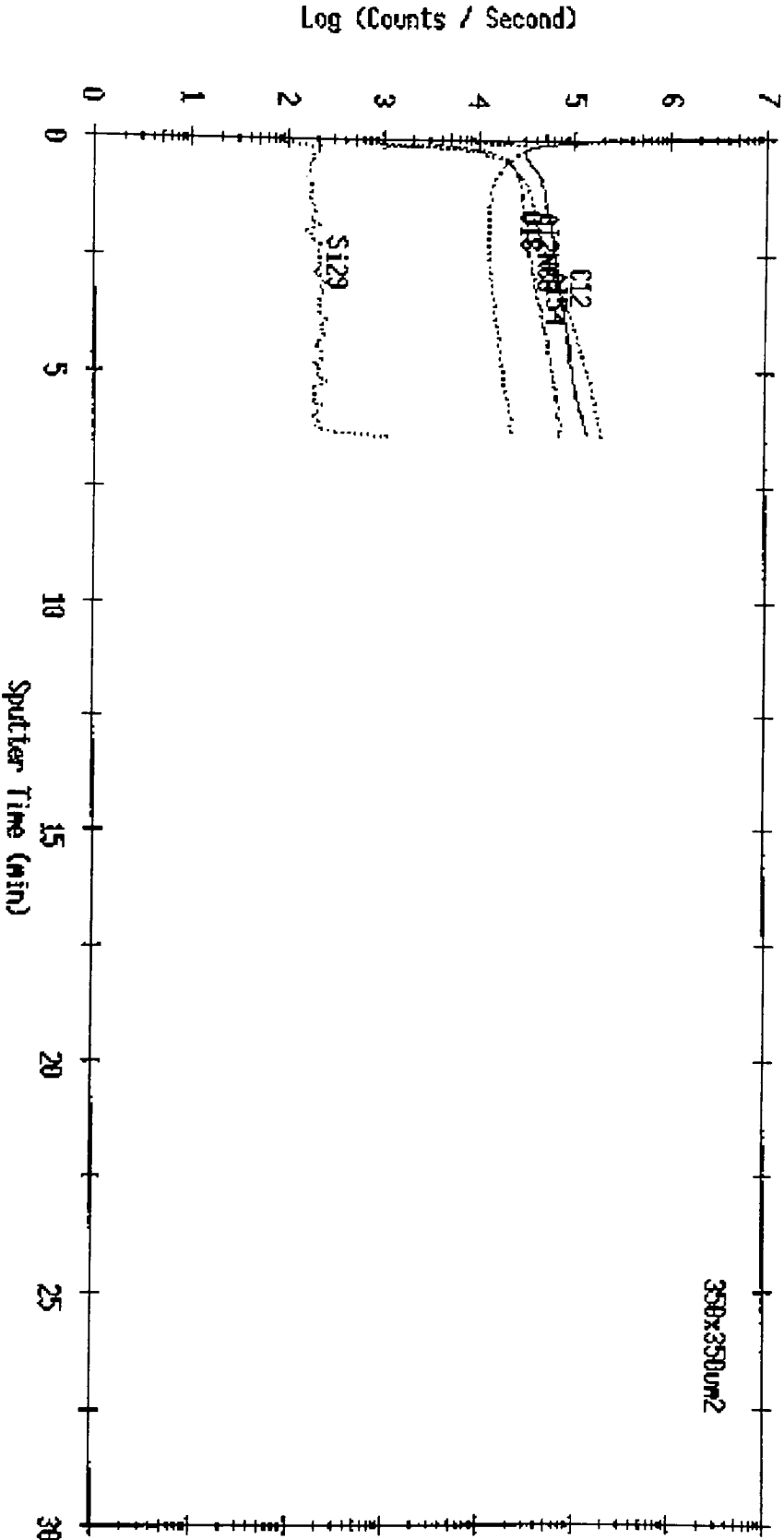
Figure 3. SIMS depth profile of 800 C film.

AES SURVEY V/T   7/18/96 AREA 1 ACQ TIME=10.00 MIN.

FILE: 760_2 AlN annealed at 760C

SCALE FACTOR= 53.602 k c/s,   OFFSET= 0.000 k c/s

BV=5.00KV BI=0.0000uA

N(E)*E, diff9

KINETIC ENERGY, eV

Al
58

Ar
215

N
381

O
328

AL
1390
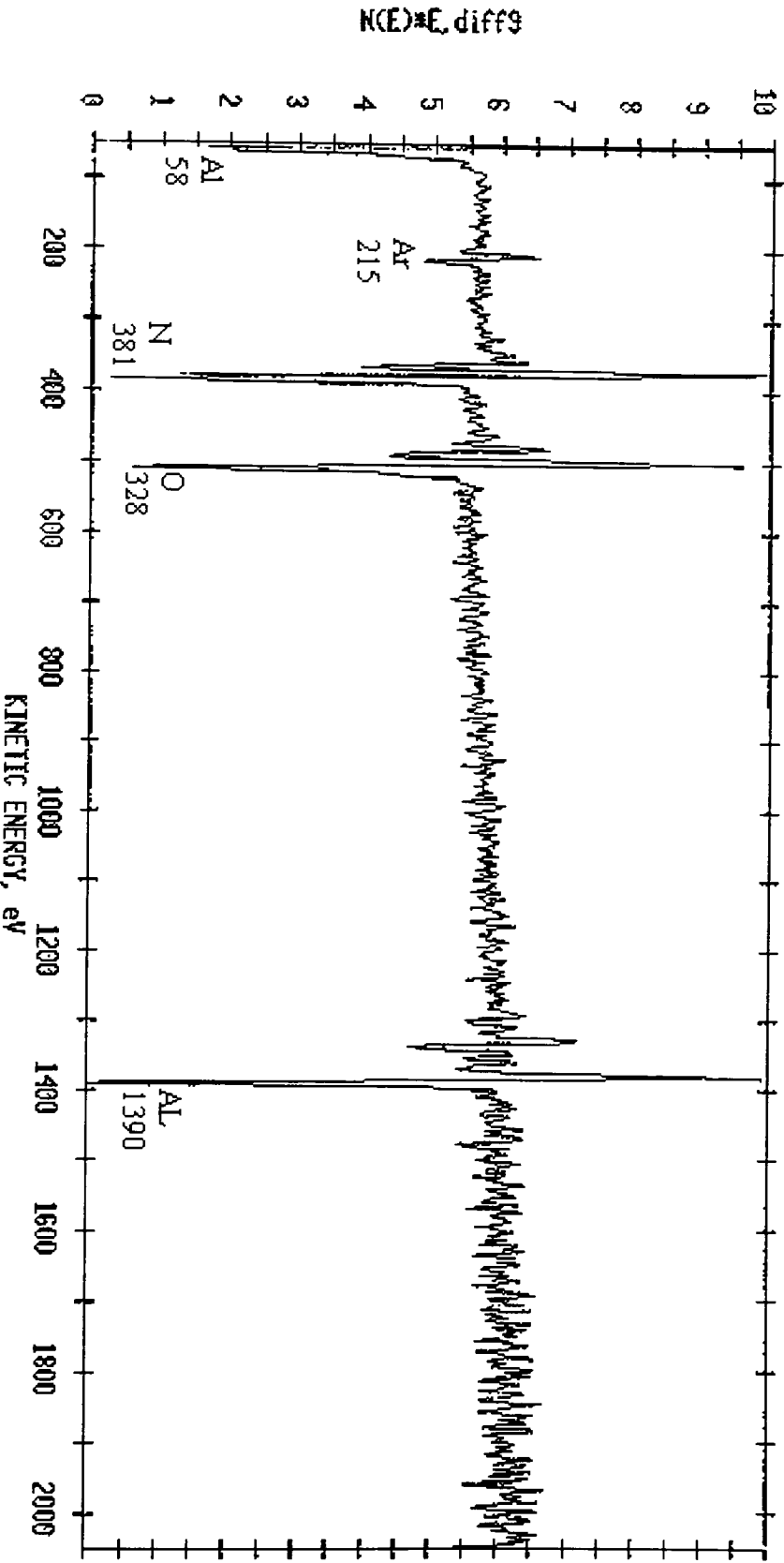
Figure 4. Auger spectrum of 760 C film.

AES SURVEY V/F   7/18/96 AREA 1 ACQ TIME=10.00 MIN.

FILE: 800_2 AlN annealed at 800C

SCALE FACTOR= 56.789 k c/s,   OFFSET= 0.000 k c/s   BV=5.00kV BI=0.0000uA

N(E)*E,diff9

AR
215

N
380

O
506

Al
1384

KINETIC ENERGY, eV
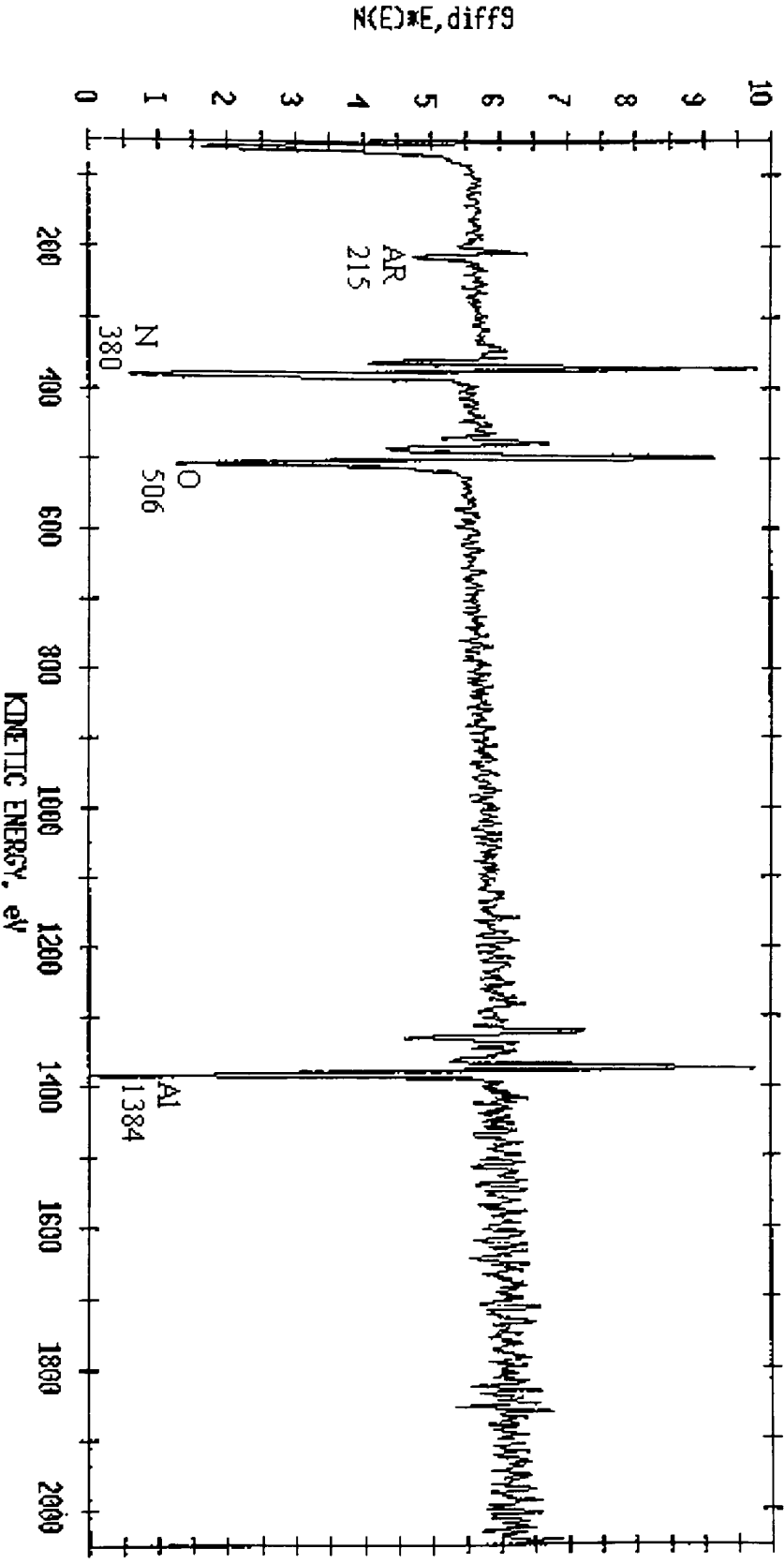
Figure 5. Auger spectrum of 800 C film.
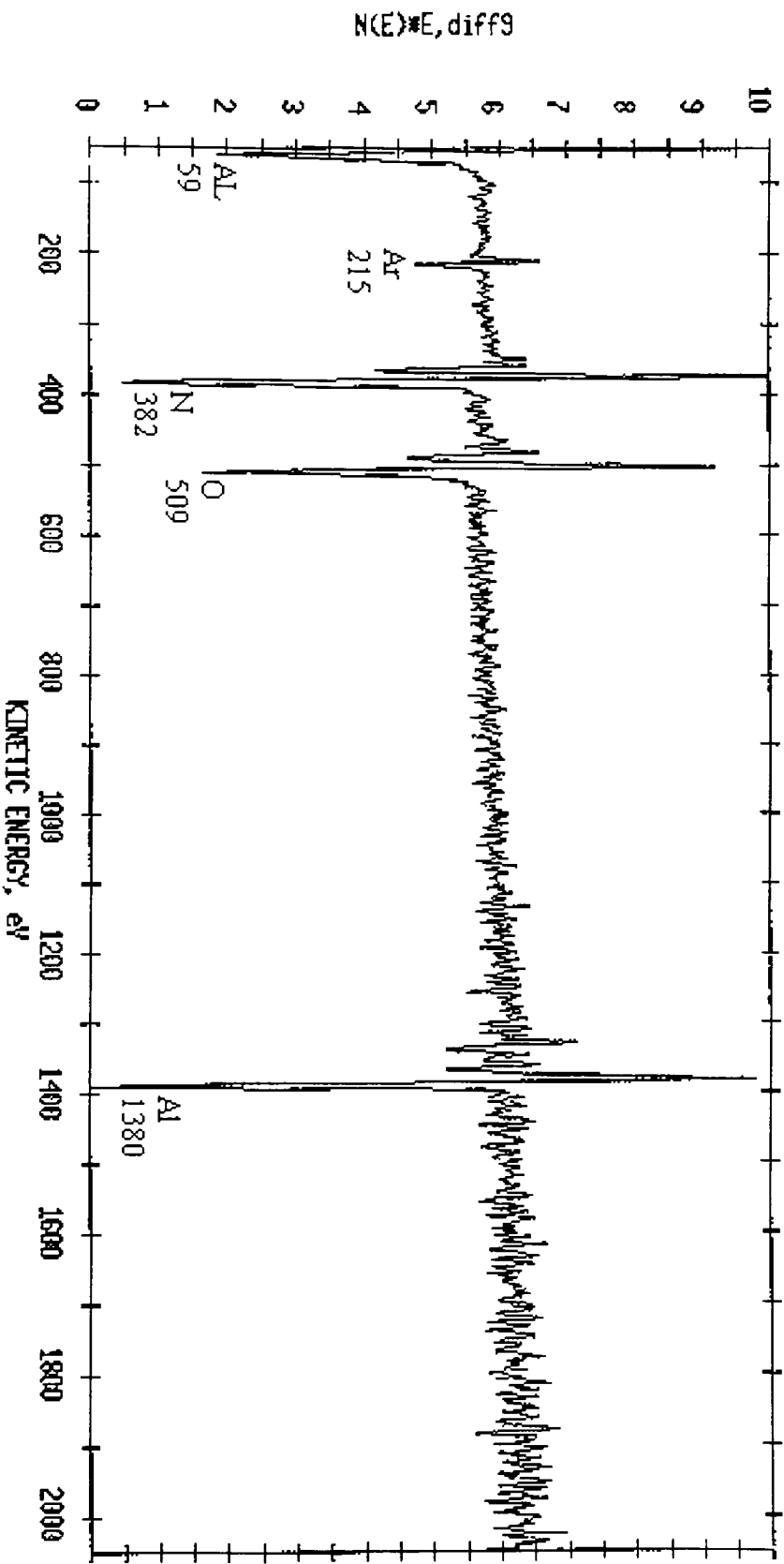
Figure 6. Auger spectrum of 850 C film.

X   0.200 µm/div
Z   15.000 nm/div
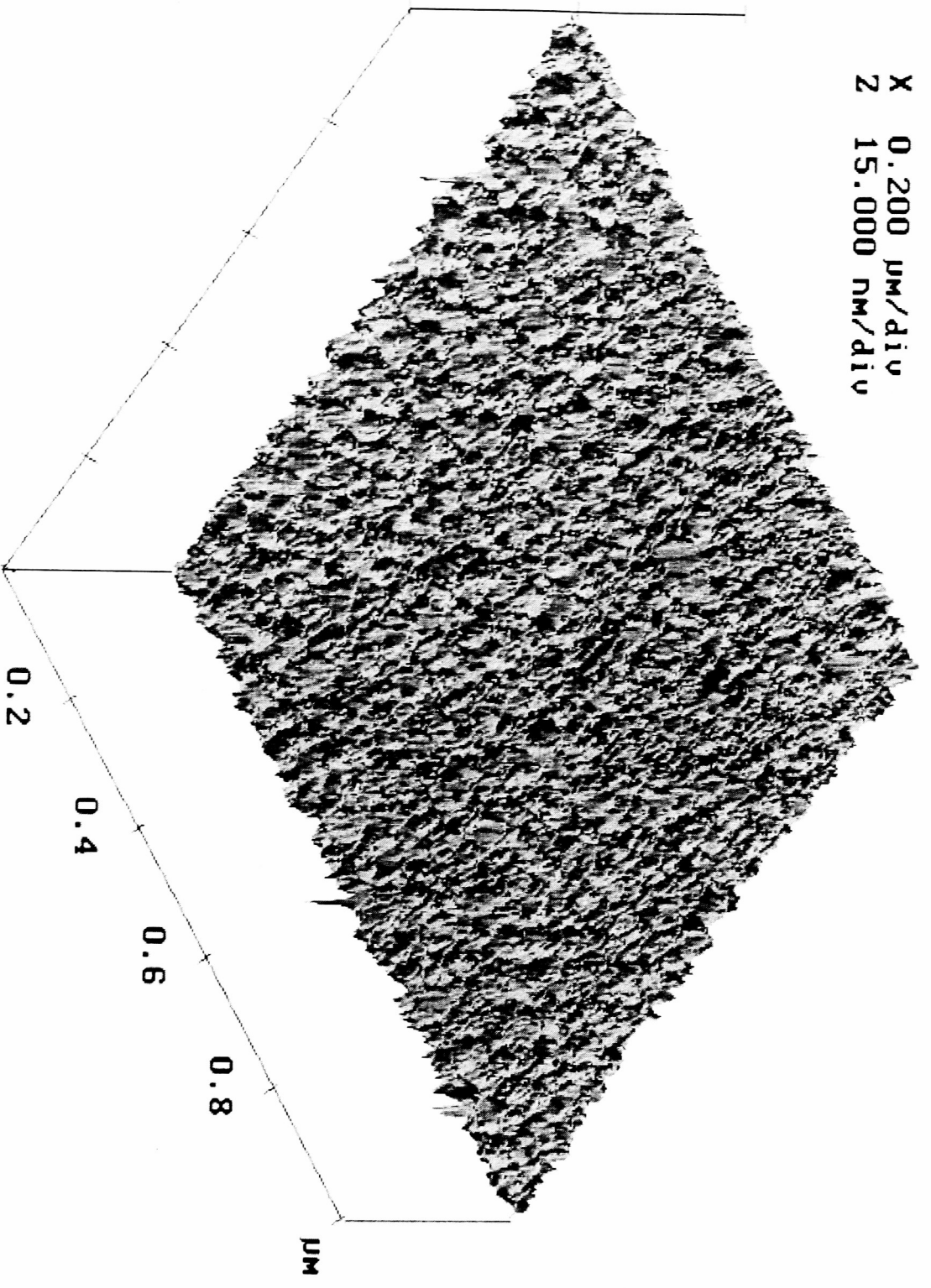
Figure 7a. AlN film on Si as deposited.

0.2

0.4

0.6

0.8

µm

X   0.200 µm/div
Z   15.000 nm/div

Figure 7b. AlN film on silica as deposited.

X 0.200 µm/div
Z 10.000 nm/div
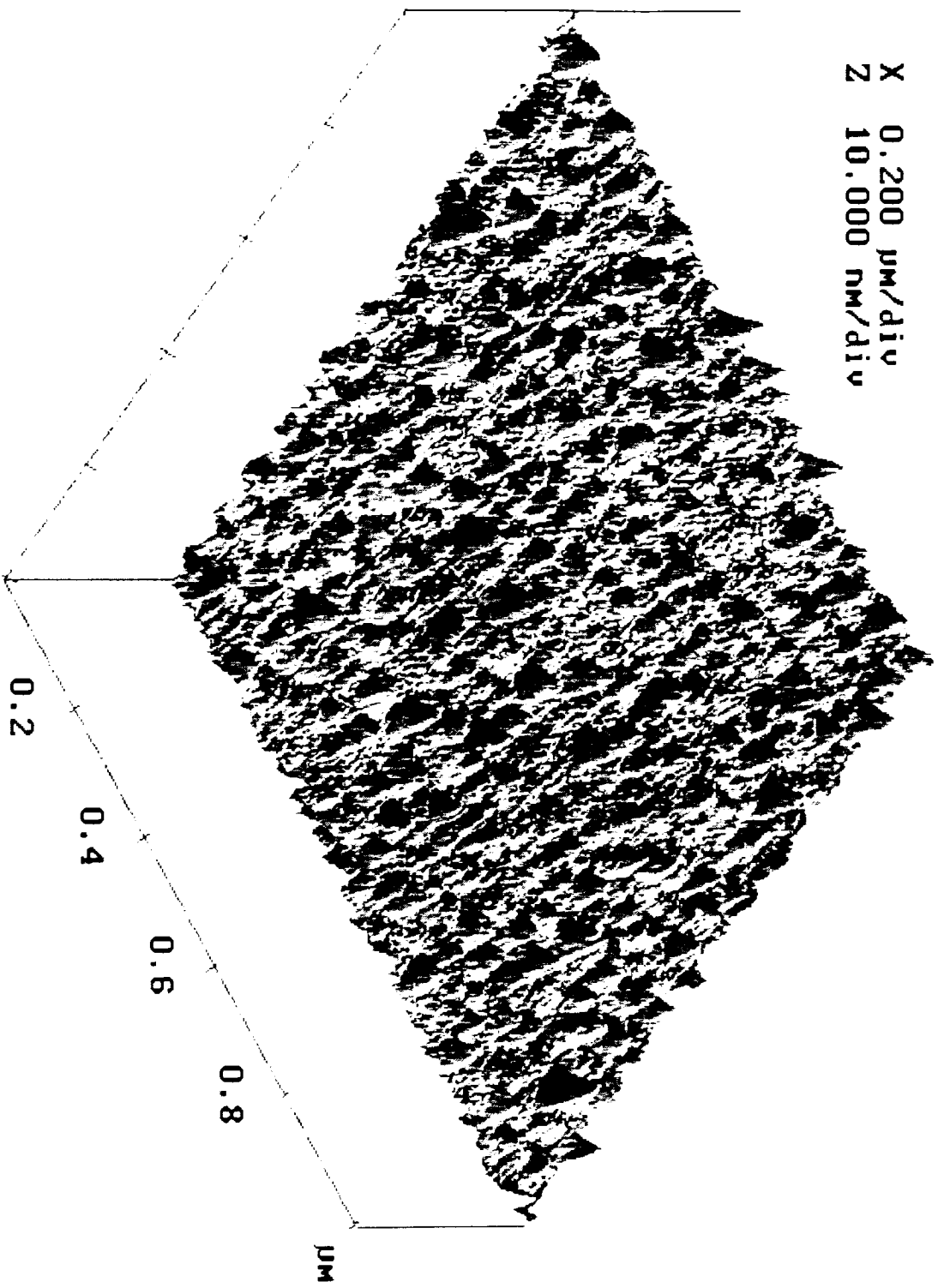
Figure 8a. AlN film on Si & annealed at 760 C.

X   0.200 μm/div
Z   5.000 nm/div
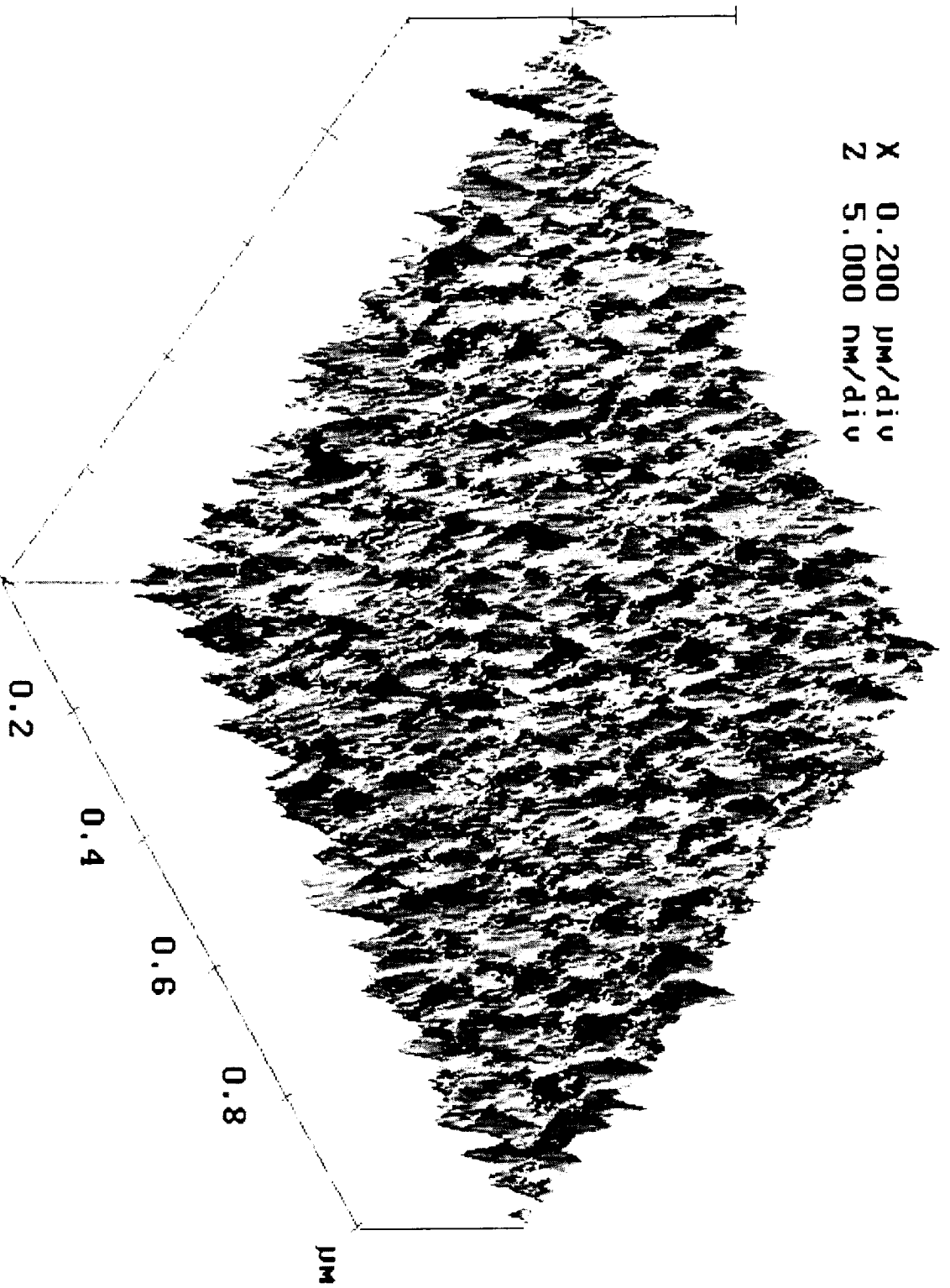
Figure 8b. AlN film on silica & annealed at 760 C.

0.2   0.4   0.6   0.8   μm

X   0.200 µm/div
Z   10.000 nm/div
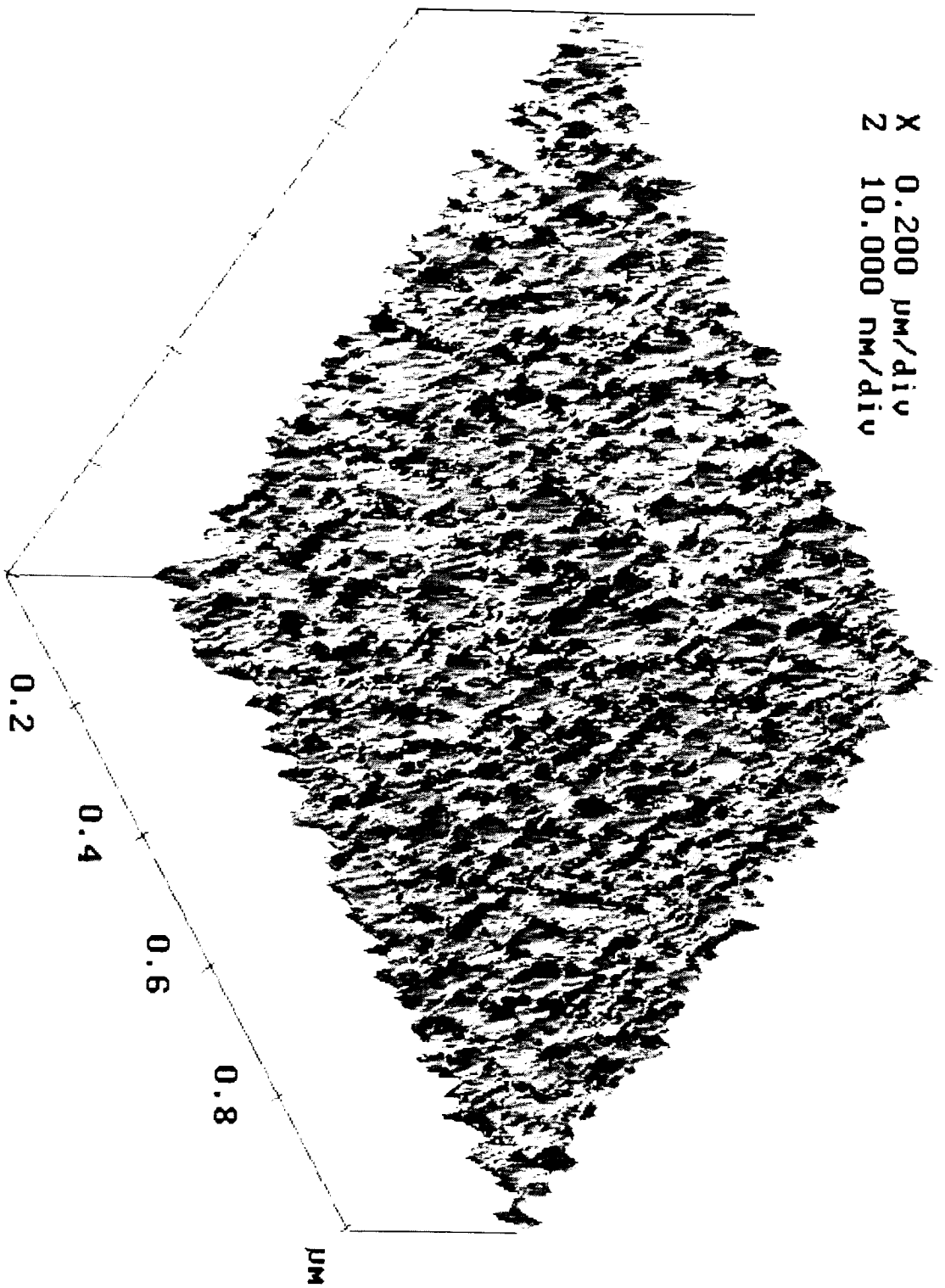
Figure 9a. AlN film on Si & annealed at 800 C.

X   0.200 µm/div
Z   15.000 nm/div
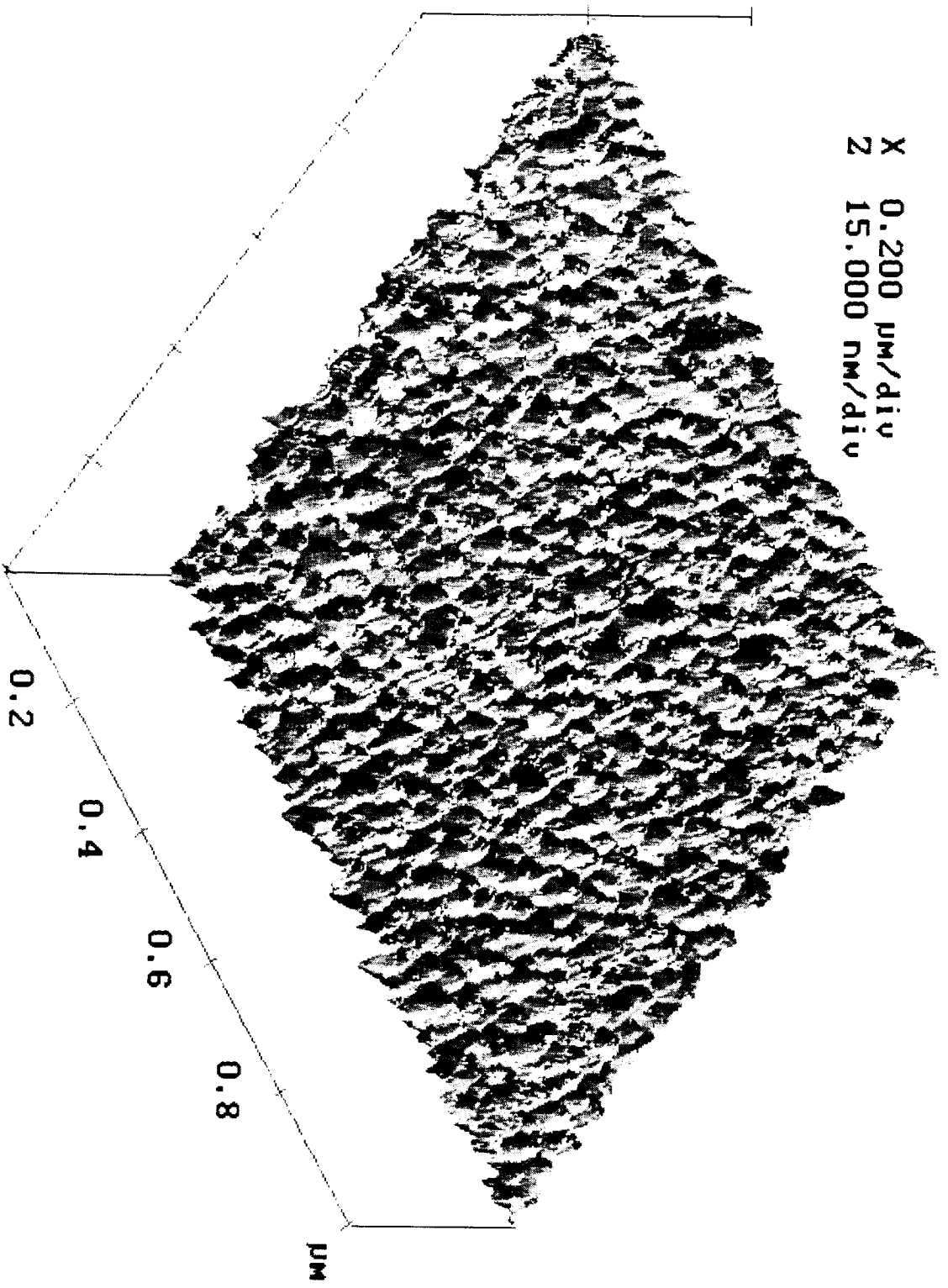
Figure 9b. AlN film on silica & annealed at 800 C.

0.2

0.4

0.6

0.8

µm

X 0.200 μm/div
Z 15.000 nm/div
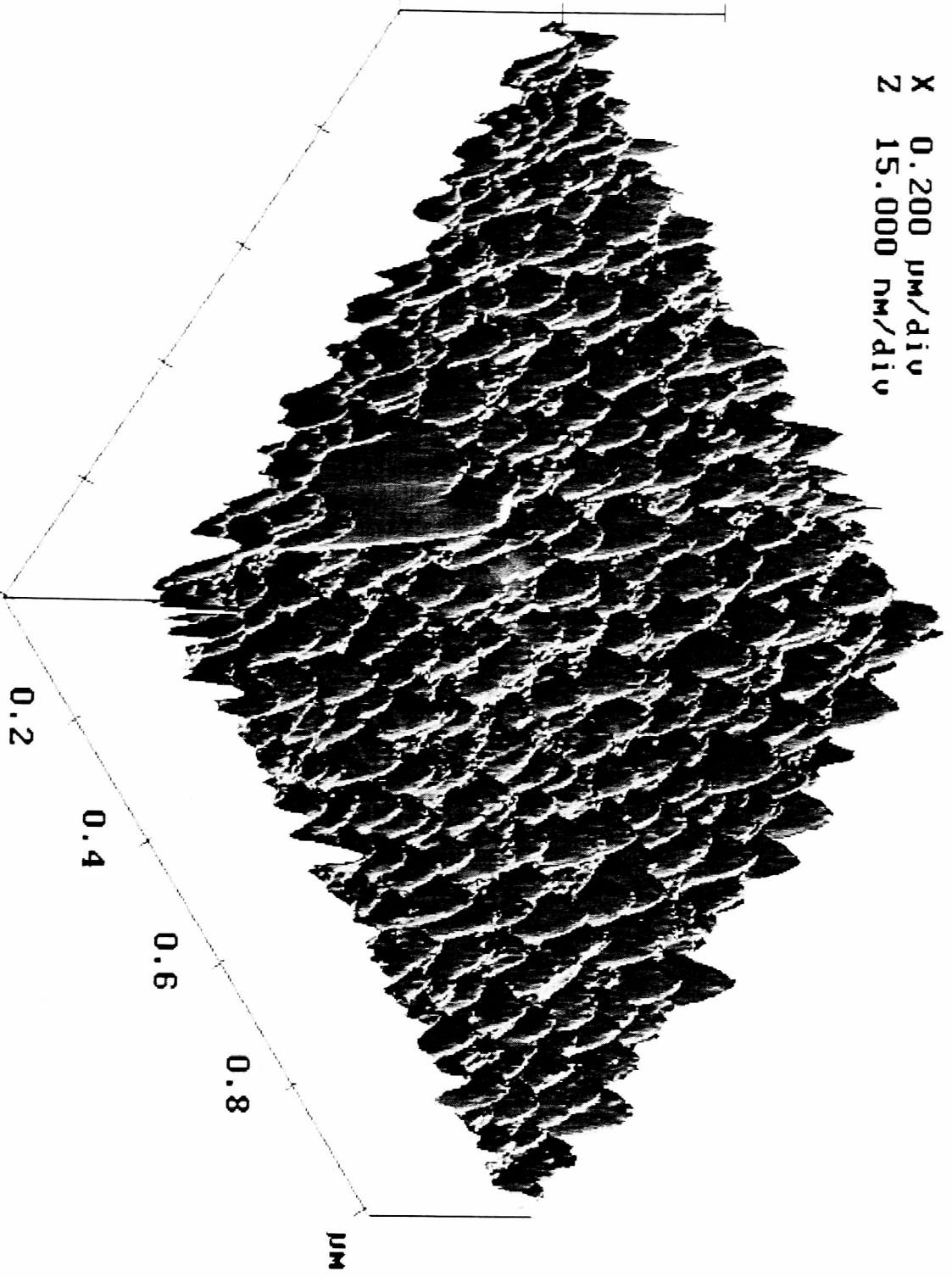
Figure 10a. AlN film Si & annealed at 850 C.
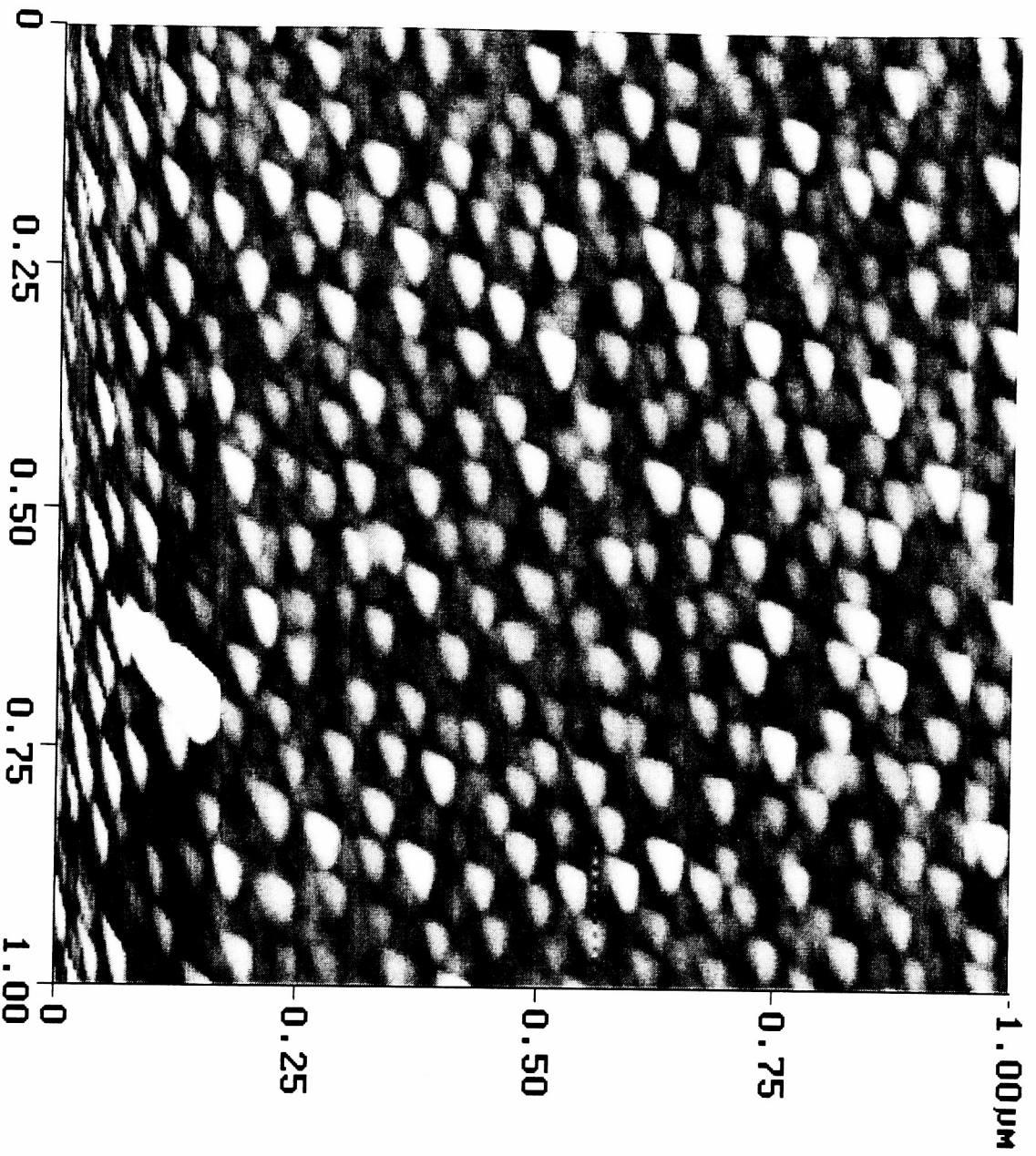
Figure 10b. AlN film on Si (top view) & annealed at 850 C.

X   0.200 µm/div
Z   15.000 nm/div
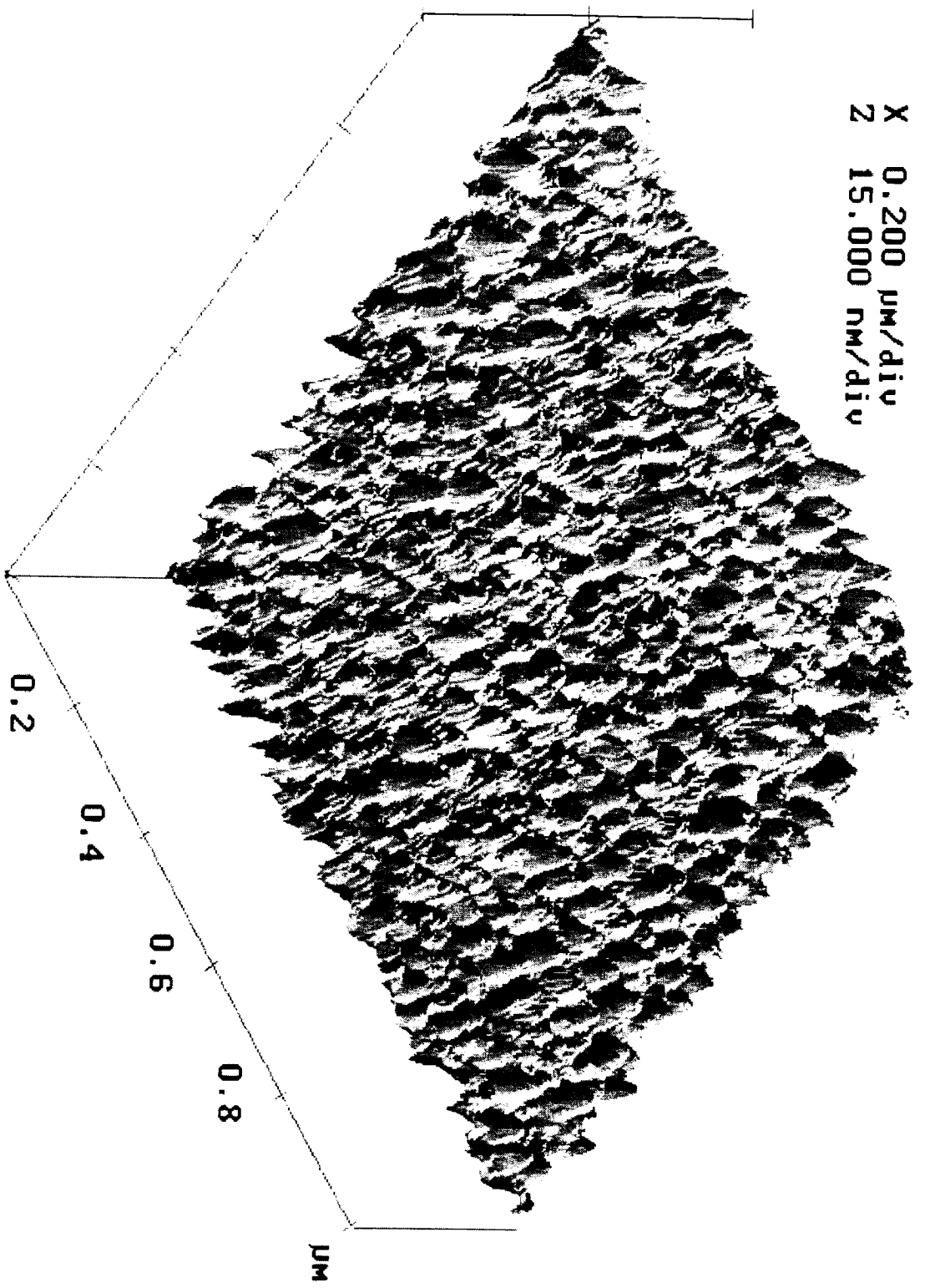
Figure 10c. AlN film on silica & annealed at 850 C.

µm

7 Bibliography

[1] A. Hafidi, M. Billy, J. P. Lecompte, *Journal of Materials Science*, 27, 3405 (1992).

[2] D. Robinson, and R. Dieckmann, *Journal of Materials Science*, 29, 1949 (1994).

[3] Y. Takeshi, K. Shinozaki, N. Ishizawa, N. Mizutani, and M. Kato, *Journal of the American Ceramic Society*, 71, C-334 (1988).

[4] K. Watari, K. Ishizaki, and T. Fujikawa, *Journal of Materials Science*, 27, 2627 (1992).

[5] J. H. Enloe, R. W. Rice, J. W. Lau, R. Kumar, and S. Y. Lee, *Journal of the American Ceramic Society*, 74, 2214 (1991).

[6] N. Kuramoto, H. Taniguchi, and I. Aso, *Ceramic Bulletin*, 68, 883 (1989).

[7] W. D. Kingery, H. K. Bowen, D. R. Ulhmann, Introduction to Ceramics, John Wiley & Sons, United States, (1976), pp. 61-3.

[8] Ralph W. G. Wyckoff, Crystal Structures, Vol. 1, John Wiley & Sons, New York, (1965), pp. 110-1.

[9] G. A Jeffrey, G. S. Parry, and R. L. Mozzi, *The Journal of Chemical Physics*, 25, 1024 - 31 (1956).

[10] A. U. Ahmed, A. Rys, N. Singh, J. H. Edgar, and Z. J. Yu, *Journal of the Electrochemical Society*, 139, 1146 (1992).

[11] J. A. Kovacich, J. Kasperkiewicz, D. Lichtman, C. R. Aita, *Journal of Applied Physics*, 55, 2935 (1984).

[12] G. Yamaguchi and H. Yanagida, *Journal of the Ceramic Association of Japan*, 32, 1264-5 (1959).

[13] K. T. Park, J. Cao, Y. Gao, G.W. Wicks, M. W. Ruckman, *Journal of Applied Physics*, 70, 2623-27 (1991).

[14] P. Gassmann, F. Bartolucci, R. Franchy, *Journal of Applied Physics*, 77, 5718-24 (1995).

[15] P. Martin, R. Netterfield, T. Kinder, A. Bendavid, *Applied optics*, 31, 6734-40 (1992).

[16] G. K. Wehner, *Advances in Elec. and Elec. Physics*, 7, 239 (1955).

[17] E. Kay, *Advances in Elec. and Elec. Physics*, 17, 245 (1962).

[18] A. Von Engle, Ionized Gases, Oxford University Press, London (1965).

[19] J. A. Thornton, *Journal Vacuum Science Technology*, 15, 188 (1978).

[20] J. A. Thornton, "Recent Developments in Sputtering --- Magnetron Sputtering", *Proceedings of the 21st Technical Conference, Society of Vacuum Coaters*, Detroit, Michigan (1978).

[21] J. A. Thornton, *Journal of Vacuum Science Technology*, 15, 171 (1978).

[22] J. S. Loagan, N. M. Mazza, and P. D. Davidse, *Journal of Vacuum Science Technology*, 6, 120 (1969).

[23] Rolfe E. Hummel, Electronic Properties of Materials, Springer-Verlag, Berlin Heidelberg, (1993), pp. 186-220.

[24] C. Kittel, Introduction to Solid State Physics, John Wiley & Sons, Inc., New York, (1971), pp. 447 - 63.

[25] A. J. Decker, Solid States Physics, Macmillan & Co. Ltd., United Kingdom, (1952), pp. 133 - 57.

[26] J. B. Marion, <u>Classical Electromagnetic Radiation</u>, Academic Press, Inc., New York, (1974), pp. 283 - 4.

[27] A. G. Marshall and F. R. Verdun, <u>Fourier Transforms in NMR, Optical, and Mass Spectrometry</u>, Elsevier, Amsterdam, (1990), pp. 1-68.

[28] K. F. Palmer and M. Z. Williams, *Applied Optics*, 24, 1788-98 (1985).

[29] C. F. Klingshirn, <u>Semiconductor Optics</u>, Springer-Verlag, Heidelberg, (1995), pp. 248-51.

[30] C. R. Aita, C. J. Kubiak, and F. Y. H. Shih, *Journal of Applied Physics*, 66, 4360-4 (1989).

[31] Max Garbuny, <u>Optical Physics</u>, Academic Press, Inc., New York, (1965), pp. 226 - 7.

[32] R. K. Willardson, ed., <u>Semiconductors an semimetals</u>, Academic Press, Orlando, (1982), vol. 21: J. L. Pankove, ed., <u>Hydrogenated Amorphous Silicon</u>, pp. 12-79.

[33] F. Ansart and J. Bernard, *Phys. Stat. Sol. (a)*, 134, 467-73 (1992).

[34] Digital Instruments, <u>Nanoscope Command Reference Manual</u>, Version 4.11, 1996.

[35] C. Julian Chen, <u>Introduction to Scanning Tunneling Microscopy</u>, Oxford University Press, Inc., New York, (1993), pp. 313-22.

[36] Perkin-Elmer Corporation, <u>Lambda 11 UV/Vis Spectrometer - Installation, Maintenance, System Description</u>, Part No. B050-9913, 1994.

[37] Perkin-Elmer Corporation, 1700X Series FTIR Spectrometers Instrument Manual, Perkin-Elmer Ltd., 1988.

[38] Gary E. McGuire, <u>Characterization of Semiconductor Materials</u>, Noyes Publications, Park Ridge, New Jersey, (1989), pp. 55-110.

[39] The Major Analytical Instrumentation Center, <u>Analytical Techniques Handbook</u>, University of Florida, 1995.

[40] John P. McKelvey, <u>Solid State Physics</u>, Krieger Publishing Company, Malabar, Florida, (1993), pp. 40-5.

[41] John P. McKelvey, <u>Solid State Physics</u>, Krieger Publishing Company, Malabar, Florida, (1993), pp. 45-51.

[42] G. A Jeffrey, G. S. Parry, and R. L. Mozzi, *The Journal of Chemical Physics*, 25, 1024 - 31, (1955).

[43] R. D. Shannon, *Journal of Applied Physics*, 73, 348-66 (1993).

[44] R. A. Youngman and J. H. Harris, *Journal of the American Ceramic Society*, 73, 3238-46 (1990).

[45] J. C. Zolper, D. J. Rieger, A. G. Baca, S. J. Pearton, J. W. Lee, and R. A. Stall, *Applied Physics Letters*, 64, 538-40 (1996).

[46] American Society for Testing and Materials, <u>KWIC Guide to the Powder Diffraction Files</u>, ASTM, 1966.